2016

Computational Study of Water Desalination by Reverse Osmosis Membrane

Ali Eisa M. Anqi
Lehigh University

Computational Study of Water Desalination by Reverse Osmosis Membrane

by

Ali Eisa M. Anqi

Presented to the Graduate and Research Committee

of Lehigh University

in Candidacy for the Degree of

Doctor of Philosophy

in

Mechanical Engineering

Lehigh University

May 2016

Approved and recommended for acceptance as a dissertation in partial fulfilment of the requirements for the degree of Doctor of Philosophy.

_____
Date

_____
Dr. Alparslan Oztekin
Committee Chair

_____
Approved Date

_____
Dr. Jacob Kazakia
Committee Member

_____
Dr. Edmund Webb
Committee Member

_____
Dr. Xuanhong Cheng
Committee Member

ACKNOWLEDGMENT

I would like to thank Dr. Alparslan Oztekin for his guidance and advice throughout my research. Dr. Alparslan Oztekin has lead by example. I would like to express my thanks to the committee members Dr. Jacob Kazakia, Dr. Edmund Webb and Dr. Xuanhong Cheng for serving on my dissertation committee. I offer my thanks to Dr. Nawaf Alkhamis who shared his knowledge and expertise in this research field. I also thank Mohammad Anqi, my brother, for his support and his valuable information and experience in reverse osmosis desalination process.

I would like to thank my mother Aishah Anqi for her endless love and support, and I dedicate this work to the memory of my father Eisa Anqi who left us inspiring memories. I must express my gratitude to my wife Khulud Fawaz for her love and encouragement throughout the time, and I thank my children Leen and Eisa. I am thankful to my sisters: Layla and Mariam for their support.

I am grateful to King Khalid University for providing the financial support to pursue my graduate studies.

CONTENTS

LIST OF TABLES

LIST OF FIGURES

NOMENCLATURE

(u, v, w)	components of velocity [m/s]
(x, y, z)	spatial coordinates
h_m	mass transfer coefficient [m/s]
C_D	drag coefficient
F_1, F_2	blending functions
U_{ave}	average inlet velocity [m/s]
a_1	turbulent model parameter
c_0	inlet concentration [kg/m^3]
c_b	feed bulk concentration [kg/m^3]
c_f	membrane salt concentration [kg/m^3]
c_p	production concentration [kg/m^3]
f_x	drag force [N]
v_w	water flux [m/s]
Δp	transmembrane pressure difference [Pa]
A	water permeability [m/s Pa]
C_D	drag coefficient
C_L	lift coefficient
d	spacer diameter [m]
D	diffusivity [m^2/s]
e	distance from spacer to wall [m]

F_1, F_2	blending functions
h	channel height [m]
h_m	mass transfer coefficient [m/s]
k	turbulent kinetic energy [J/kg]
p	pressure [Pa]
Re	Reynolds number, $Re = U_{ave}\ 2h/\nu$
s	distance between spacers [m]
Sc	Schmidt number, $Sc = \nu/D$
Sh	Sherwood number, $Sh = h_m\ h/D$
St	Strouhal number, $St = fd/U_{ave}$
t	time [s]
CP	coefficient of performance
c	salt concentration [kg/m^3]
l	distance between spacers [m]
s	channel depth in z-direction [m]
μ	dynamic viscosity [Pa s]
μ_t	eddy viscosity [Pa s]
ρ	density [kg/m^3]
ω	specific dissipation rate [1/s]
α	normalized spacing, $\alpha = s/d$
β, β^*	turbulent model parameters
$\sigma_\omega, \sigma_{\omega_2}$	turbulent model parameters

ν	kinematic viscosity [m^2/s]
ν_t	kinematic eddy viscosity [m^2/s]
$\boldsymbol{\kappa}$	osmotic coefficient [kPa m^3/kg]
τ	scaled time $\tau = 2\ t\ U_{ave}/d$
γ	turbulent model parameter
σ_{k1}	turbulent model parameter
$\Delta\pi$	osmotic pressure [Pa]
$\boldsymbol{\tau}$	Normalized wall shear stress
θ	strand angle [°]

Subscripts

i and j	index notation
w	properties along the membrane surface
f	properties along the membrane in the feed channel

ABSTRACT

The reverse osmosis (RO) desalination process has been widely used to overcome the fresh water shortages around the globe. Spiral wound membranes are utilized to desalinate sea water and brackish water. In a typical spiral wound desalination module, the feed channel contains spacers with different arrangements. The membranes are semi-permeable which allows the pure water to pass through and hold back the dissolved salt ions from passing. In order to model desalination process properly in these modules accurate membrane flux model should be employed. The membrane is treated as a functional surface where the rate of water permeation is determined by the local pressure, osmotic pressure and local concentration.

The rejection of salt from membrane causes an accumulation of salt near the membrane surface. Such phenomena are referred as concentration polarization occurring at the surface or near the surface of the membrane. The concentration polarization adversely affects the membrane performance and reduces the lifetime of the desalination module. The concentration polarization causes an increase in the osmotic pressure across the membrane and in turn leads to reduction of water flux through the membrane. The fouling potential also increases in regions where high concentration polarization occurs. Fouling build ups and scaling are also known as influencing the membrane performance adversely. This study demonstrates that membrane mass flux performance, concentration polarization and the fouling buildup/scaling are profoundly influenced by the flow structures in the feed channel.

It has been shown by the present study that the flow inside the feed channel containing spacers can be strongly three dimensional and transient. Numerical simulations are conducted to characterize three dimensional and transient nature of the flows. Navier-Stokes equations and the mass transport equation are solved to determine the flow and concentration fields in the feed channel. The laminar flow model is utilized at low flow rates while turbulent flow models are utilized at higher flow rates. The Shear Stress Transport (SST) k-ω turbulence model and large eddy simulation (LES) methods are employed to characterize the turbulent flow structures.

The presence of spacers in the feed channel enhances membrane performance significantly. The influence of the spacer is more pronounced at higher flow rates. The spacing and the arrangement of spacers have strong influence on the membrane performance. Spacers also aid in mitigating concentration polarization and fouling in these modules. Momentum mixing induced by the presence of spacers is the reason for improvement of membrane performance. Modules including the mesh type of spacers with 30° angle performs best. This study clearly illustrated that the type, shape and arrangements of spacers are integral part of design and optimization of reverse osmosis desalination modules.

CHAPTER 1: INTRODUCTION

Synthetic membranes have been widely used in industrial applications. Membranes perform separation and purification with the advantage of low energy consumption compared to evaporation methods. Separation by membranes is applicable in industries such as water desalination, food industry, medical devices and others. Species can be separated by membrane from homogeneous and heterogeneous mixtures [1,2]. Water purification and desalination processes using membranes have a wide range of applications.

Loeb and Sourirajan synthesized cellulose acetate (CA) membrane to desalinate seawater in 1962, and it was commercialized in the 1970's [3]. Then Cadotte and Petersen fabricated polyamide composite membrane in 1978 for reverse osmosis applications [4,5]. Now, these two types of membranes are widely used worldwide in fresh water production industry. The water industries include different processes such as microfiltration, ultrafiltration, nanofiltration and reverse osmosis. Each process separates certain type of particles and species from the feed water based on size (see Figure 1). The membrane is treated as a microporous medium in the microfiltration, ultrafiltration and partially the nanofiltration processes. The pore-flow model governs the flow in microporous media, and it is based on Darcy's law. In reverse osmosis, the membrane is modeled by the solution-diffusion model which utilizes the Fick's diffusion law. The nanofiltration process is a transition stage where the flow through the membrane is modeled by a combination of the pore-flow and solution-diffusion models.

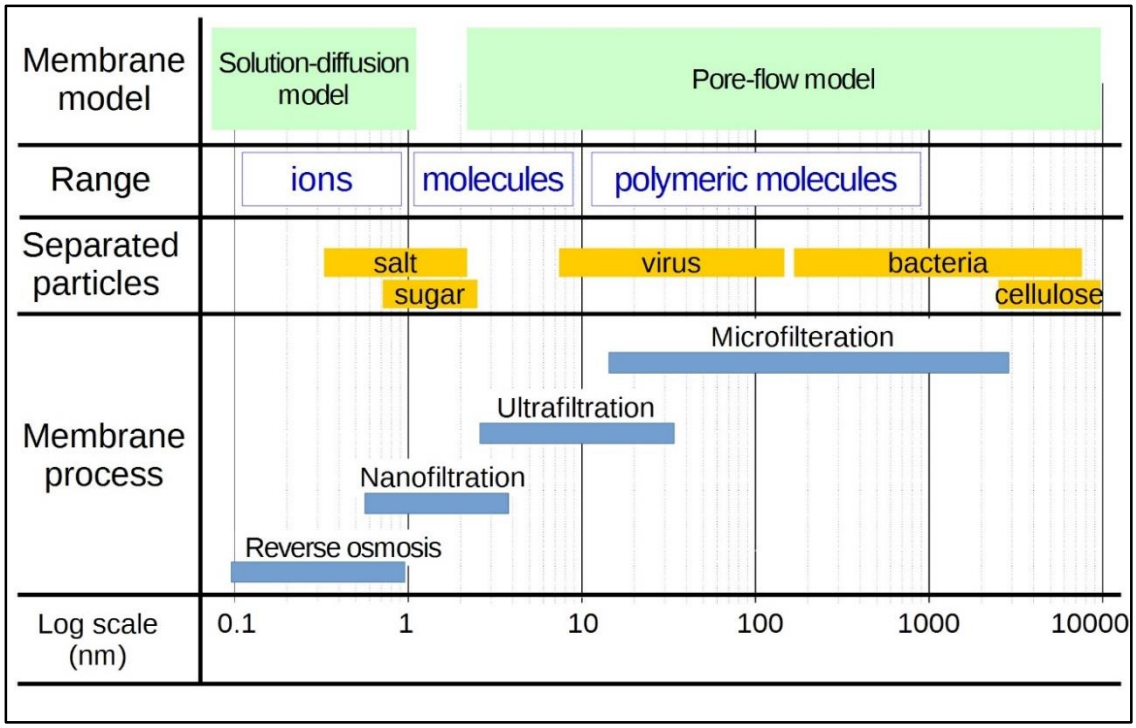

Figure 1: Water purification processes.

1.1. REVERSE OSMOSIS DESALINATION

Reverse Osmosis (RO) is a process which is used around the globe to produce fresh water. This technology is typically used to desalinate seawater or brackish water. Reverse Osmosis is capable of producing fresh water by applying high pressure in a feed channel surrounded by a semi-permeable membrane. The membrane lets the water passes through and holds back the dissolved salt ions. The applied pressure has to be greater than the osmotic pressure of the solution. The fresh water production rate is dependent on the salt concentration in the feed water and on membrane properties such as the selectivity and the permeability. The rate of water permeation increases as values of the selectivity and the permeability of the membrane increase. The increase in the

water permeation causes an increase in the salt accumulation at or near the membrane surface. That in turn increases the probability of the occurrence of salt concentration polarization along the membrane surface. The occurrence of concentration polarization along the surface of the membrane has two major undesirable effects on the membrane performance [6–11]. One is the increase of the osmotic pressure as the salt concentration rises so the applied pressure must be increased to keep the water production rate the same. The other is the promotion of scaling and fouling along the surface of the membrane at the region where the salt concentration polarization occurs. In spiral wound membranes, spacers are placed in the feed channel to maintain the gap between the membranes and to promote momentum mixing (Figure 2).

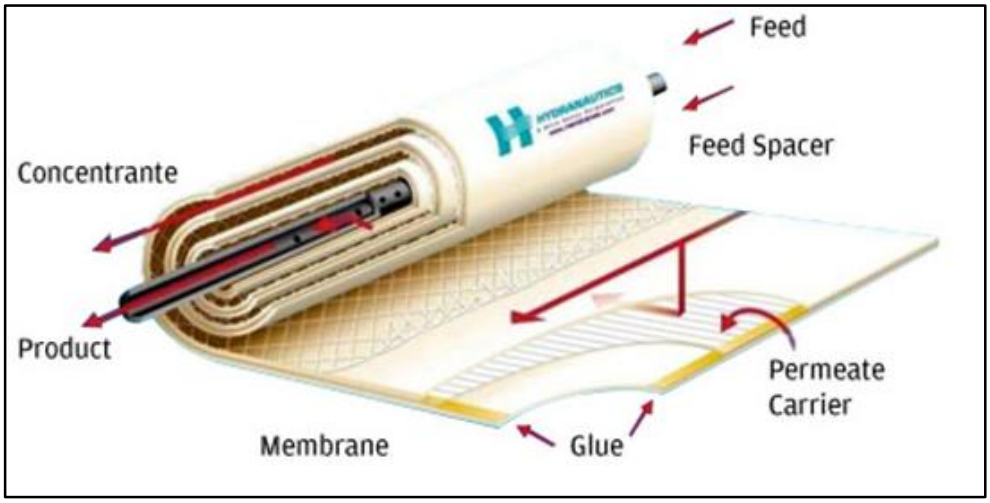

Figure 2: Schematic of spiral wound membrane. (source: Auxiaqua [12])

1.2. LITERATURE REVIEW

Many investigators have studied the flow and the mass transfer in reverse osmosis feed channel [13–17]. Shakaib et al. [18] considered three dimensional simulations for flow and mass transfer in feed channel including spacers. They assumed that the membrane was impermeable surface along which the concentration was constant. They showed that the mass transfer in the feed channel is strongly influenced by the spacer geometry. Geraldes et al. [19] studied concentration polarization inside the feed channel with ladder-type spacers. They employed momentum and mass transfer equations and imposed no-slip, no-penetration conditions at the membrane surface. They calculated the salt flux through the membrane by artificially introducing the permeate velocity. They concluded that the spiral wound membrane performs better when the spacer-filament is adjacent to the membrane surface. Both Shakaib et al [18] and Geraldes et al. [19] considered laminar flows. Karode and Kumar [20] conducted three-dimensional flow simulations and experiments to examine flow characteristics in a feed channel containing different types of commercial spacers. Karode and Kumar [20] have concluded that the turbulent flow structures, the degree of pressure drops and the characteristics of the wall shear stress were strongly influenced by the spacer's types and arrangements. Fimebers-Weihs and Wiley [21] performed steady three-dimensional flows and mass transfer simulations. The membrane was treated as an impermeable wall, and the mass transfer coefficient was determined from an empirical relation. They reported that the pressure drop and the mass transfer coefficient are influenced by the spacer configurations and by the feed flow rate. Koutsou et al. [22] conducted a direct numerical simulation to investigate the flow characteristics inside the feed channel

bounded by impermeable walls. They reported that the flow inside the feed channel containing spacers becomes unsteady for values of Reynolds number greater than about 40. Their computational study did not consider the mass transfer. Recently, Srivathsan et al. [23,24] have investigated the membrane performance by conducting three dimensional steady computational fluid dynamics simulations. They utilized periodic condition in the streamwise direction by including two crossing spacers in the computational cell. They have treated the membrane as a permeable surface and also as an impermeable surface and calculated Sherwood number using an empirical relation. Saeed et al. [25] has performed a numerical simulations to study the mass transport in spacer filled membrane. They solved the Navier-Stokes equations and the mass transport equation in a feed channel bounded by an impermeable wall. Quasi three dimensional simulations are conducted by using periodic boundary conditions in the stream-wise direction. The mass fraction of sodium chloride is assumed to be constant along the membrane surface. Both Srivathsan et al. [23] and Saeed et al. [25] concluded that the spacing between spacers highly influences the membrane performance and the pressure drop.

The flow in a channel filled with spacers is similar to the flow past cylinders confined in a channel. Some of the findings relevant to the present study are summarized here. Chakraborty et al. [26] documented that the drag coefficient decreases as the Reynolds number (Re) increases, and the drag coefficient increases as the blockage ratio increases at fixed Re. Kanaris et al. [27] reported that the transition from two-dimensional to three-dimensional flows occurs at about $180 < Re < 210$ in flows past cylinder with a blockage ratio of 1/5, where Re is based on the centerline

velocity and cylinder diameter. Rehimi et al. [28] reported that the onset of the vortex shedding occur at $Re = 108$ and the onset of transition from two dimensional to three dimensional flows occurs at $Re = 159$ in flows past a cylinder with a blockage ratio of 1/3. Griffith et al. [29] et al. reported that the flow transitions occur at lower value of Re when the blockage ratio is increased to 1/2. The present study focuses on the effect of such flow transitions on the membrane performance, concentration polarization, and fouling for water desalination process by reverse osmosis.

CHAPTER 2: MATHMATICAL MODELING

2.1. GOVERNING EQUATIONS

Velocity and pressure fields in the feed channel are governed by the continuity and momentum equation, and the concentration field is governed by the mass transport equation. The binary solution is assumed to be incompressible with density, ρ, and viscosity, μ. The diffusion coefficient, D, is assumed to be constant. The equations governing the fluid motions are the Navier-Stokes equations:

$$\frac{\partial u_i}{\partial x_i} = 0, \tag{1}$$

$$\frac{\partial u_i}{\partial t} + u_j \frac{\partial u_i}{\partial x_j} = \frac{1}{\rho}\frac{\partial p}{\partial x_i} + \nu \frac{\partial^2 u_i}{\partial x_j \partial x_j}\ , \tag{2}$$

The equation governing the mass transport in the feed channel

$$\frac{\partial c}{\partial t} + u_j \frac{\partial c}{\partial x_j} = D \frac{\partial^2 c}{\partial x_j \partial x_j}. \tag{3}$$

Here i and j are the summation indices. $x_1 = x$ is the stream-wise direction, $x_2 = y$ is the cross-flow direction, and $x_3 = z$ is the span-wise direction. $u_1 = u$ is the stream-wise component, $u_2 = v$ is the cross-flow component, and $u_3 = w$ is the span-wise component of the velocity. t is the time, and c is the salt concentration of the binary solution of salt and water.

It is well documented that the flow, temperature and concentration fields in channels containing cylinders are predicted accurately by the shear stress transport (SST) k-ω turbulence model [30–33]. It is also well-documented that flows past arrays of spacers confined in channels have turbulent-like characteristics for $Re \geq 400$ [22,34–36]. The SST k-ω turbulence model is employed by the present computational

study to characterize three-dimensional steady turbulent flow structures in the feed channel for Re of 400 or above. The SST k-ω turbulence momentum transport equation is given by:

$$u_j \frac{\partial u_i}{\partial x_j} = -\frac{1}{\rho}\frac{\partial p}{\partial x_i} + \frac{1}{\rho}\frac{\partial}{\partial x_j}\left((\mu + \mu_t)\frac{\partial u_i}{\partial x_j}\right) \quad (4)$$

where μ is the dynamic viscosity and μ_t is the eddy viscosity, $\mu_t = \rho \frac{a_1 k}{\max(a_1\omega, \Omega F_2)}$. The equations governing the turbulence kinetic energy, k, and the specific dissipation rate, ω, are:

$$u_i \frac{\partial(\rho k)}{\partial x_i} = \tau_{ij}\frac{\partial u_i}{\partial x_j} - \beta^*\rho\omega k + \frac{\partial}{\partial x_j}[(\mu + \sigma_k\mu_t)\frac{\partial k}{\partial x_j}, \quad (5)$$

$$u_i \frac{\partial(\rho\omega)}{\partial x_i} = \frac{\gamma}{\nu_t}\tau_{ij}\frac{\partial u_i}{\partial x_j} - \beta\rho\omega^2 + \frac{\partial}{\partial x_j}\left[(\mu + \sigma_\omega\mu_t)\frac{\partial\omega}{\partial x_j}\right] + 2\rho(1 - F_1)\sigma_{\omega 2}\frac{1}{\omega}\frac{\partial k}{\partial x_j}\frac{\partial\omega}{\partial x_j} \quad (6)$$

where Ω is the vorticity magnitude, $a_1, \beta, \beta^*, \sigma_k, \sigma_\omega, \sigma_{\omega_2}$ and γ are closure coefficients, and F_1, F_2 are the blending functions. Detailed description of the model can be found in Ref.[37].

The SST k-ω turbulence mass transport equation is given by:

$$u_j \frac{\partial c}{\partial x_j} = \frac{\partial}{\partial x_j}\left(\left(D + \frac{\mu_t}{\rho\, Sc_t}\right)\frac{\partial c}{\partial x_j}\right) \quad (7)$$

where Sc_t is the turbulence Schmidt number.

2.3. NUMERICAL METHOD

The idea in the computational fluid dynamics is to convert the governing equations of the fluid flow and mass transport to a system of algebraic equations. Flow and velocity field can be approximated by solving coupled non-linear set of algebraic

equations. There are different approaches to discretize the Navier-Stokes equations and mass transport equation. The finite difference, finite element and finite volume are the most common methods in the computational fluid dynamics. The finite volume performs better than the other two methods in the complex geometries, and it demands less computational resources than the finite element method. In addition, the conservation laws are satisfied automatically in the finite volume method [38–40].

In finite volume method, the conservation laws are applied to the control volume, Ω, with control surface, s (Figure 3). $\boldsymbol{V}$ is the velocity vector, and $\boldsymbol{n}$ is the normal vector to the control surface. The conservation of mass, momentum and concentration are written in the integral form. These integral forms represent a balance between the rate of change of flow properties in the control volume, Ω, and the rate of flux of these properties through the control surface. For incompressible viscous Newtonian-fluid, the conservation laws are as follows.

The mass conservation

$$\frac{\partial}{\partial t}\int_{\Omega}\rho\, d\Omega + \int_{s}\rho\ \boldsymbol{V}\cdot\boldsymbol{n}\, ds = 0 \tag{8}$$

Here t denotes the time and ρ denotes the density of solution.

The momentum conservation

$$\frac{\partial}{\partial t}\int_{\Omega}\rho\, u_i\, d\Omega + \int_{s}\rho u_i \boldsymbol{V}\cdot\boldsymbol{n}\, ds = \int_{s}\left[(-p\, n_i) + \sum_j \mu\left(\frac{\partial u_i}{\partial x_j} + \frac{\partial u_j}{\partial x_i}\right) n_j\right] ds \tag{9}$$

Here u_i is the i^{th} velocity components ($u_1 = u, u_2 = v\ and\ u_3 = w$). u, v and w are the stream-wise, cross-flow and the span-wise components of the velocity vector, respectively. μ is the dynamic viscosity.

The concentration equation

$$\frac{\partial}{\partial t}\int_{\Omega} c\, d\Omega + \int_{s} c\, \boldsymbol{V}\cdot\boldsymbol{n}\, ds = \int_{s} D\, \nabla c\cdot n\, ds \qquad (10)$$

Here c is the concentration, and D is the diffusion coefficient.

The Gauss's divergence theorem converts an integral over a control surface into an integral over a control volume.

$$\int_{s} \rho\, \boldsymbol{V}\cdot\boldsymbol{n}\; ds = \int_{\Omega} \nabla\cdot(\rho\, \boldsymbol{V})\, d\Omega \qquad (11)$$

By using the equation (11), equations (8-10) become integrals over the control volume.

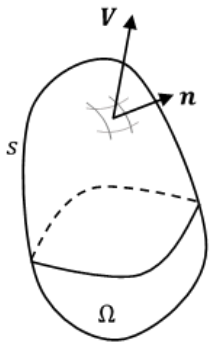

Figure 3: Control volume.

2.2. MEMBRANE MODELING

The solution-diffusion model was introduced in 1940's to model the mass transport and concentration gradient at the membrane surface for the gas separation process. At that time, the pore-model was used to predict the mass transport at the membrane surface in the water desalination by reverse osmosis. In the 1980's, the solution-diffusion became well-accepted model in predicting the membrane performance in the field of the water purification by the reverse osmosis [2,41]. The solution-diffusion model considers the chemical potential as the driving force of the mass transport. On the other hand, the pore-model is based on assuming the driving

force is the pressure difference only. Experimental results [42–44] prove that the solution-diffusion is more accurate than the pore-model in predicting the membrane performance in the water desalination by the reverse osmosis.

The membrane is considered as a functional surface under the solution-diffusion approach. In the solution-diffusion model, the local water flux is determined from the trans-membrane pressure difference and the local osmotic pressure between the feed and the production sides. Simultaneously, the salt concentration gradient is calculated from the local water flux and local salt concentration along the membrane surface (Figure 4). The equations for the rate of water permeate and for the local salt concentration gradient at the membrane surface are:

$$\left.\begin{array}{l} v_w = A[(p_f - p_p) - (\pi_f - \pi_p)] \\ D\frac{\partial c}{\partial y}\Big|_f = v_w(c_f - c_p) \end{array}\right\} \quad (12)$$

where v_w is the water flux through the membrane, A is the water permeability through the membrane, p is the pressure, π is the osmotic pressure, and the subscripts f and p denote the feed and production sides, respectively. The osmotic pressure,π, is calculated from Van't Hoff's equation:

$$\pi = i\phi RTc/M \quad (13)$$

where i denotes the number of ions produced by disassociation of solute, ϕ is the osmotic coefficient, c is the salt concentration in kg/m^3, M is the molecular weight of the salt in kg/mol, R is the universal gas constant (0.0083145 KPa m^3/(mol K°)), and T is the absolute temperature in K°. For a solution consists of water and dissolved NaCl, the osmotic pressure, equation (*13*), can be written as:

$$\pi = \boldsymbol{\kappa} c \quad (14)$$

Here $\boldsymbol{\kappa}$ is the osmotic pressure coefficient, $\boldsymbol{\kappa} = i\phi RT/M$. The value of $\boldsymbol{\kappa}$ at the temperature of 293 K° is 75 KPa m^3/kg. By substituting equation (14) in equations (12), the water flux and salt concentration gradient at the membrane surface in the feed side can be written as:

$$\left.\begin{array}{l} v_w = A[(\Delta p) - \boldsymbol{\kappa}(c - c_p)] \\ D\frac{\partial c}{\partial y}\Big|_f = v_w(c_f - c_p) \end{array}\right\} \quad (15)$$

where Δp is the transmembrane pressure difference.

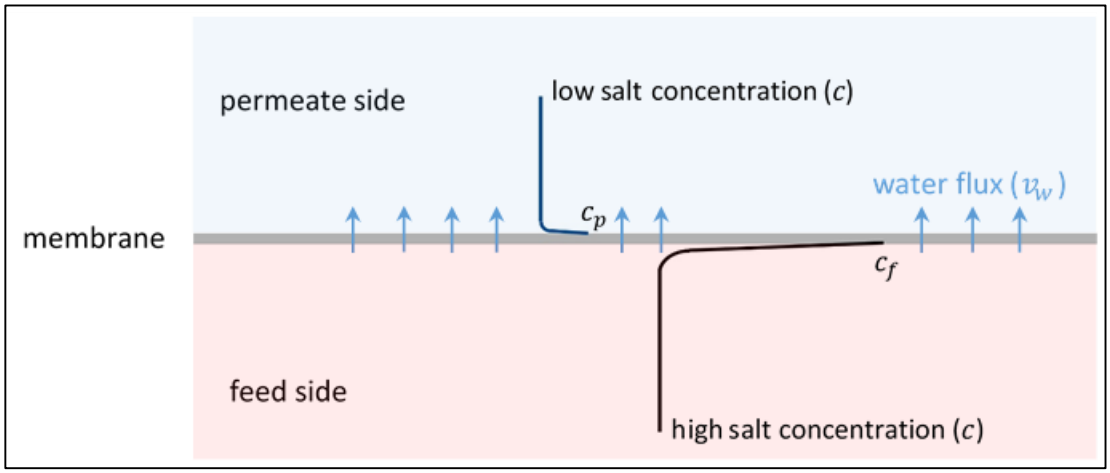

Figure 4: Concentration polarization and water flux at the reverse osmosis membrane surface.

2.3. DIMENSIONLESS PAPAMETERS

The results are presented in terms of various dimensionless properties. The drag coefficient, C_D, is determined from:

$$C_D = \frac{2f_x}{\rho U_{ave}^2 A_s} \quad (16)$$

where f_x is the drag force exerted on the spacer, and A_s is the projected area of the spacer in the direction perpendicular to the stream-wise direction. The lift coefficient of a spacer is calculated from:

$$C_L = \frac{2\, f_y}{\rho\, U_{sp}^2 A_s} \tag{17}$$

where f_y is the lift force exerted on the spacer. The dimensionless mass transfer coefficient, Sherwood number (Sh), is evaluated as:

$$Sh = \frac{h_m\, h}{D} \quad , \quad h_m = \frac{D \left.\frac{\partial c}{\partial y}\right|_{y=h}}{(c_b - c_w)} \tag{18}$$

where h_m is the local mass transfer coefficient, h: the channel height, c_b is the bulk concentration. The friction coefficient is obtained from:

$$f = \frac{2h \left|\frac{dp}{dx}\right|}{(1/2)\, \rho U_{ave}^2} \tag{19}$$

where $\frac{dp}{dx}$ is the pressure drop in the channel, and U_{ave} is the average velocity at the channel inlet.

CHAPTER 3: TWO DIMENSIONAL ANALYSES

3.1. CIRCULAR SHAPED SPACERS

3.1.1. MESH STUDY AND VALIDATION

The schematic of the computational domain is depicted in Figure 5. The solution of salt water is studied for separation of salt from water using a RO membrane. Flow inside the channel with turbulators is considered for various arrangements: the inline geometry (e = $1/4\ h$), the staggered geometry (e = $1/8\ h$), and the staggered geometry with spacers touching the membrane (e = 0). Here *d* is the diameter of the spacer and *e* is the distance between the edge of the spacer and the membrane surface, as shown in Figure 5. Simulations are conducted with $\alpha = \frac{s}{d}$ of 10 and 20 for each spacer arrangement. Here *s* is the gap between the spacers. The distance x/h = 10 is assigned between the inlet and the first spacer to minimize the effect of the inlet on the flow structure inside the spacer bank. Similarly, the distance x/h = 20 is assigned between the last spacer and the outlet to minimize the outlet effect. Steady state simulations were conducted for three values of the Reynolds number: 400, 800 and 4000. In addition, a transient simulation at *Re* = 800 is conducted using the large eddy simulation (LES) to study the transient effects on the membrane performance in the inline geometry. Reynolds number is defined based on the hydraulic diameter of the channel, $Re = U_{ave}\ 2h/\nu$. Results presented in this Chapter were documented in Ref. [45].

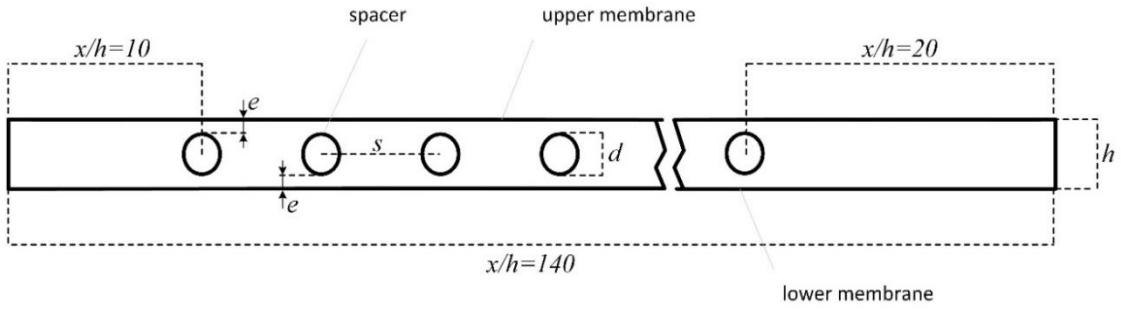

Figure 5: Schematic of the flow geometry

Disparity between diffusion coefficient and viscosity of salt-water binary solution leads to a large value for Schmidt number (Sc = 667). That results in a thin concentration boundary layer. In order to resolve the concentration field near the membrane surface very fine mesh elements are needed. Mesh structure near the surface of the membrane and the surface of the spacer is shown in Figure 6. A mesh optimization study is conducted using three meshes: 1.2×10^6, 1.8×10^6, and 2.4×10^6. For the three meshes, the profiles of stream-wise component of the velocity at the wake of the 1st spacer obtained by three meshes are nearly the same, as shown in Figure 7. Additionally, the drag coefficient is calculated for the 1st spacer using three meshes. The drag coefficient is found to be 1.09, 1.10, and 1.08, respectively for the 1.2×10^6, 1.8×10^6, and 2.4×10^6 meshes. That ensures that the grid independency is satisfactory. The 1.8×10^6 mesh is chosen to carry out both the steady state and the transient simulations.

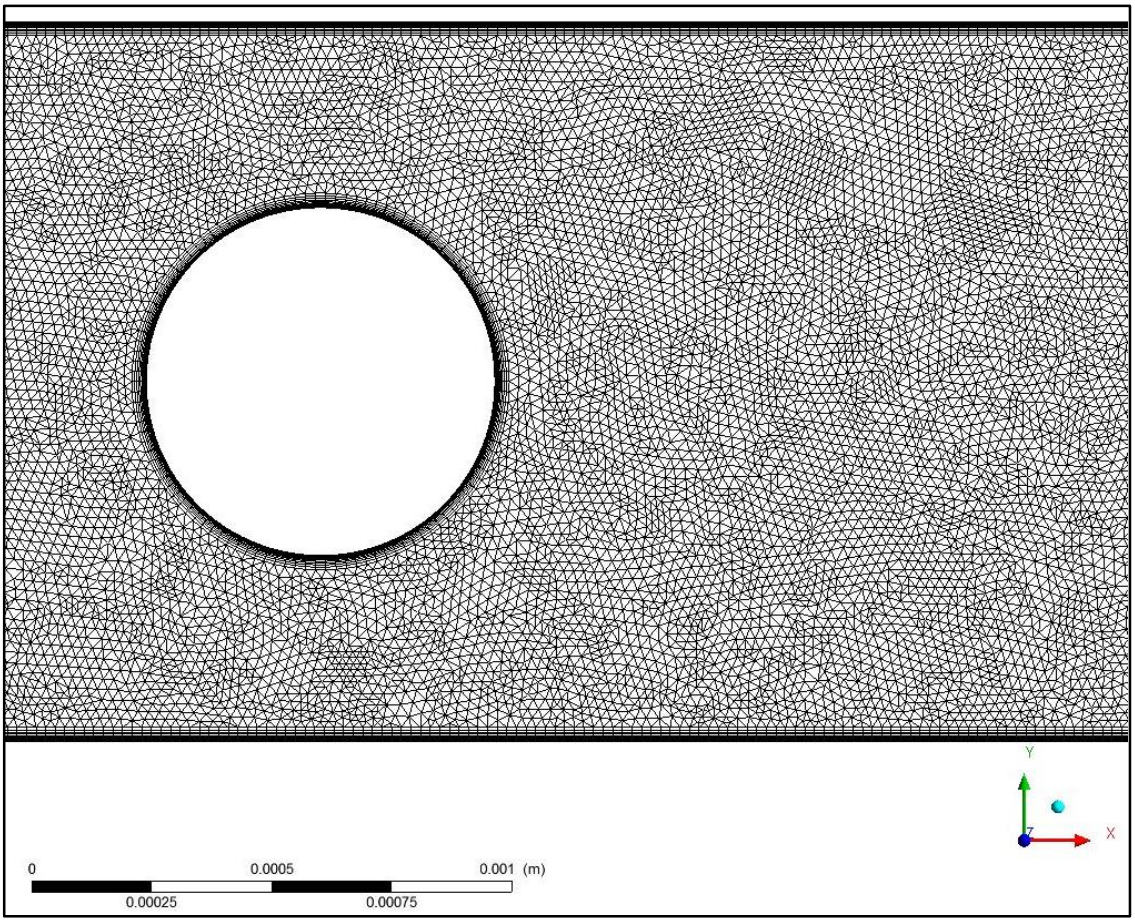

Figure 6: Mesh size near membrane and spacer.

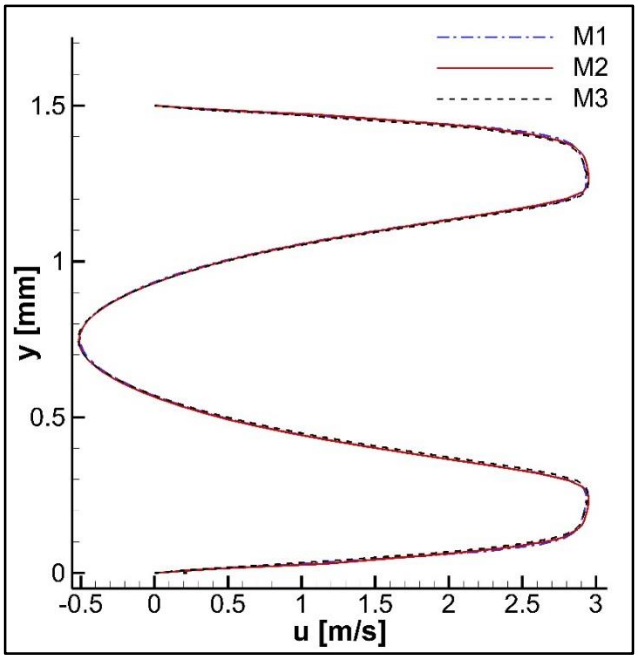

Figure 7: Profiles of stream-wise component of the velocity calculated using three different meshes: 1.2×10^6, 1.8×10^6, and 2.4×10^6

In order to validate the *k-ω* SST turbulence model employed in the present work, simulations are conducted in an empty channel and in a channel containing square cross sectioned spacers with an inline arrangement. The results of these simulations are compared to those reported by Ma and Song [36]. The same parameters used in Ref [36] are selected: Δp = 800 psi, c_0= 32000 ppm, A = 7.3×10^{-12} m/(s Pa), h = 1 mm, U_{ave}= 0.1 m/s, and Re = 149. The spacing between the cylinders is 4.5 mm and the channel length is 10 cm. The flow and the concentration field are depicted in Figure 8. Contours of the velocity and the salt concentration are very similar to those documented in Ref [36]. On the other hand, the wall concentration and the water flux through the membrane exhibit slightly different trend. The spacers are expected to redirect the flow toward the membrane which results in a thinner boundary layer. In the wake of the spacer, the expansion causes a thicker boundary layer and as the boundary layer becomes thicker it

leads to the concentration polarizations, as seen in Figure 7(c). Since the pressure in the governing equations is treated differently in the present work than in Ref [36], we expect to see slightly different concentration and water flux profiles between the two works. The pressure drop in the channel without and with spacers is 106 and 1014 Pa, respectively. The pressure drop predicted here for each case matches the reported pressure drop of corresponding cases in Ref [36].

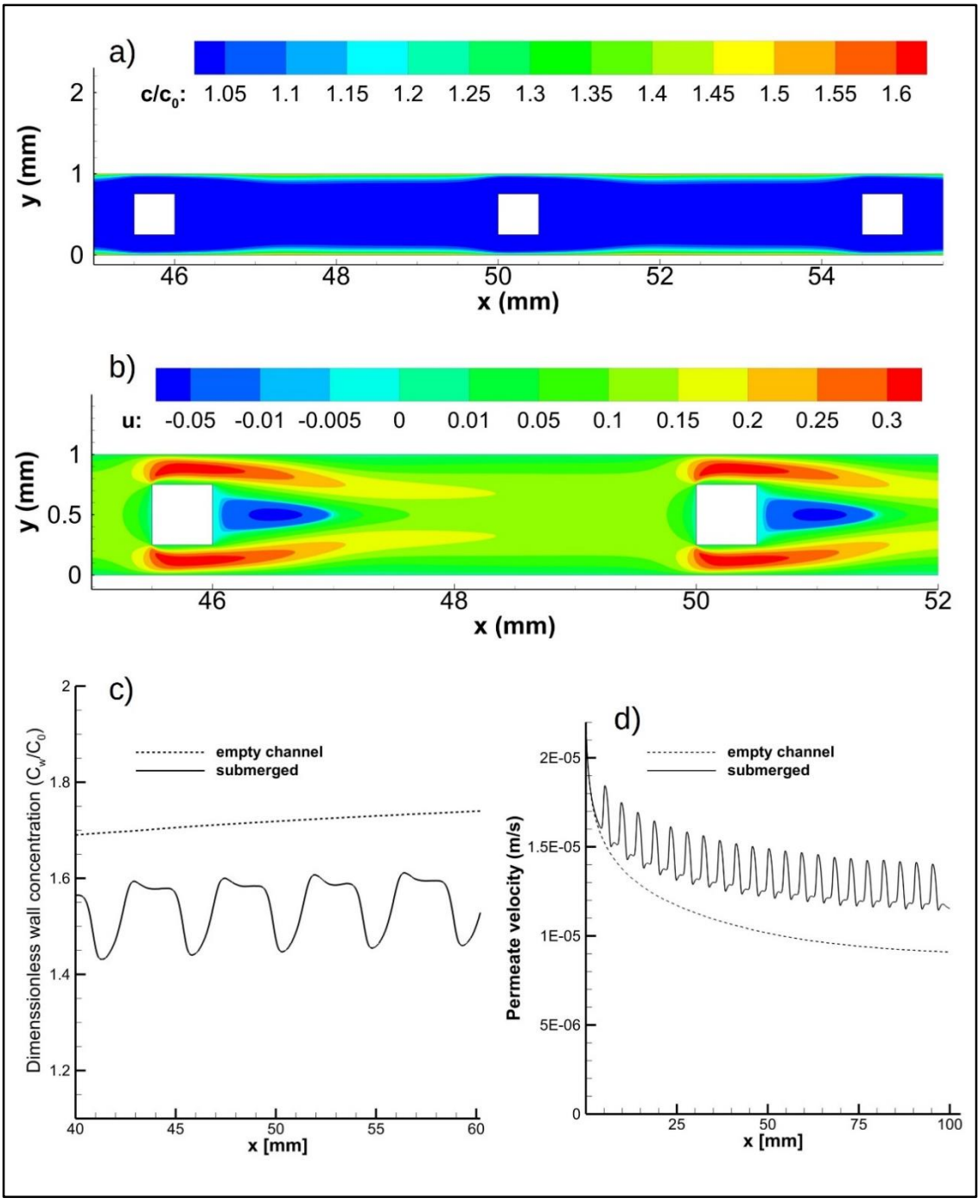

Figure 8: a) concentration contour of the submerged case. b) velocity contour of the submerged case. c) normalized concentration profile along the surface of the upper membrane. d) permeate velocity along the surface of the upper membrane

3.1.2. RESULTS

The results of steady flow simulations in the inline and the staggered geometries are presented at *Re* = 400, 800 and 4000 for α of 10 and 20. The results of the transient flow simulations in the inline geometry for α = 20 is presented and compared against that of the steady simulations.

Figure 9 illustrates steady state contours of the stream-wise component of the velocity and the normalized salt concentration at various locations along the *x*-axis for *Re* = 800 and α = 20. The cylinders are placed in an inline arrangement. The images are acquired between the first and second cylinder, the seventh and eighth cylinder, and between eleventh and twelfth cylinder, respectively. The velocity contours show that the flow has a repeated pattern following each spacer. Flow past the spacer expands, that leads to a thickening of a boundary layer in the wake few diameters away from the spacer. Polarization of concentration occurs at the same location where the momentum boundary layer thickens. The intensity of the polarization increases further downstream, as shown in Figure 9.

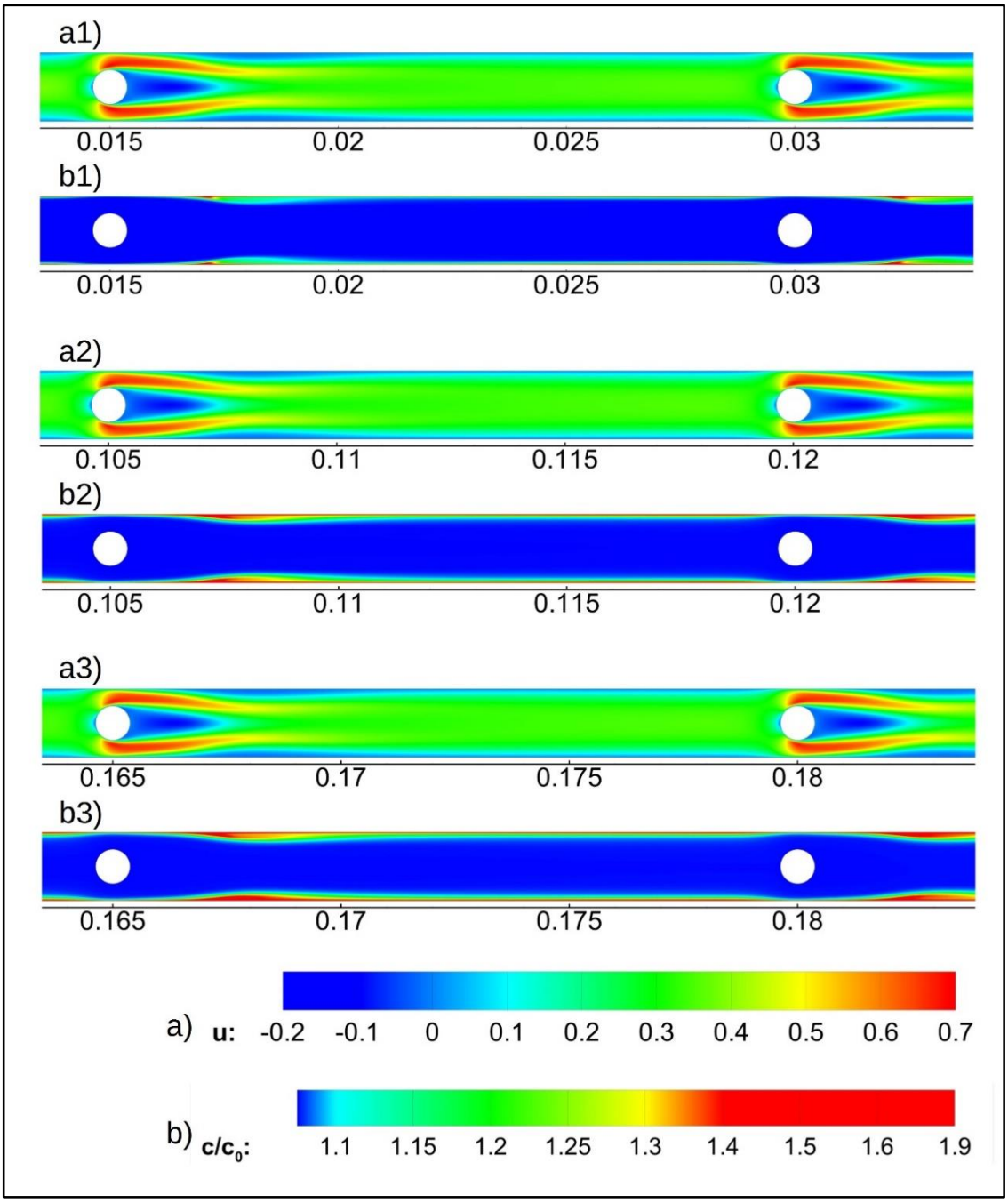

Figure 9: Steady flow at Re=800, α=20, and e=1/4 h. a1), a2), and a3) velocity contours and b1), b2 and b3) concentration contours at different locations along x-axis.

Figure 10 depicts the normalized concentration profiles (c/c_0) along the upper membrane. The black lines denotes the concentration profiles in the empty channel, the blue and the red lines denote the concentration profiles for α = 20, and α = 10, respectively, in various geometries. The same color coding is applied for the water flux and the Sherwood number profiles along the membrane surface depicted in Figures 11 and 12, respectively. The concentration polarization is alleviated at all *Re* with the presence of spacers in the channel. In the inline geometry, the best mitigation of the concentration polarization is obtained at *Re* = 800 when it is compared against to the open channel, as shown in Figure 10 (a). It is also noted that at high speed flow, *Re* = 4000, the concentration profiles are not influenced significantly as the spacing of the cylinders is changed. Figure 10 (b) shows the concentration profiles in the staggered geometry with e = 1/8 h. The staggered spacers exhibit significant level of polarization mitigation at Re = 800 for both α = 20 and α = 10. The improvement is better with α = 10 than that with α = 20, as illustrated in Figure 10 (b). On the other hand, the staggered spacers hardly mitigate the concentration polarization at $Re = 400$. Figures 10 (c) and 10 (d) show the concentration profiles in the staggered geometry when spacers touching the membrane surface for α = 20 and 10, respectively. In this geometries, Re = 800 shows the maximum level polarization mitigation. There is a spike in the concentration distribution at locations where spacers are touching the membrane. These spikes are results of the stagnant flow in the region front of spacers, and they might result in the formation of surface fouling.

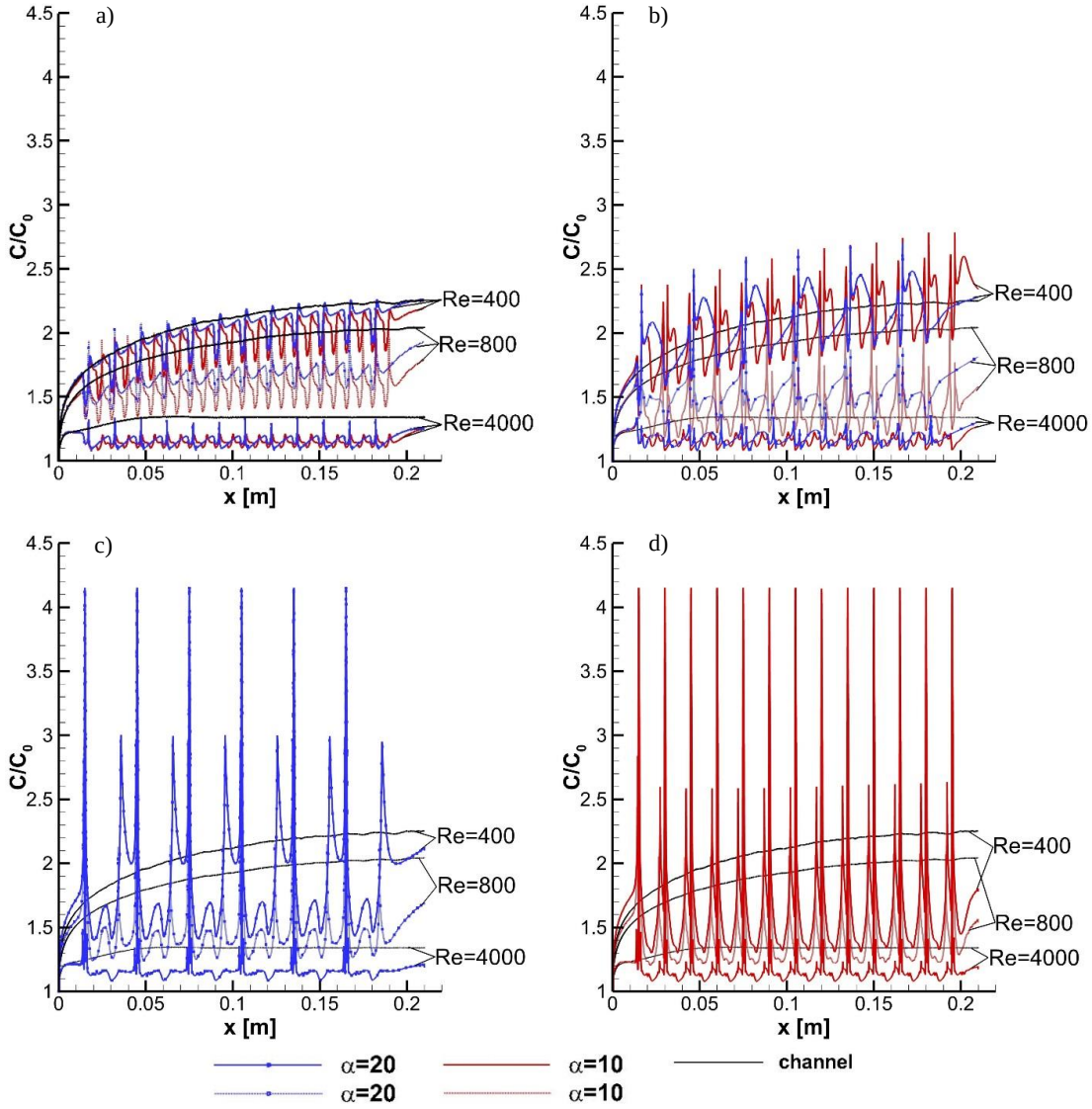

Figure 10: Concentration profiles along the surface of the upper membrane a) e = 1/4 h, α = 20 and α = 10 b) e = 1/8 h, α = 20 and α = 10 c) e = 0, α = 20 d) e = 0, α = 10

Figure 11 illustrates the water fluxes along the upper membrane in the inline and the staggered geometries for α of 10 and 20 at *Re* = 400, 800 and 4000. The water production rate for the membrane system including spacers in all geometries at all flow rates increases when it is compared against the open channel. Figure 11(a) shows the water fluxes in the inline geometry for $\alpha = 20$ and 10. The largest increase in the water

flux through the membrane is obtained at *Re* = 800. The geometry with α = 10 performs slightly better than that of α = 20. Figure 11(b) depicts the water flux in the staggered geometry for *e/h* = 1/8, α of 10 and 20. Similarly, the improvement in the suction rate is the highest at *Re* = 800. Slight or no discernible enhancement is seen in the water flux at *Re* = 400. The nominal value of the permeate rate is very close to that obtained for the open channel at *Re* = 400, as seen in Figure 11(b). Figure 11(c) and 11 (d) illustrate the water flux through the membrane at the upper membrane in the staggered geometry when spacers touch the membrane surface. The best improvement is again attained at *Re* = 800.

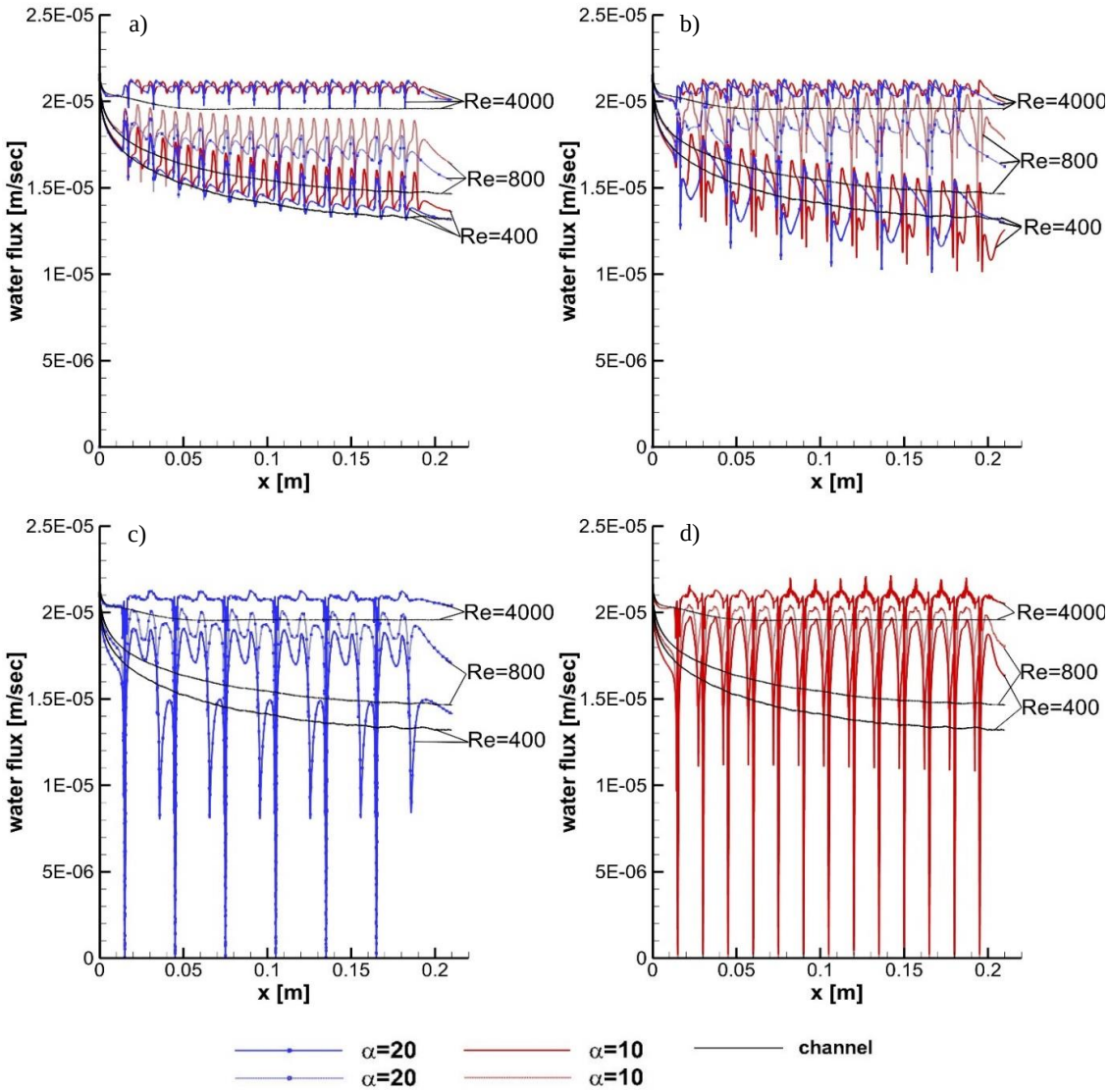

Figure 11: Water flux along the surface of the upper membrane a) e = 1/4 h, α = 20 and α = 10 b) e = 1/8 h, α = 20 and α = 10 c) e = 0, α = 20 d) e = 0, α = 10

Figure 12 depicts the Sherwood number, *Sh*, determined along the surface of the upper membrane. The nominal value of the Sherwood number in the inline and the staggered geometries is higher than that of the open channel at all values of *Re*. As expected the Sherwood number increases as the *Re* is increased in all geometries including the open channel. The greatest enhancement in the Sherwood number is

reached at the highest flow rate, as shown in Figure 12. The local Sherwood exhibits strong dependence on the spacers' configuration.

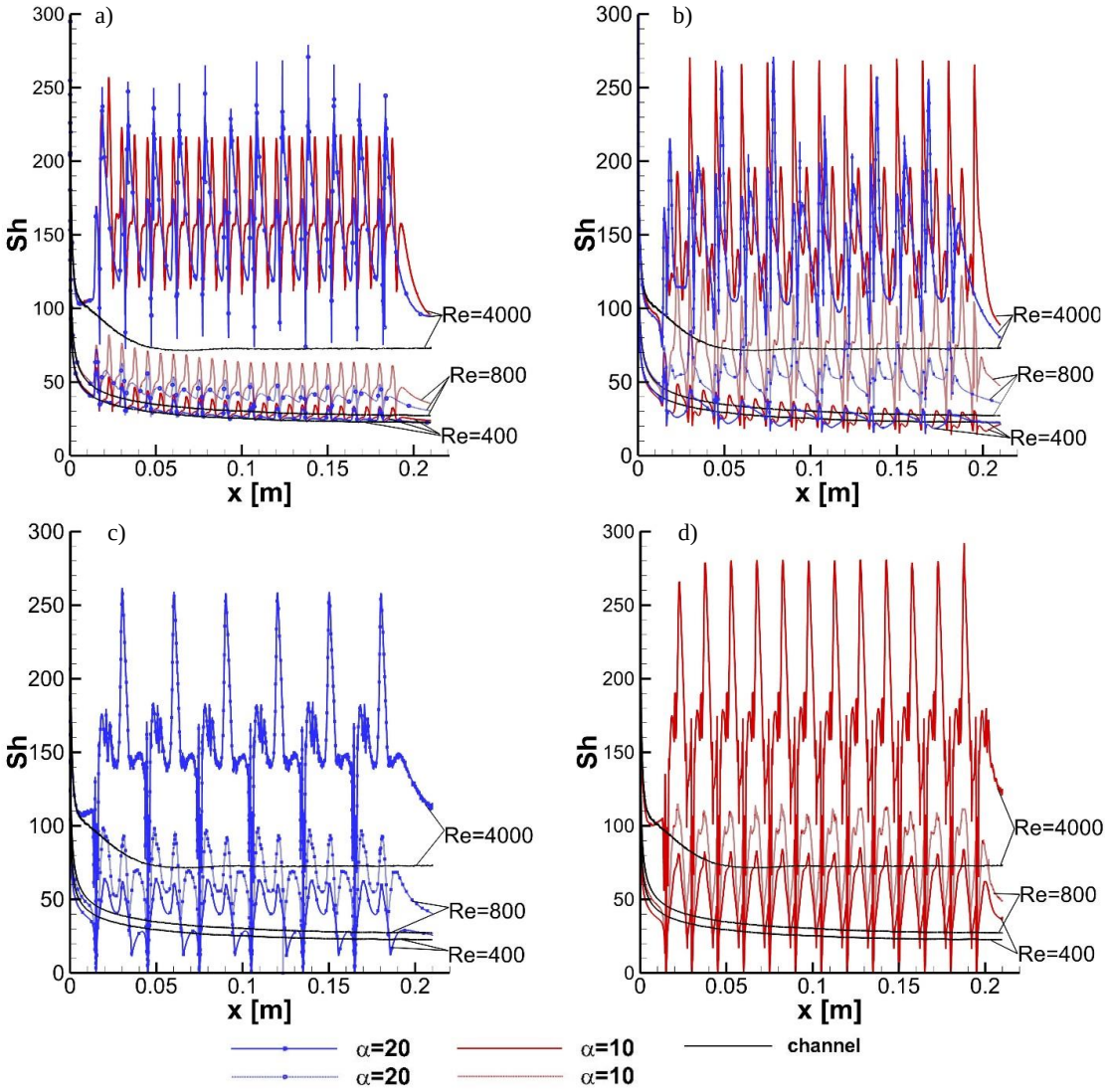

Figure 12: Local Sherwood number along the surface of the upper membrane a) e = 1/4 h, α = 20 and α = 10 b) e = 1/8 h, α = 20 and α = 10 c) e = 0, α = 20 d) e = 0, α = 10

Table 1 lists the pressure drop in the feed channel, the average value of the water flux and the Sherwood number in all geometries at *Re* of 400, 800 and 4000. In order to eliminate the inlet and the outlet effects, the average values of v_w and *Sh* are calculated

from the local values determined in the region 0.01 m ≤ x ≤ 0.2 m. The average values of the Sherwood number and the suction rate increase as the flow rate increases in all geometries. The Sherwood number for α = 10 is higher than that of α = 20 at all *Re*. As it is expected the pressure drop increases as the flow rate increases. As it is also expected the pressure drop is higher for α = 10 in all geometries. Table 1 illustrates that the pressure drop in the feed channel is strongly dependent on the spacers' configuration. The highest values of the mass transfer coefficient occurs in the geometry of e = 0 for α = 10, yet the pressure drop is not the highest in this geometry. It is noted that the highest pressure drop occurs in the staggered geometry with e = 1/8 h for α = 10, as shown in Table 1.

	channel			Channel with inline spacers e=1/4 h						Staggered spacers e=1/8 h	
				α=20			α=10			α=20	
Re	$\lvert\Delta p_x\rvert$ [Pa]	$\overline{v_w}\times10^{-5}$ [m/s]	$\overline{Sh}$	$\lvert\Delta p_x\rvert$ [Pa]	$\overline{v_w}\times10^{-5}$ [m/s]	$\overline{Sh}$	$\lvert\Delta p_x\rvert$ [Pa]	$\overline{v_w}\times10^{-5}$ [m/s]	$\overline{Sh}$	$\lvert\Delta p_x\rvert$ [Pa]	$\overline{v_w}\times10^{-5}$ [m/s]
400	106	1.438	26.7	471	1.484	28.6	822	1.547	31.5	456	1.44
800	204	1.565	31.8	1309	1.732	42.3	2407	1.798	49.6	1337	1.821
4000	1702	1.965	74.9	22949	2.078	155.1	42398	2.084	161	22461	2.063

Table 1: The pressure drop , the average water flux and the Sherwood number in inline geometry.

	Staggered spacers e=1/8 h				Staggered spacers e=0					
	α=20	α=10			α=20			α=10		
Re	$\overline{Sh}$	$\lvert\Delta p_x\rvert$ [Pa]	$\overline{v_w}\times10^{-5}$ [m/s]	$\overline{Sh}$	$\lvert\Delta p_x\rvert$ [Pa]	$\overline{v_w}\times10^{-5}$ [m/s]	$\overline{Sh}$	$\lvert\Delta p_x\rvert$ [Pa]	$\overline{v_w}\times10^{-5}$ [m/s]	$\overline{Sh}$
400	27.2	864	1.468	28.5	300	1.632	38.1	467	1.7	49.9
800	53.4	2637	1.92	73.5	1011	1.833	63.5	1672	1.845	73.9
4000	139.7	49446	2.078	155.8	20335	2.045	154.8	36763	2.046	167.6

Table 1: (Continued)

Figure 13 illustrates images from the transient simulation at t = 0.2078 sec (or at dimensionless time, τ = 148.5). Contours of the stream-wise component of the velocity are shown in Figure 13(a), and contours of the normalized salt concentration are shown

in Figure 13(b). The simulations are conducted in the inline geometry for α = 20 at *Re* = 800. The velocity and the concentration field obtained for the transient simulations can directly be compared against the results of steady simulations presented in Figure 9 for the same conditions. The numbers (1, 2, and 3) in the figure caption denote the location where images are acquired and they are identical to those shown in Figure 9. The vortex shedding from spacers enhances the momentum mixing in the region near and away from the spacers. The flow induced by the Karman vortex street increases the concentration mixing as shown in Figure 13(b1), 13 (b2), and 13 (b3). The results presented for the steady simulations denote the time average of the transient velocity and the concentration fields, as shown in Figure 13.

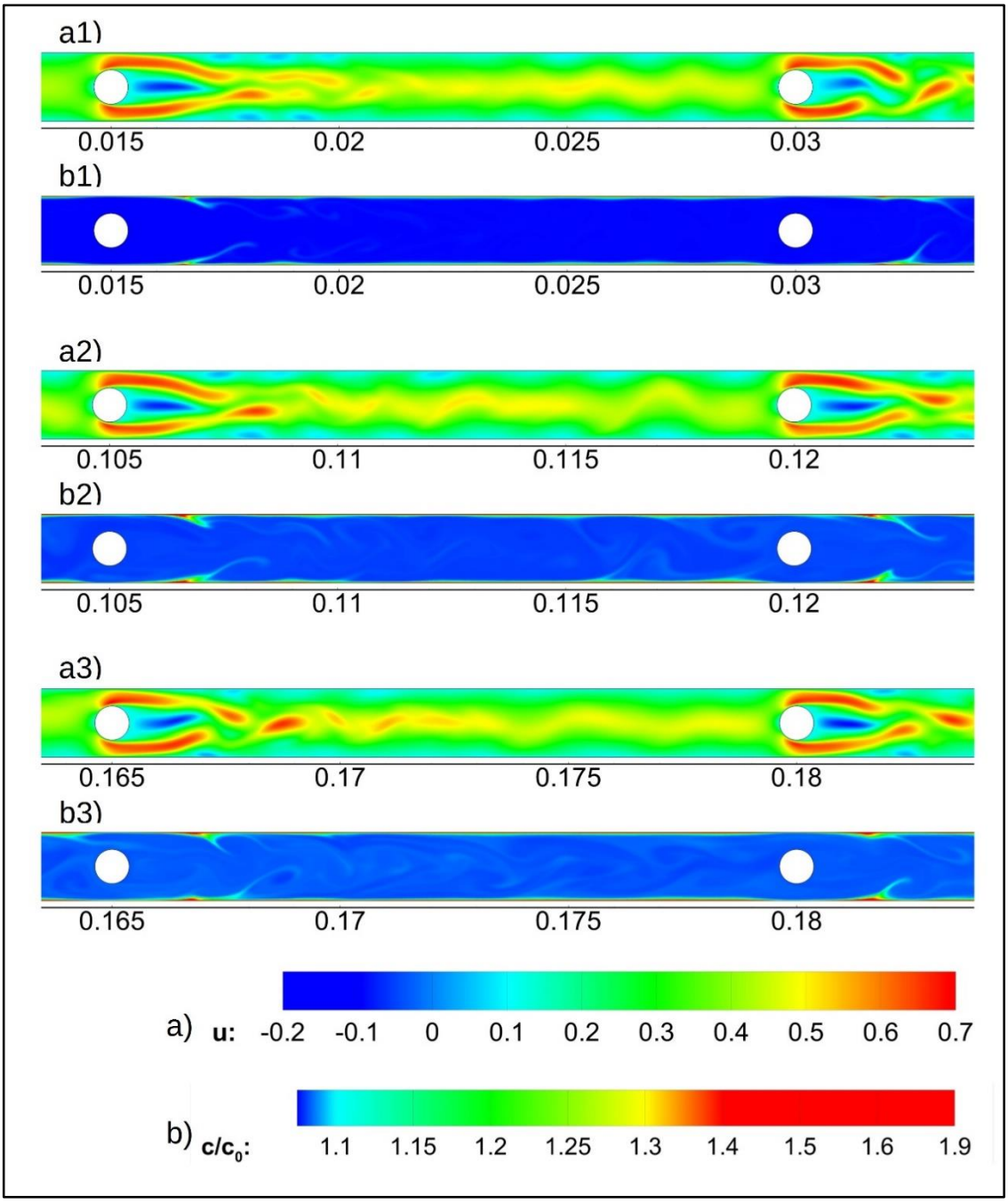

Figure 13: Transient simulation at Re=800, α=20 and e=1/4 h @t=0.2078 [sec] (τ =148.5). a1), a2), and a3) velocity contours, and b1), b2), and b3) concentration contours at different locations along x-axis.

Vorticity contours shown in Figures 14(a1), 14(a2) and 14 (a3) reveal the intensity of the secondary flows induced by the vortex shedding. The vortices shed by the spacers dissipate as they are convected away from the cylinders. Figure 14(a) illustrates that the flow induced by the vortex shedding in the wake region of spacers is strongly influenced by the proximity of the walls. The similar flow structures are reported by Singha and Sinhamahapatra [46] and Sahin and Owens [47] in the channel containing spacers with the same blockage ratio at the similar flow rates. The lift coefficient calculated for the spacer on the first row proves that the flow is nearly perfectly periodic at Re = 800. The power spectral density of the lift coefficient signals yield the dimensionless frequency, the Strouhal number, $St = fd/U_{ave} = 0.252$. Here f is the frequency of the fluctuations manifested by the vortex street behind the spacers. Mettu et al. [48] found the Strouhal number to be 0.25 for a blockage ratio of 0.4 at Re = 800. The Sherwood number calculated at three different axial location, P1, P2, and P3, from the transient and steady state results are compared, the axial locations selected are x = 15, 18, and 22.5 mm, respectively. The solid lines denote the Sh determined from the transient simulations and the dashed lines denote the Sh determined for the steady state results. Sh calculated from the steady state simulations is not too different than that calculated from the transient simulations, as shown in Figure 14(c). These results imply that steady state simulations provide an accurate assessment of the membrane performance in the geometries considered here.

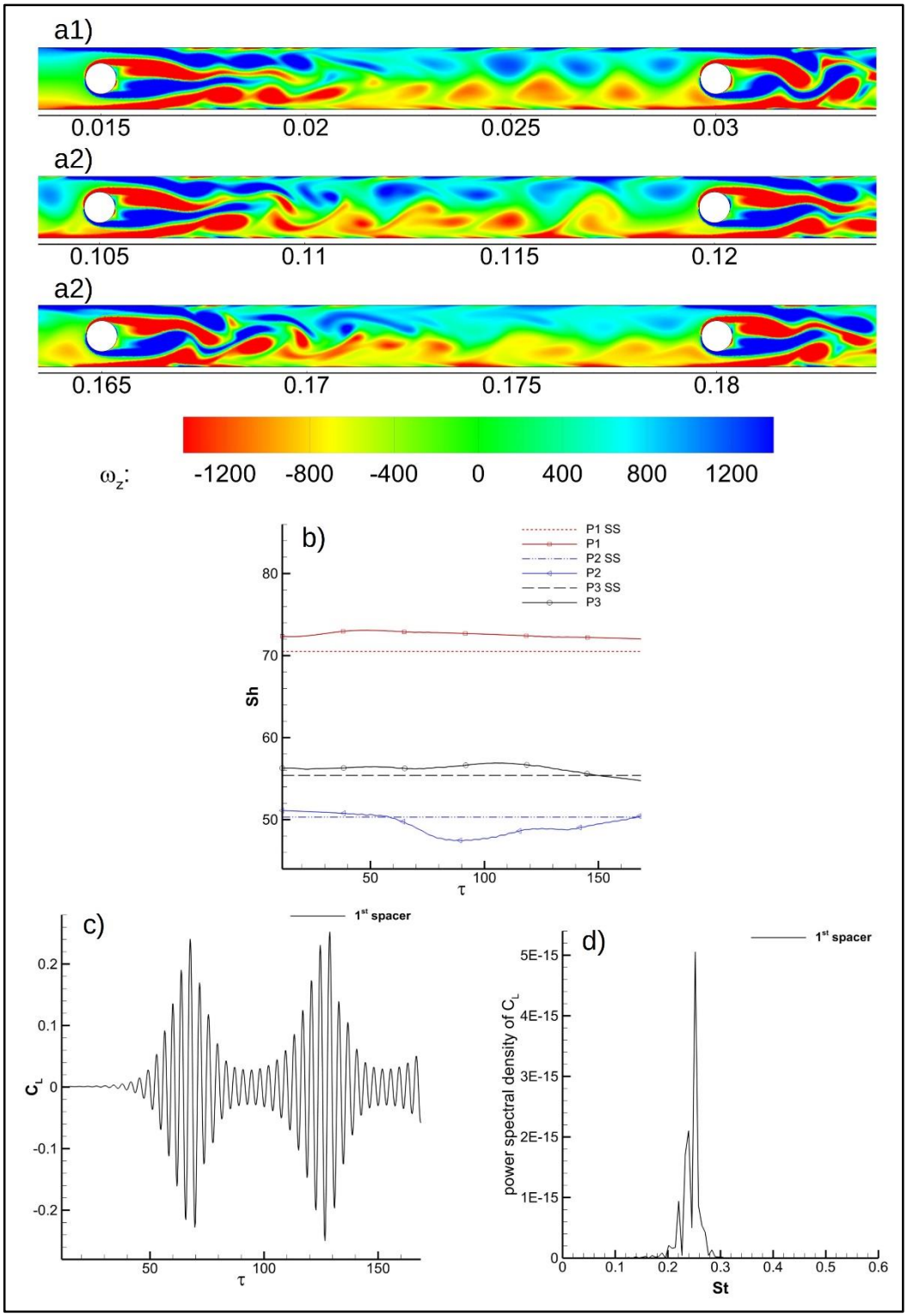

Figure 14: Transient simulation at Re=800, α=20 and e=1/4 h. a1), a2), and a3) are vorticity contours at different locations along x-axis @t=0.2078 [sec] (τ =148.5), b) local Sh number at three different points, c) lift coefficient of the first spacer vs. non-dimensional time, and d) the power spectral density of the lift coefficient signal.

3.1.3. CONCLUSION

Numerical simulations have been conducted to study the performance of Reverse Osmosis membrane for a brackish water desalination process. The momentum and mass transport equations govern the flow of the brackish water in the feed channel. The mass flux of water through the membrane varies with the local pressure and the concentration. The SST k-ω turbulence model has been selected to perform the steady turbulent flow simulations while the LES has been selected to perform the transient turbulent flow simulations. Three flow rates, Re = 400, 800, and 4000, are considered in the inline and the staggered geometries. Momentum mixing resulted from turbulators improves the performance of the membrane greatly at all flow rates considered. The concentration polarization is mitigated in the inline and the staggered geometries at all flow rates. The results clearly indicate that the Sherwood number is strongly influenced by Re and the arrangement of the spacers. This study proves that, in order to enhance the brackish water desalination by the RO membrane, the arrangement and the spacing of turbulators must be optimized for a given range of Re. Pressure drop should be considered as an important part of the of optimization process.

3.2. NON-CIRCULAR SHAPED SPACERS

3.2.1. GEOMETRY

Simulations are conducted for three different shaped spacers: circular, diamond and triangular. The schematic of the membrane composite is illustrated in Figure 15. The gap between the plates, h, is 1.5 mm. The spacing between two successive spacers, s, is 7.5 mm. d/h is the blockage ratio where the span of the spacer in the channel, d, is 0.75 mm. The inline arrangement of the spacers is used in the present study. e/h = 1/4, where e is the distance between the edge of the spacer and the wall. Simulations are performed for values of the Reynolds numbers of 100, 300, 1000, and 2000. The results in this section were published in Ref. [49].

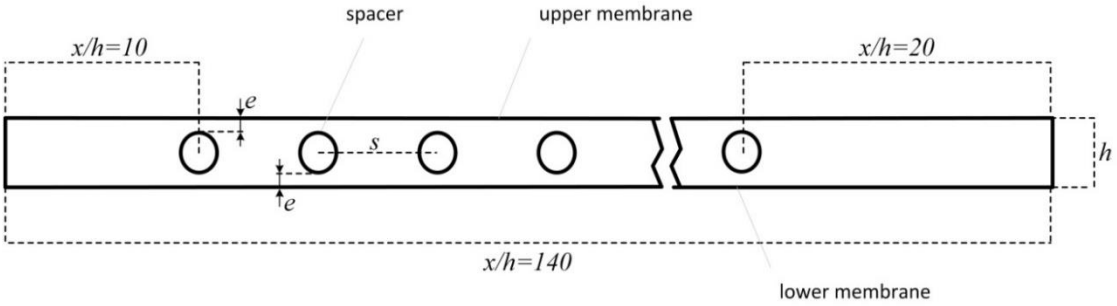

Figure 15: Schematic of the membrane composite.

3.2.2. RESULTS

The present work simulates the flow in the feed channel of a RO membrane for desalination of brackish water. The membrane is treated as a functional surface, and the flow is considered to be turbulent when Re > 400. The simulations are conducted for

three different spacer shape: a circular, a diamond, and a triangular. Results are presented for Re = 100, 300, 1000, and 2000.

Figure 16 shows the steady state contours of the stream-wise component of velocity, u, and the concentration ,c/c_0, in the feed channel containing circular, diamond and triangular cross-sectioned spacers in inline arrangement. Velocity and concentration contours are displayed between 11^{th} and 12^{th} spacers at $Re = 300$. a) images denote the velocity contours and b) images denote the normalized concentration contours. The velocity contours show that the spacers disrupt the flow repetitively in the feed channel which causes the momentum mixing. The spatial flow structure in the wake of spacers differ slightly in these geometries at *Re* = 300. The momentum mixing influences the concentration field as illustrated in Figure 16. The concentration boundary layer near the membrane is slightly thinner in the channel with the circular spacers than those with the diamond and triangular shaped spacers.

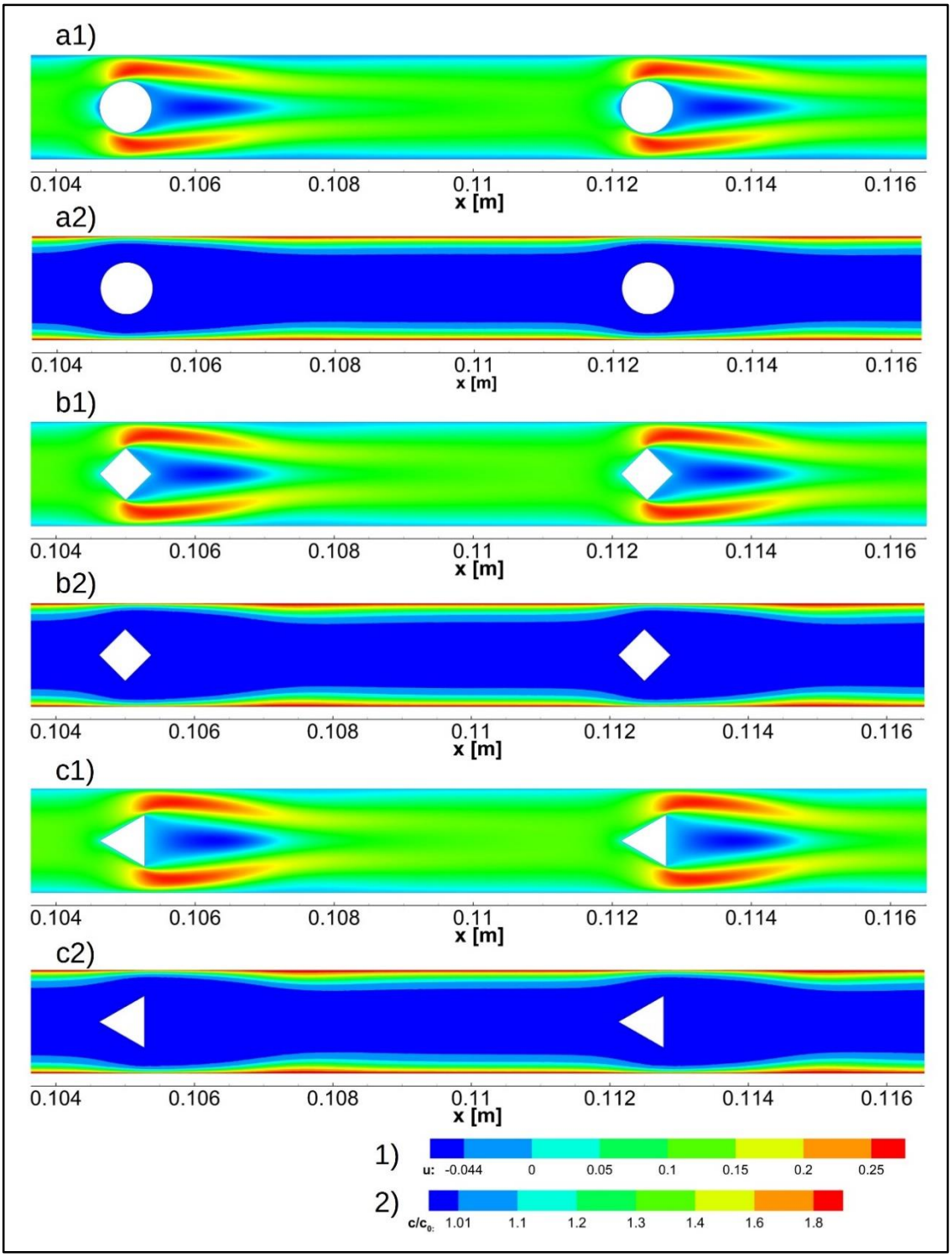

Figure 16: Contours of the stream-wise component of the velocity (a1, b1, c1) and contours of the normalized concentration (a2, b2, c2) at $Re = 300$ for three different shaped spacers.

Figure 17 depicts the water flux at the surface of the upper membrane for circular, diamond, and triangular shaped spacers at Re = 100, 300, 1000, and 2000. In Figure 17, the blue solid lines represent *Re* = 100, the black dashed lines represent *Re* = 300, the red dashed lines represent *Re* = 1000, and the black dashed lines represent Re = 2000 for the three different shaped spacers. The same legend is used for the concentration profiles and the Sherwood number calculated along the surface of the upper membrane, as illustrated in Figures 18 and 19, respectively. The water flux through the membrane increases significantly as Re is increased for all three different shaped spacers used in the present study. The level of the water flux is not very sensitive to the shape of the spacers. The more noticeable variation in the water flux is attained at *Re* = 300, as shown in Figure 17.

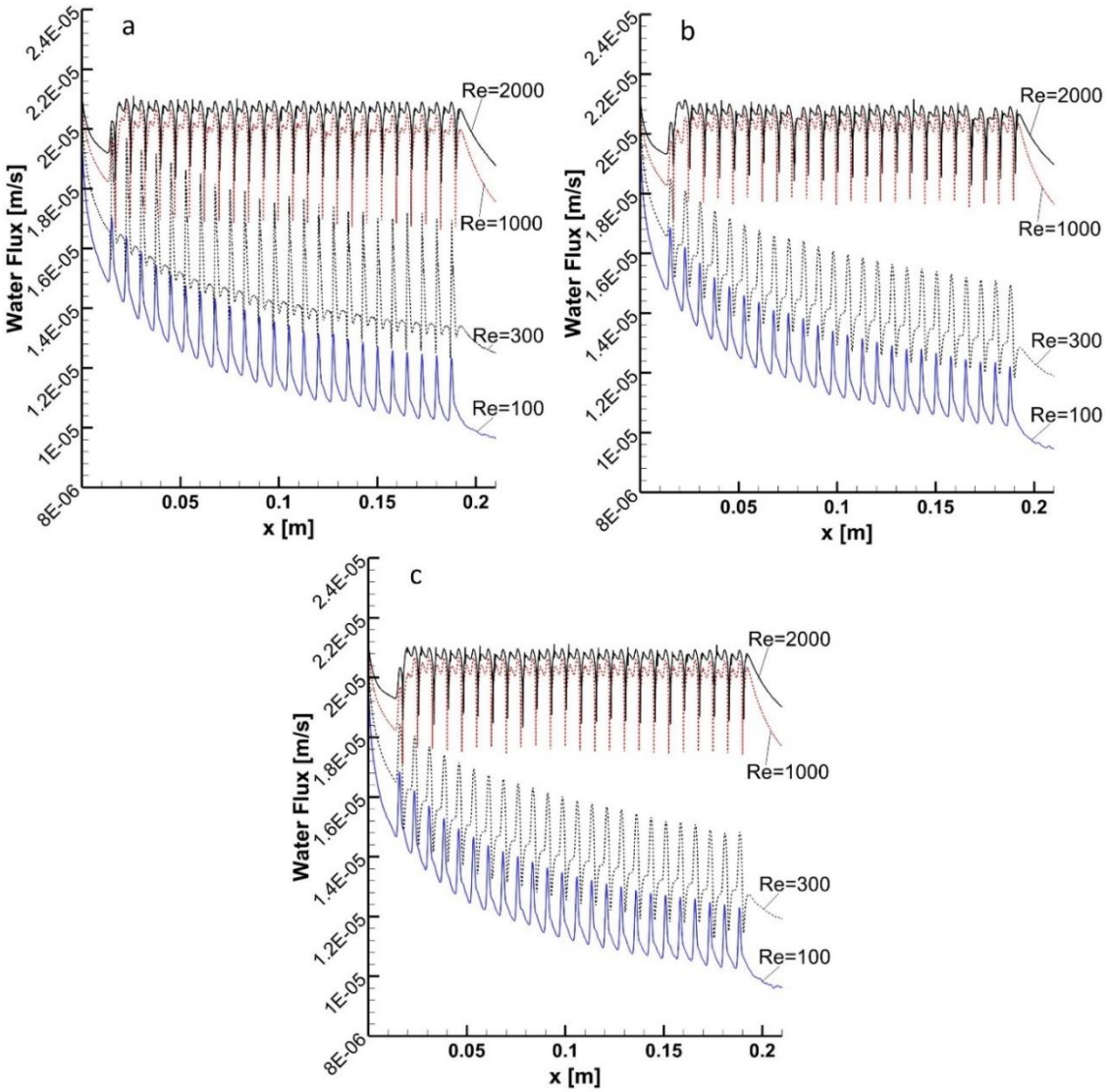

Figure 17: Water flux profiles along the surface of the upper membrane for a) circular b) diamond, and c) triangular shaped spacers. Profiles are obtained at Re = 100, 300, 1000 and 2000.

Figure 18 illustrates the normalized concentration profiles along the surface of the upper membrane for three different shaped spacers at *Re* = 100, 300, 1000, and 2000. The concentration polarization along the surface of the upper membrane is alleviated at higher *Re* for all geometries employed here. Similar to the water flux profiles, the concentration profiles differ only slightly in three geometries.

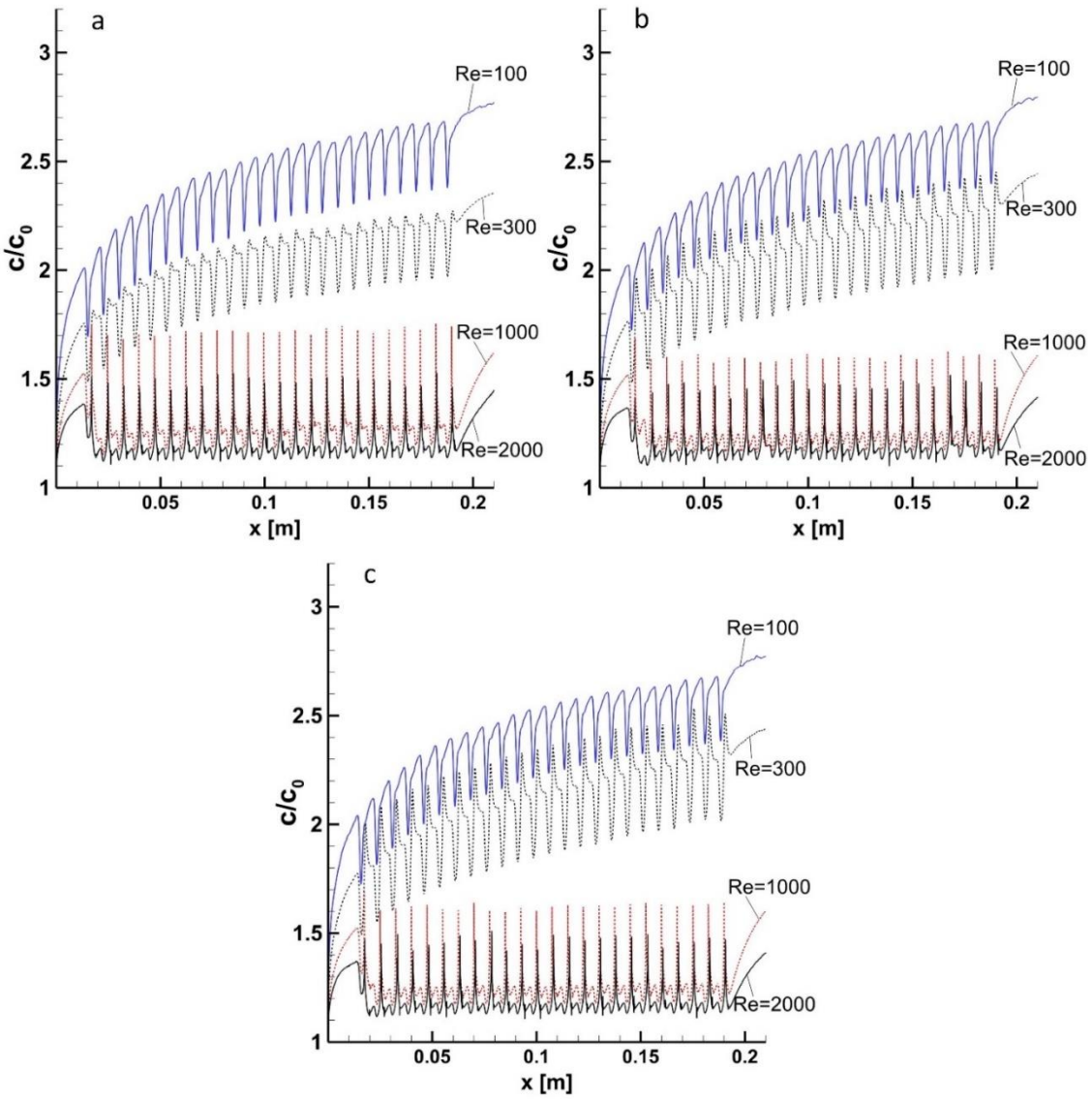

Figure 18: Normalized concentration profiles along the surface of the upper membrane for a) circular b) diamond, and c) triangular shaped spacers. Profiles are obtained at Re = 100, 300, 1000 and 2000

Figure 19 depicts the local Sherwood number along the surface of the upper membrane for three different shaped spacers in the inline arrangement. The local Sherwood number is calculated for *Re* = 100, 300, 1000 and 2000. The Sherwood number displays a periodic dependence along x following the spacers. The Sherwood number increases three to four folds as *Re* is increased to 2000 compared at low flow

rate, as shown in Figure 19. The Sherwood number is a good indicator of the membrane performance since it eliminates the effects of the concentration conditions at the inlet and the length of the computational domain. The average value of the Sherwood number increases as the flow rate is increased. This must be attributed to the momentum mixing induced by the Karman vortex street. Periodically shedding vortices are expected behind the spacers at the flow rates considered here in this study. These vortices can only be predicted by the transient simulations using large eddy simulations or direct numerical simulations. Such high fidelity simulations are not in the scope of this study, but it can be considered as a future work to investigate the transient effects on the membrane performance.

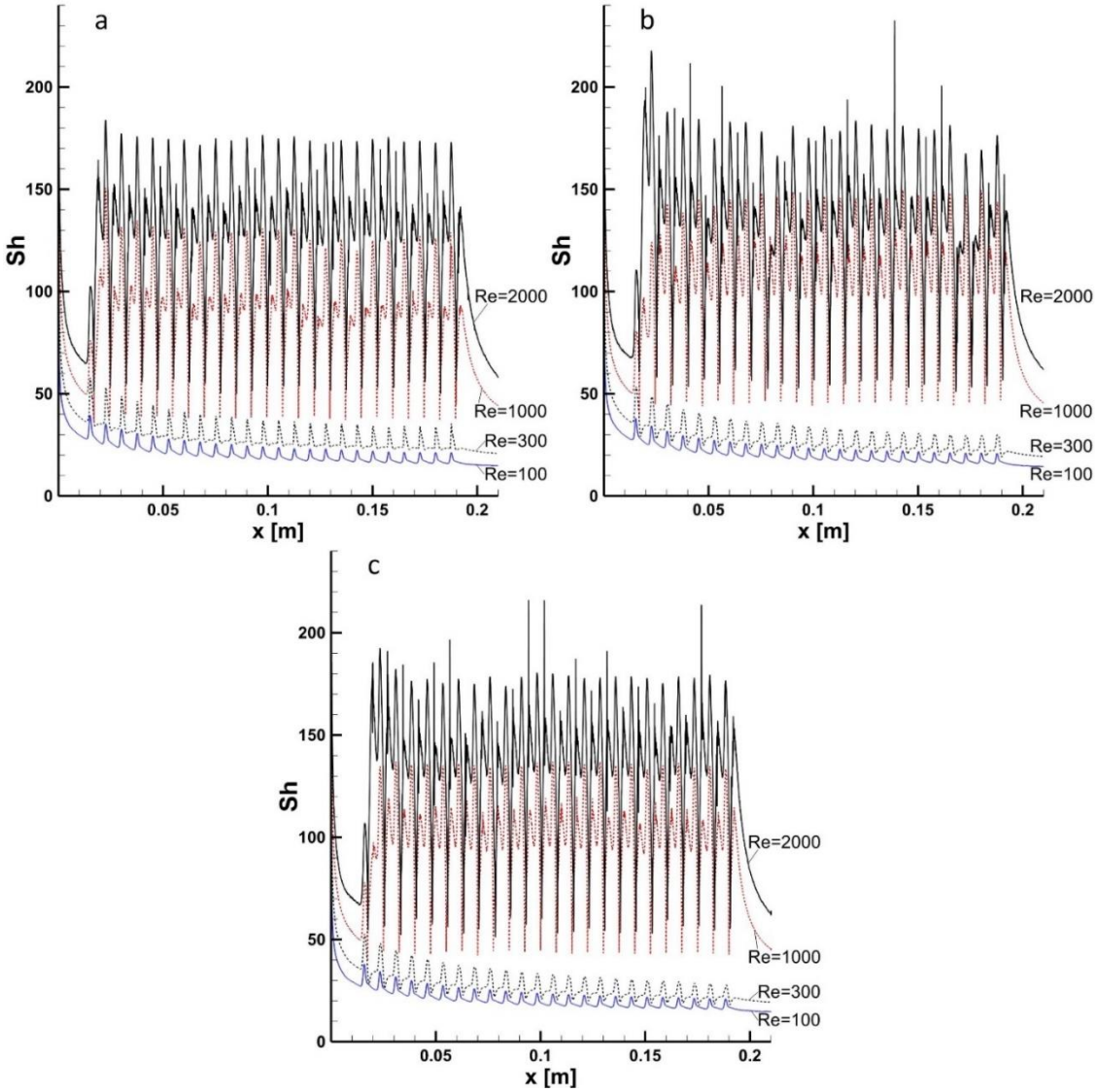

Figure 19: Local value of the Sherwood number calculated along the surface of the upper membrane for a) circular b) diamond, and c) triangular shaped spacers. Profiles are obtained at Re = 100, 300, 1000 and 2000.

3.1.3. CONCLUSION

This study proves that the velocity and the concentration fields in the feed channel have a profound impact on the membrane performance in brackish water desalination. The water production rate can be adjusted by controlling the flow rate in the feed channel. The placement of the spacers in the feed channel promotes momentum mixing,

that in turn enhance the membrane performance. For the range of *Re* considered and for the inline arrangement, the shape of the spacers' cross-section hardly influences the membrane performance. The effect of the flow rate on the membrane performance in the feed channel including spacers is profound. This study proves that spacers should be an integral part of the membrane design in brackish water desalination. The flow rate is one of the very important variables in the optimization process.

CHAPTER 4: THREE DIMENSIONAL ANALYSES – LADDER-TYPE SPACERS

4.1. GEOMETRY AND MESH STUDY

The schematic of computational domain is illustrated in Figure 20. The top and the bottom surface is an RO membrane. The gap between membranes is $h = 1.5$ mm. Sixteen uniformly spaced circular cylinders of diameter, $d = \frac{1}{2}h$, are placed in the mid-plane between the membranes to promote mixing in the feed channel. The axes of cylinders are parallel to the membranes and perpendicular to the primary flow direction. The length of the inlet and the outlet region is selected as 6 h and 15 h, respectively, to minimize the effect of the imposed inlet and outlet velocity boundary conditions on the characteristics of the flow in the spacer bank region. Flow simulations are conducted for Re = 100, 400, 600 and 800. The Reynolds number is defined as $Re = 2hU_{ave}/\nu$, where h is the channel height, U_{ave} is the inlet average velocity, and ν is the kinematic viscosity.

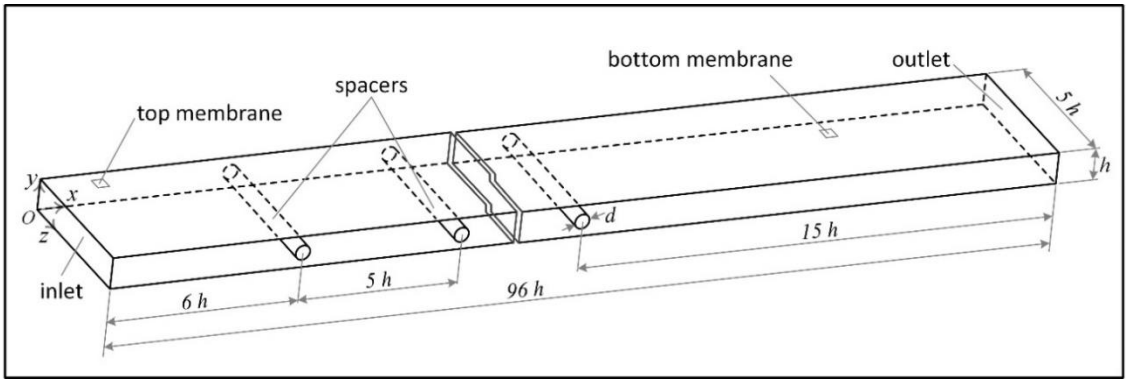

Figure 20: Schematic of flow geometry.

A mesh optimization study is performed using two mesh sizes: 20 million (M1) and 30 million (M2) elements. Profiles of the stream-wise component of the velocity are calculated across the gaps between membrane (a) across the first spacer at $x/h = 6$ and $z/h = 2.5$ and (b) in the wake of the first spacer at $x/h = 7$ and $z/h = 2.5$. Velocity profiles are shown in Figure 21 for both meshes. The friction coefficient, f, is also calculated for the mesh M1 and mesh M2. The friction coefficient is determined from equation (19) using average pressure drop across the part of spacer bank from $x = 38\ h$ to $x = 77\ h$. The velocity profiles obtained for M1 and M2 are similar; implying that mesh size M2 is enough to ensure mesh independency. The friction coefficient is calculated to be 0.320 and 0.323, respectively, for M1 and M2 mesh; confirming that the mesh independency might be achieved with M2. Stronger argument could be made by refining mesh further. The size of computation and the available computational resources make that to be a difficult task. Simulation results presented in the present study are obtained using M2 mesh.

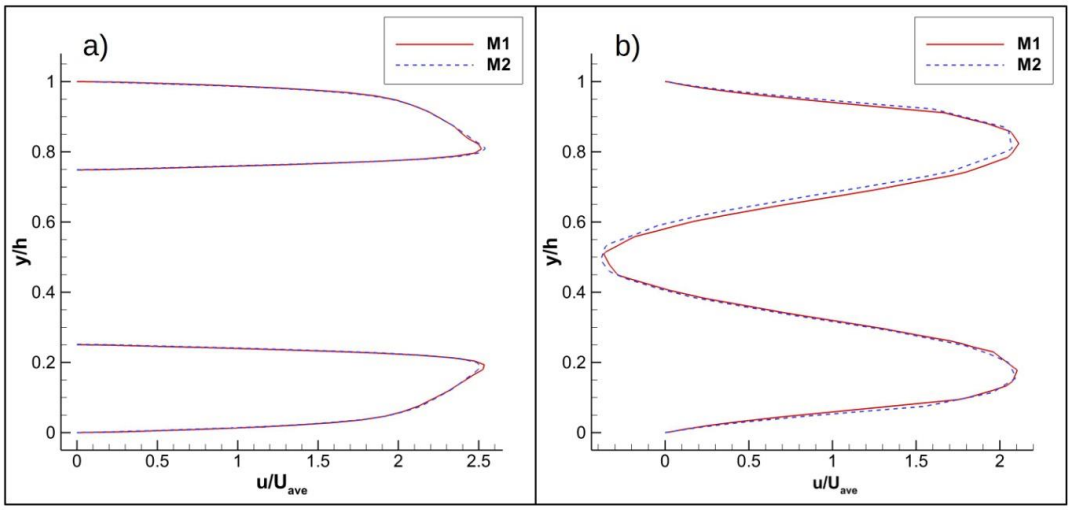

Figure 21: Profiles of stream-wise component of the velocity for mesh M1 and M2 a) at x/h = 6 and b) at x/h = 7.

4.2. RESULTS

The results of steady three dimensional flow simulations are presented for $Re =$ 100, 400, 600 and 800. Comparison between results obtained from three dimensional and two dimensional simulations are made to determine the influence of three dimensional flow structures on the membrane performance. Two dimensional flow modeling consider velocity and concentration field in the z-direction to be uniform. The laminar flow model is used for $Re = 100$, and SST k-ω turbulence model is used for $Re =$ 400, 600 and 800 to simulate mass and momentum transports in the feed channel.

Figure 22 illustrates contours of the stream-wise component velocity at $Re = 100$, 400, 600 and 800. Images are shown at three z planes ($z/h =$ 0.4, 2 and 3.6) for each value of Re. The wake region behind spacers becomes larger as Re is increased. High speed flow region around the cylinder is also stretched in the stream-wise direction as Re is increased, as shown in Figure 22. Three dimensional flow structures and their strength cannot easily be distinguished from these images. Primary flow in the stream-wise direction dominates the secondary flows induced by the flow transitions. These flows transitions are well-documented in the literature and they are expected to onset for values of Re above the criticality. The secondary flows manifest themselves nearly periodic flow structures in the span-wise direction.

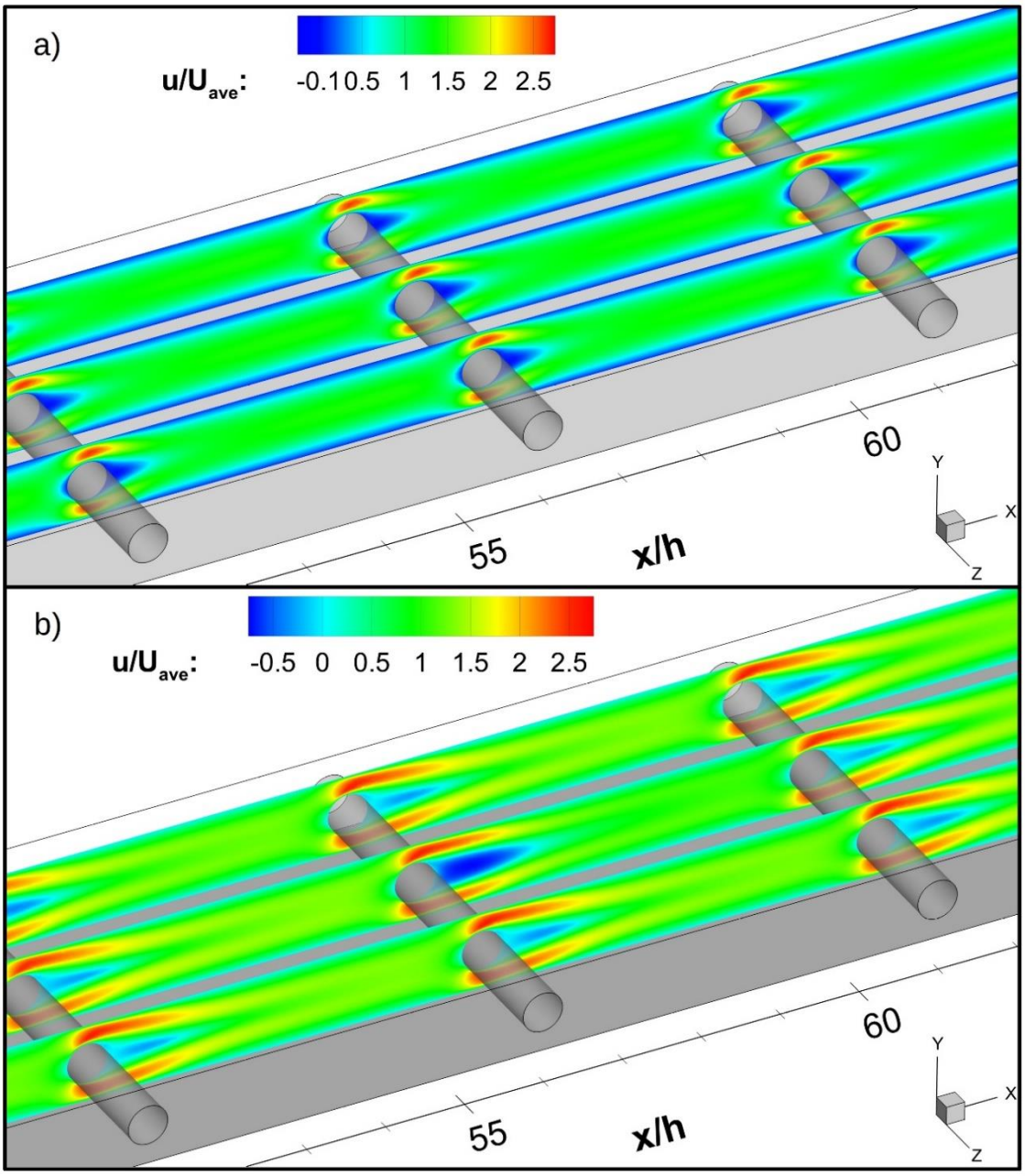

Figure 22: Contours of the stream-wise component of the velocity acquired at z-planes of $z/h = 0.43$, 2, and 3.6 for values of the Reynolds number of a) 100, b) 400, c) 600, and d) 800.

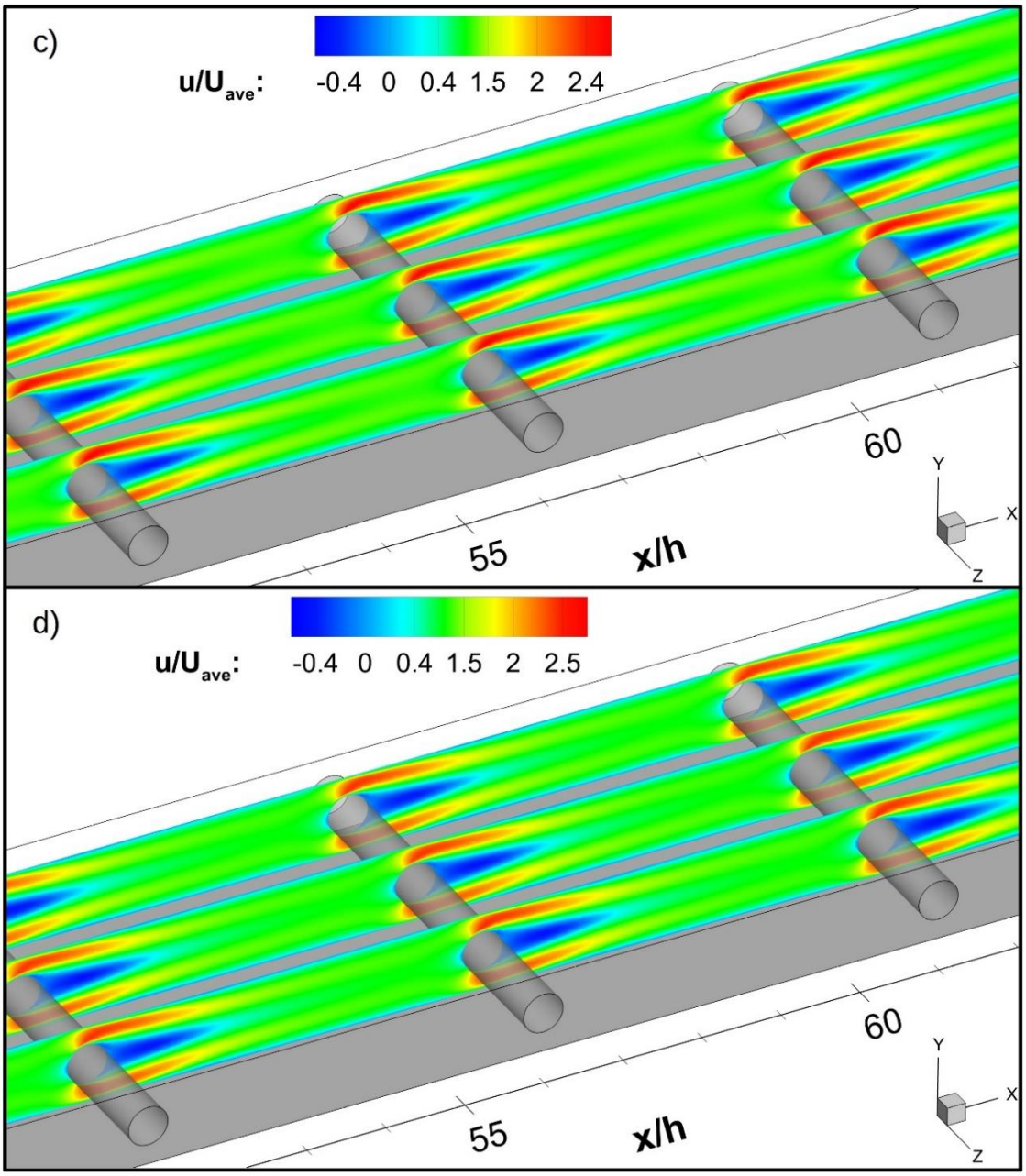

Figure 22: (Continued)

Figure 23 shows contours of the stream-wise components of the velocity at the mid-plane ($y/h = 0.5$) between membranes at $Re = 100$, 400, 600 and 800. The

presence of secondary flows is very clear. At $Re = 100$ the flow is nearly uniform in z-direction and it can be characterized as two dimensional, as shown in Figure 23a. Velocity contour depicted in Figure 23b for $Re = 400$ shows vast contrast to the velocity contour obtained for $Re = 100$. The flow becomes three dimensional as a result of induced secondary flows. It is clear that the critical value of Re for the onset of three dimensional flow is between 100 and 400. It has been reported that transition to the three dimensional flow occurs between Re of 100 and 200 for these geometries [27]. Velocity contours at $Re = 600$ and 800 exhibit three dimensional flow structures with a lesser intensity relative to the primary flow, as shown in Figure 23c and 23d. These three dimensional flow structures can have a strong influence on the membrane performance, the concentration polarization and the potential fouling along the surface of the membrane.

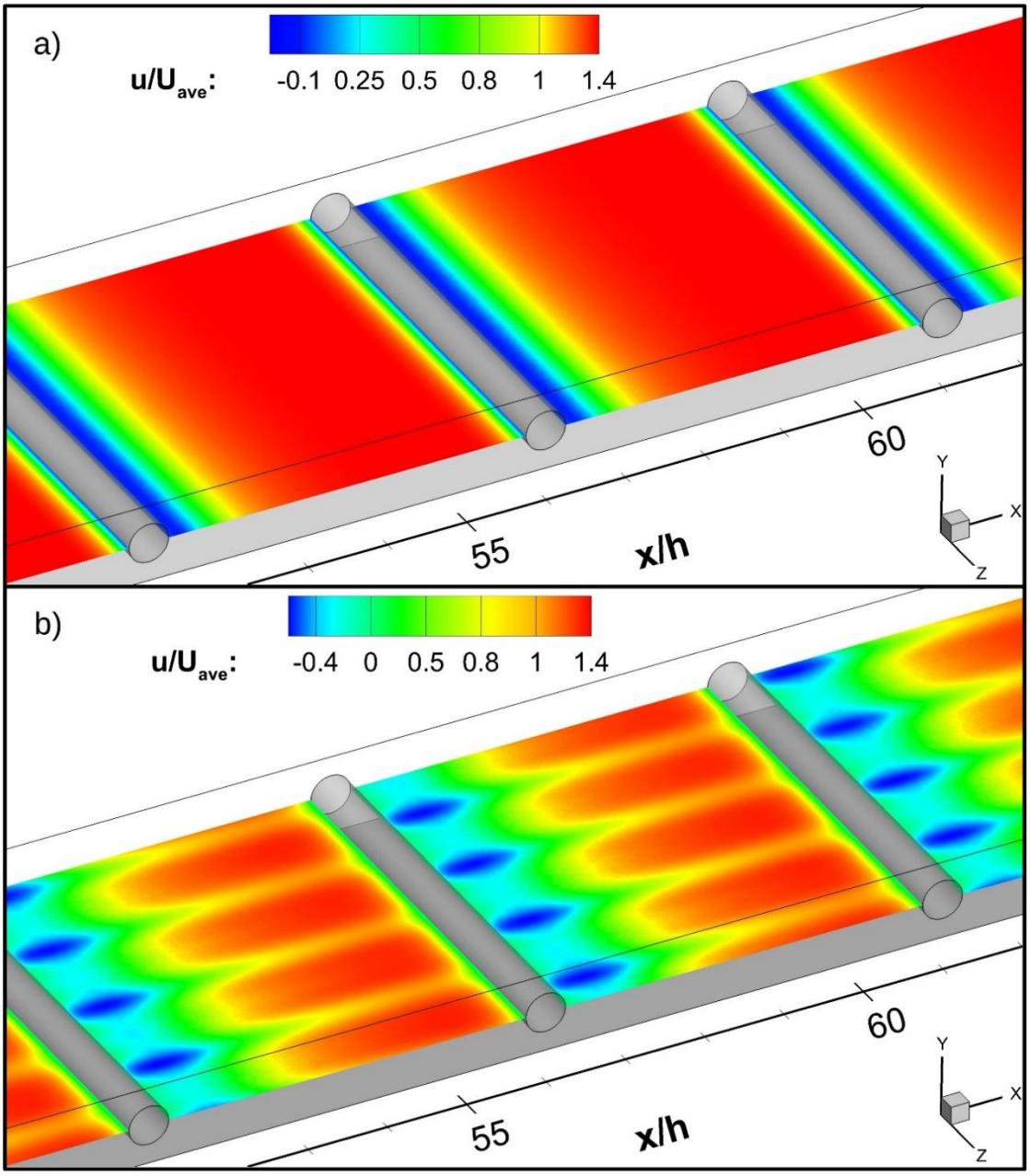

Figure 23: Contours of the stream-wise component of the velocity acquired at the mid-plane between membranes, y/h= 0.5, for values of the Reynolds number of a) 100, b) 400, c) 600, and d) 800.

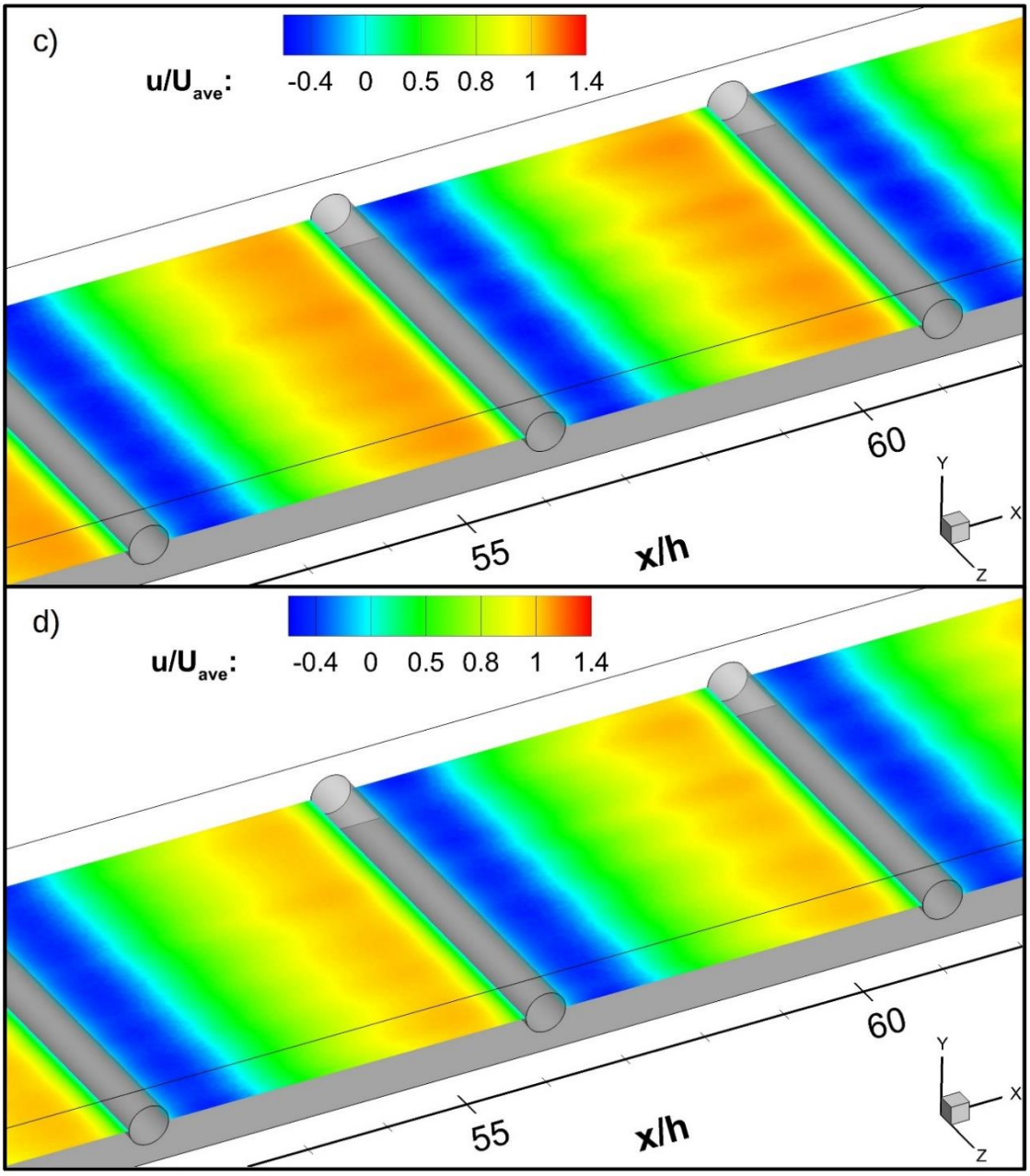

Figure 23: (Continued)

The iso-surface images of the stream-wise component of the velocity are shown in Figure 24. The iso-surfaces are consistent with images of the velocity contours shown in Figure 23. Uniform iso-surfaces are in the span-wise direction for $Re = 100$ while finger-like structures are realized in Figure 24b, 24c and 24d for $Re = 400$, 600 and

800, respectively. Flow structures are more regular for $Re = 400$ compared to those for $Re = 600$ and 800. Finger-like structures fill almost the entire region between spacers; indicating that three dimensional effects caused by flow transitions are strong and do not dissipate quickly away from spacers. Flows in the entire spacer bank region become three dimensional for $Re \geq 400$, as shown in Figure 24.

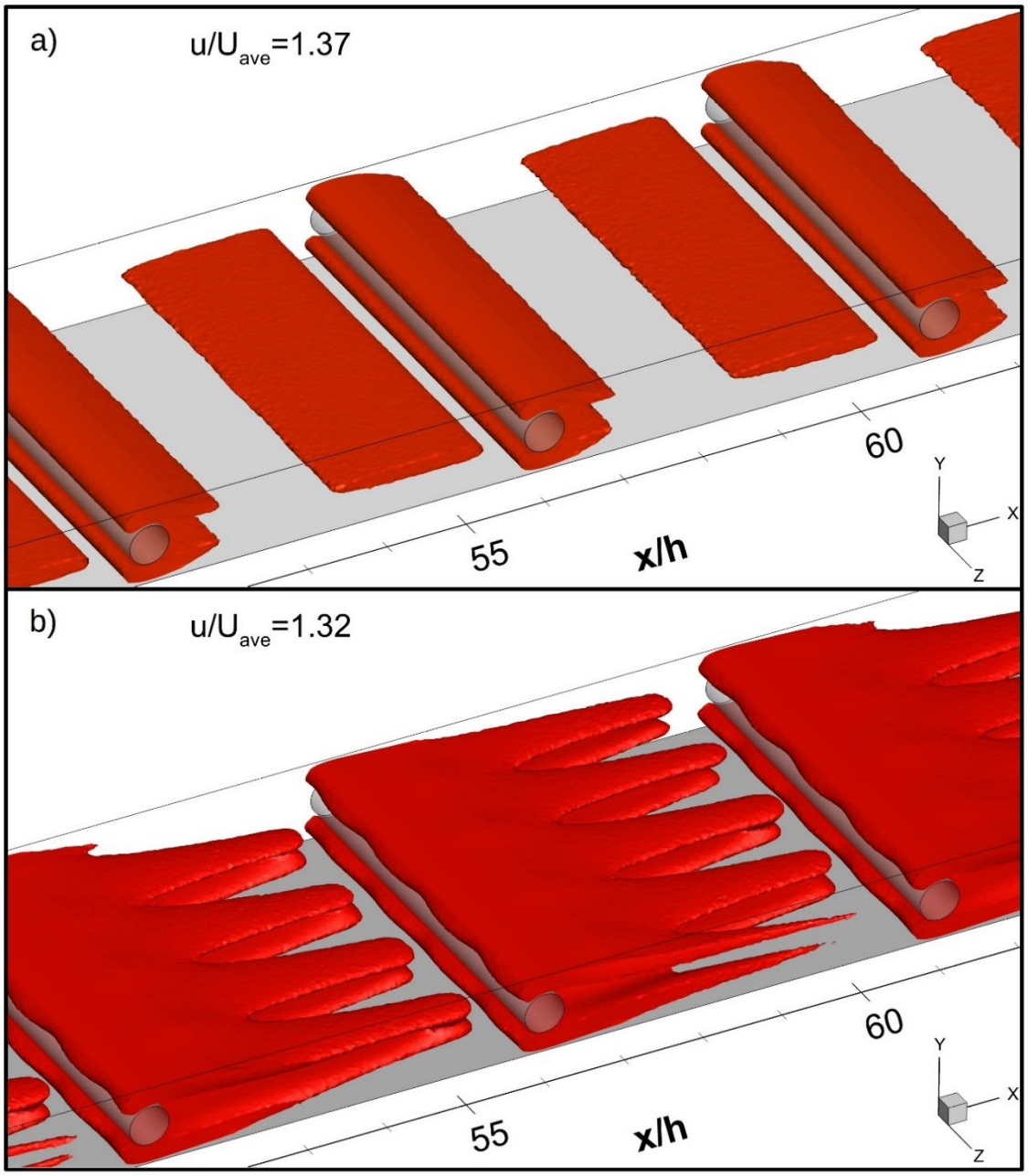

Figure 24: Iso-surfaces of the stream-wise component of the velocity for values of the Reynolds number of a) 100, b) 400, c) 600, and d) 800.

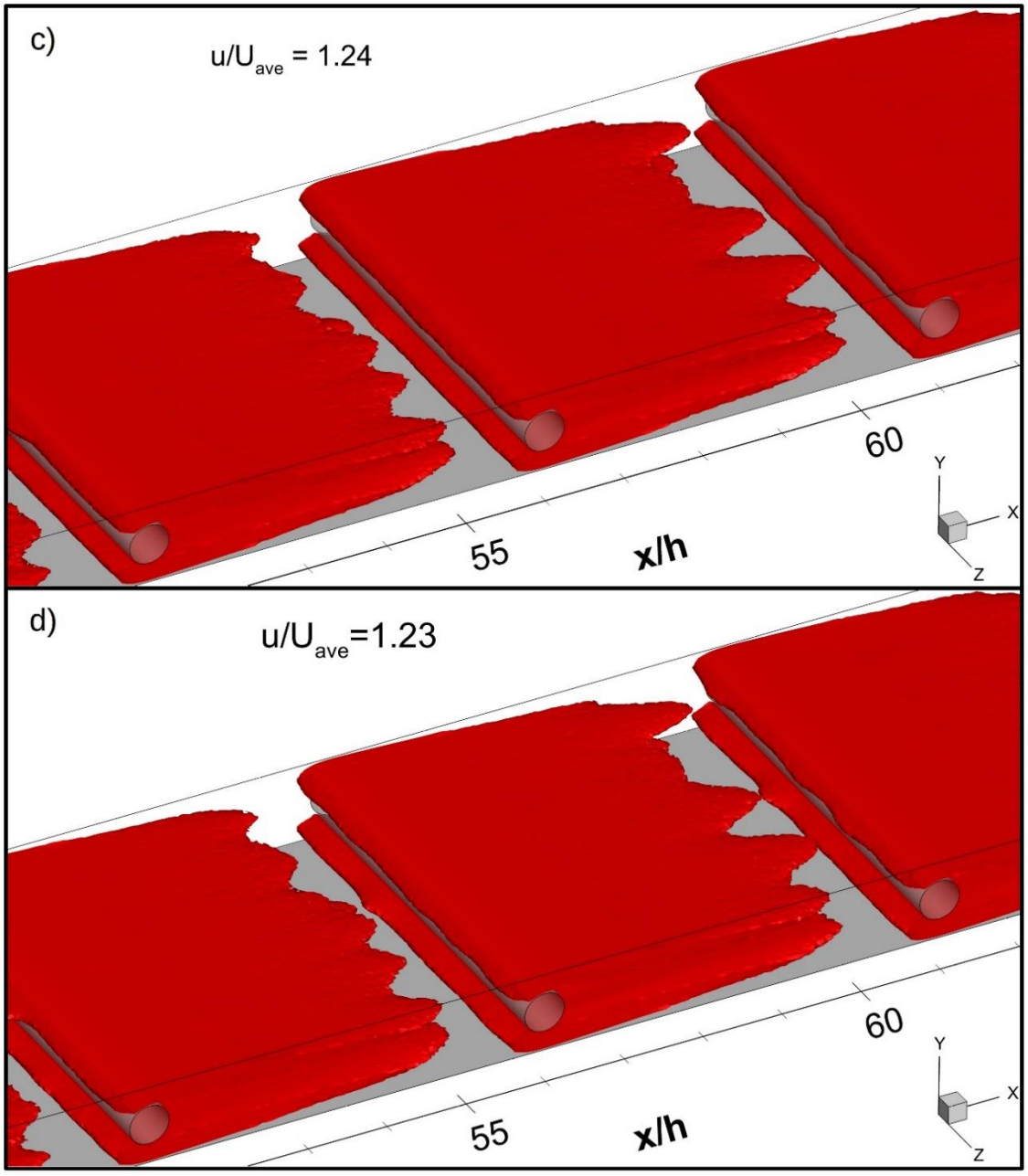

Figure 24: (Continued)

Figure 25 illustrates the iso-surfaces of x and y component of the vorticity. Images labelled by (a) denote iso-surfaces of x component of the vorticity and while images labelled by (b) denote y component of the vorticity for $Re = 100$, 400, 600 and 800. The images reveal that there are weak and fragmented vorticities near spacers at $Re = 100$, as shown in Figure 25a. There is no indication of regular flow structure distributed along the span-wise direction. The vortices dissipate rapidly away from spacers. Counter rotating five pairs of vortices are uniformly spaced in the span-wise direction, as shown in Figure 25a2 and 25b2 at $Re = 400$. Once again, these flow images clearly indicate that coherent three dimensional flow structures exist at this flow rate. The vortices are attached to the spacer and extend into the region between spacers. Flow becomes irregular as Re is increased to 600 and 800. Vortices break and form smaller eddies in the wake of spacers. The vortices extend longer, and they occupy the whole region between the spacers for $Re = 800$, as depicted in Figure 25. These vortices lead to the formation of streaks near the wall, as documented by several investigators [50–52]. The influence of such streaks can be profound on the membrane performance. Concentration polarization and the formation of fouling and scaling will be directly influenced by such flow structures. These effects are presented and discussed in the present study.

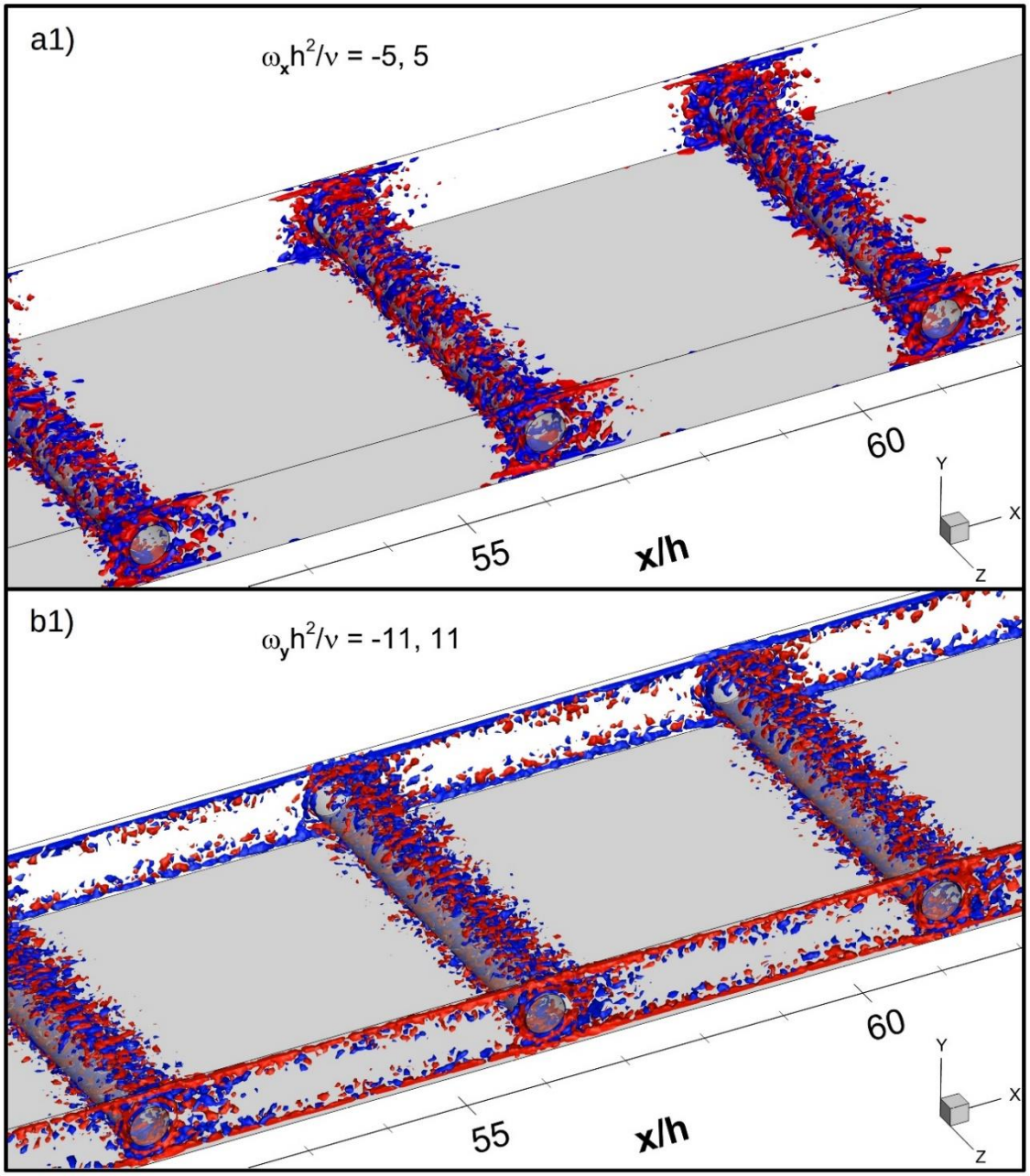

Figure 25: Iso-surfaces of x and y component of the vorticity for different values of the Reynolds number. a) and b) denote iso-surfaces of the x component of the vorticity and y component of the vorticity, respectively. 1, 2, 3 and 4 denote iso-surfaces at Re = 100, 400, 600 and 800, respectively.

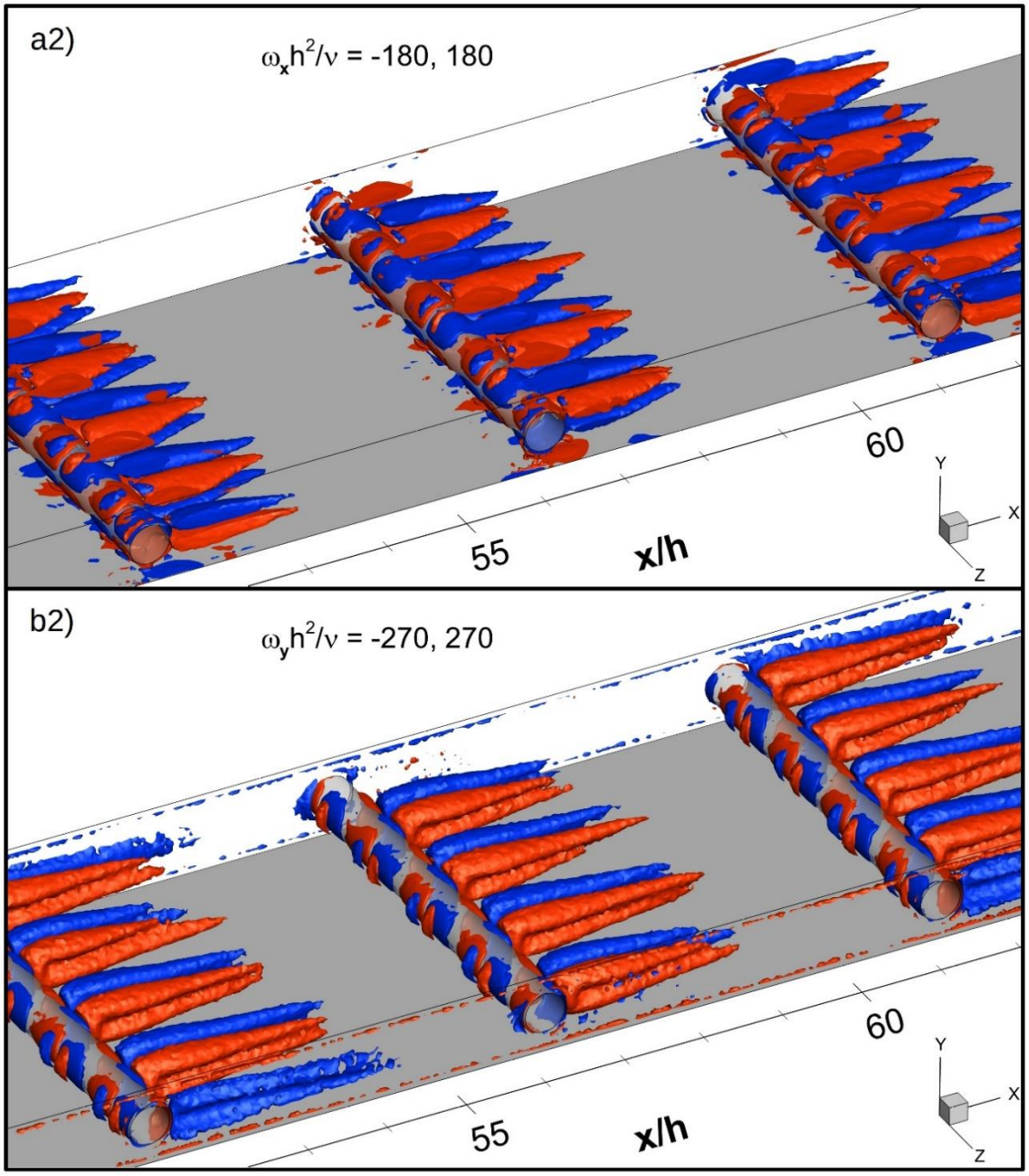

Figure 25: (Continued)

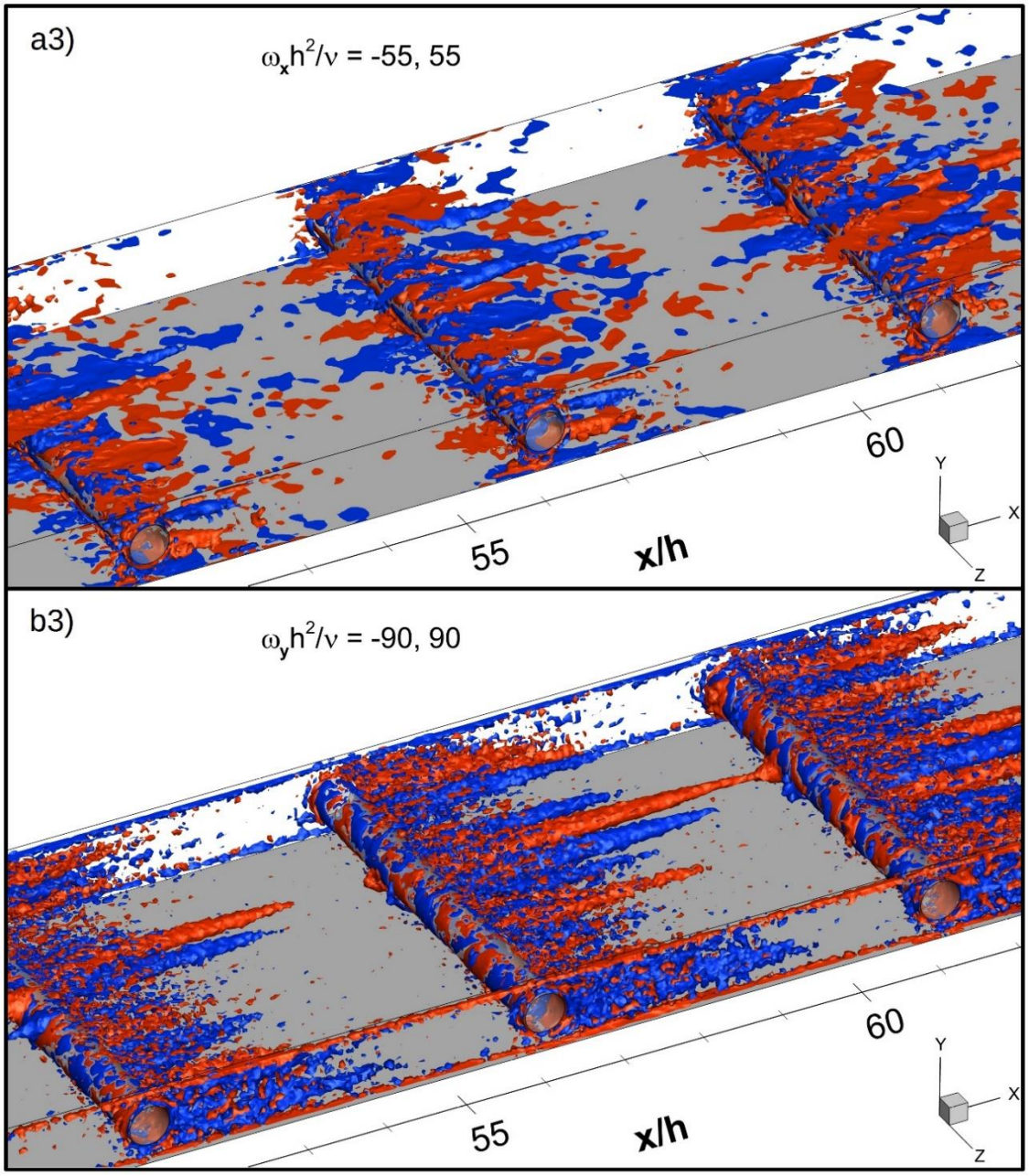

Figure 25: (Continued)

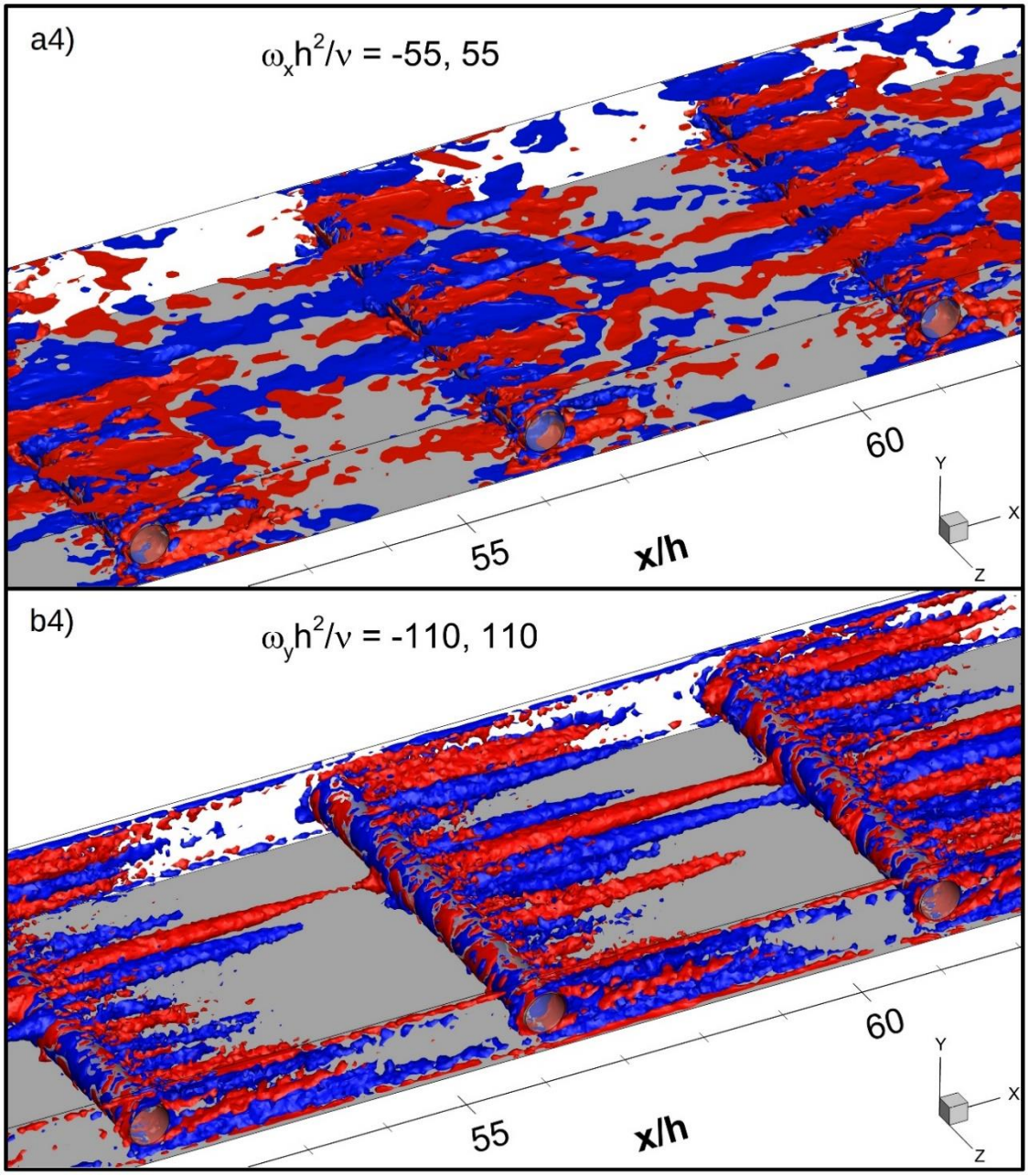

Figure 25: (Continued)

Contours of normalized salt concentration (c/c_0) at three z planes, $z/h = 0.4$, 2 and 3.6, are shown in Figure 26 for $Re = 100$, 400, 600 and 800. There is a thin concentration boundary layer near membrane surface. The thickness of the boundary layer is greater for $Re = 100$ and it decreases as Re is increased. The concentration boundary layer is disrupted by the presence of the spacer. The boundary layer grows away from the spacer. All three planes show similar concentration field at all flow rates. The concentration polarization at $Re = 100$ is the highest while it is the lowest at $Re = 800$, as depicted in Figure 26.

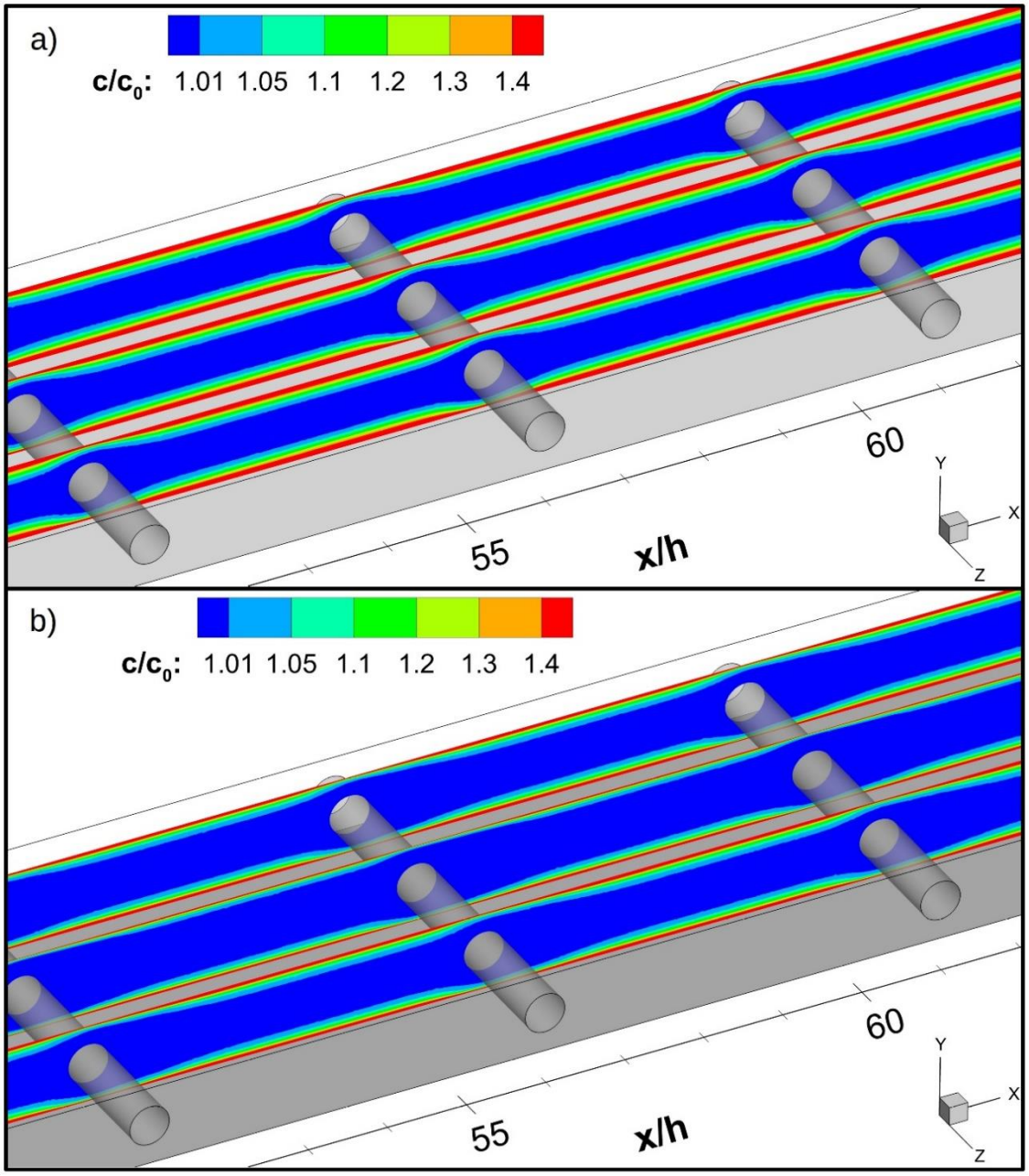

Figure 26: Contours of normalized concentration (c/c_0) acquired at z-planes of $z/h = 0.43$, 2, and 3.6 for values of Re a) 100, b) 400, c) 600 and d) 800.

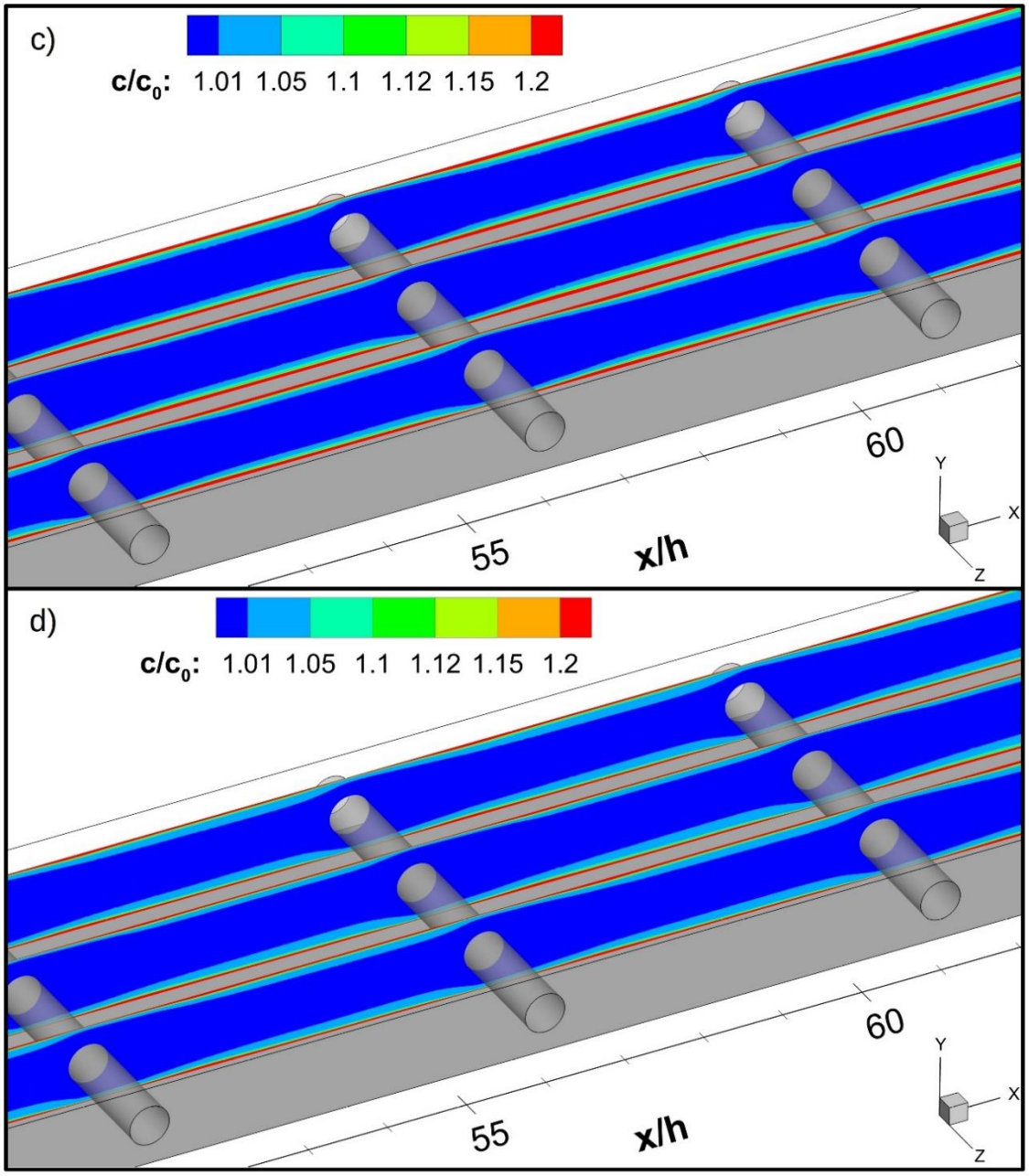

Figure 26: (Continued)

Contours of the water flux through the membrane and the concentration along the surface of the top membrane are shown in Figure 27 for $Re = 100$, 400, 600 and 800. Both water flux and the concentration are uniform in the span-wise direction for $Re = 100$. The water flux through the membrane is profoundly increased by the presence of the spacers, as shown in Figure 27a. The water flux is much higher above each spacer. The concentration along the membrane is much lower right above the spacers, but it increases rapidly away from the spacers. It is also noted that the presence of the spacers alleviate the concentration polarization occurring along the surface of the membrane. At $Re = 400$ the distribution of the water flux and the concentration along the surface of the membrane is strikingly different compared to those at $Re = 100$. The effect of three dimensional flows in the feed channel influences the water flux and the local concentration along the membrane surface. Streaks of high and low regions of water flux and concentration are uniformly distributed in the span-wise direction. Streaks are more pronounced at $Re = 400$ compared to those at $Re = 600$ and 800; following the relative strength of the secondary flows over the primary flows as presented above. The water flux is greater and the concentration overall is lower near spacer at all values of Re. The intensity of the concentration polarization decreases with increasing flow rate. It is important to note that low water flux regions correlates to the high intensity concentration polarization regions at all flow rate considered here. Streaks of high concentration polarization region between spacers coincide with streaks of low water flux regions, as shown in Figure 27. Results of three dimensional simulations confirm conclusion drawn from two dimensional simulations reported earlier [45]. The present

author documented that the spacers enhance the membrane performance while it helps to alleviate concentration polarization in two dimensional flows.

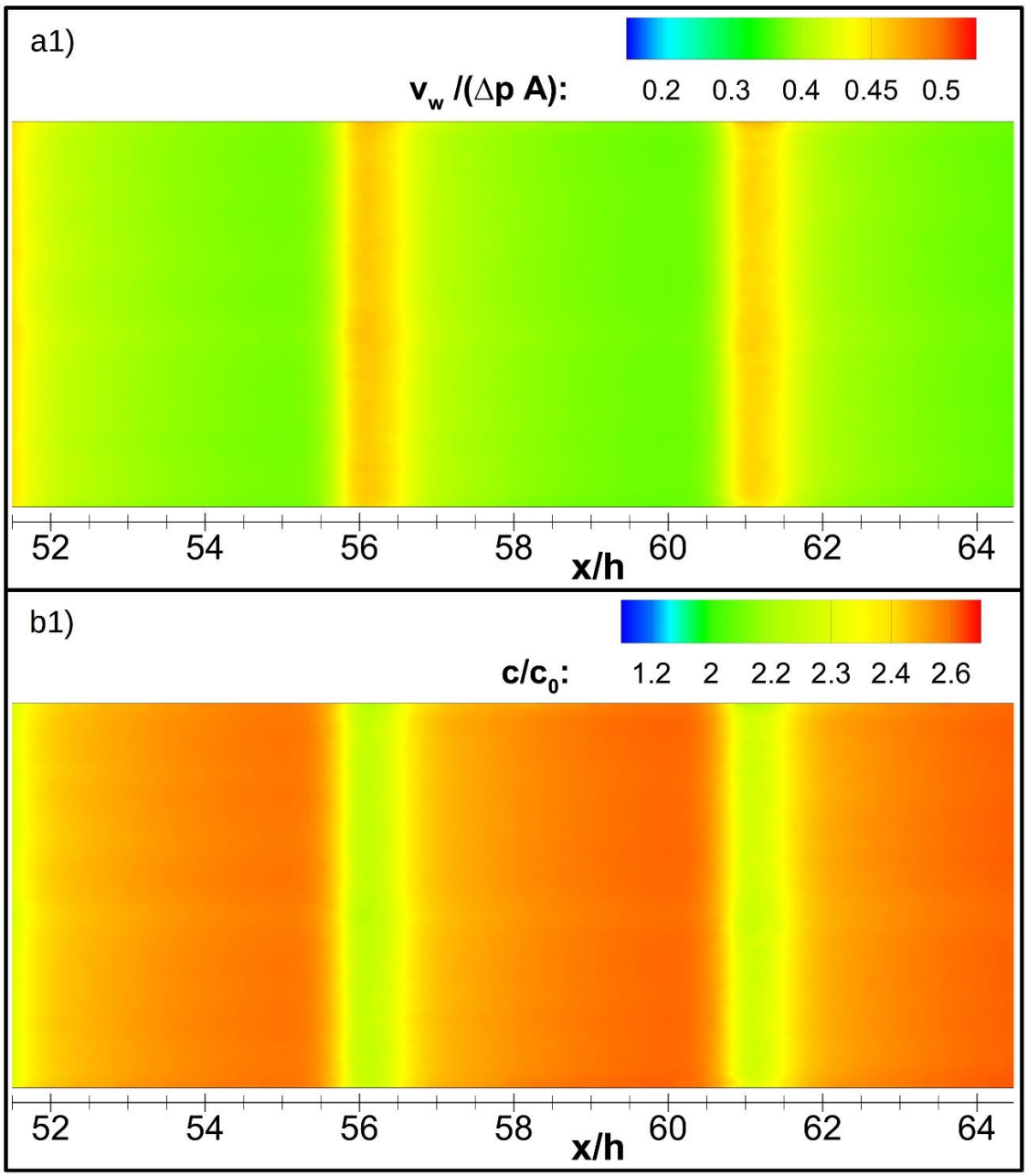

Figure 27: (a) contours of normalized water flux through the top membrane and (b) contours of normalized concentration along the surface of the top membrane for different values of Re. 1, 2, 3 and 4 denote iso-surfaces at Re = 100, 400, 600 and 800, respectively.

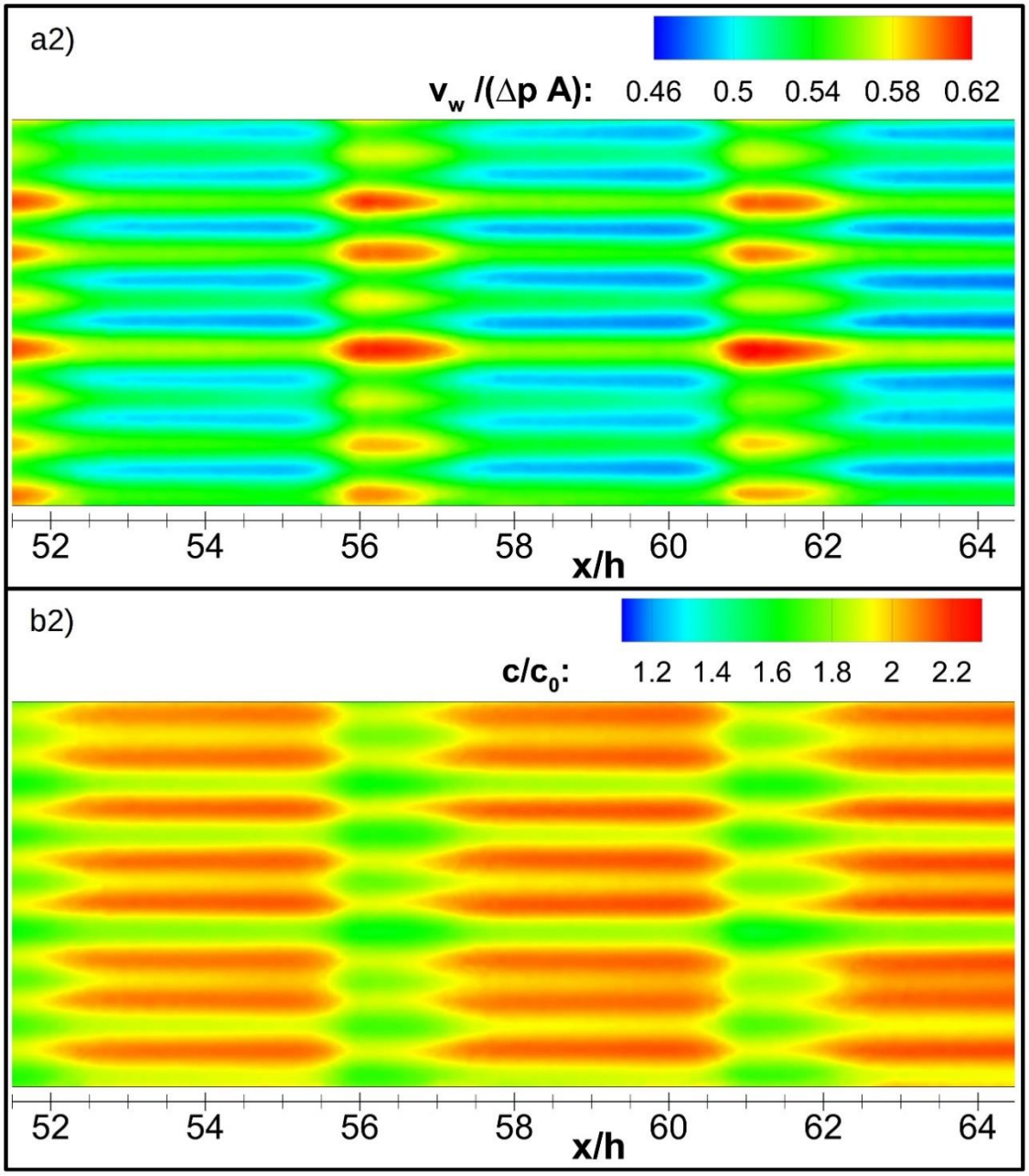

Figure 27: (Continued)

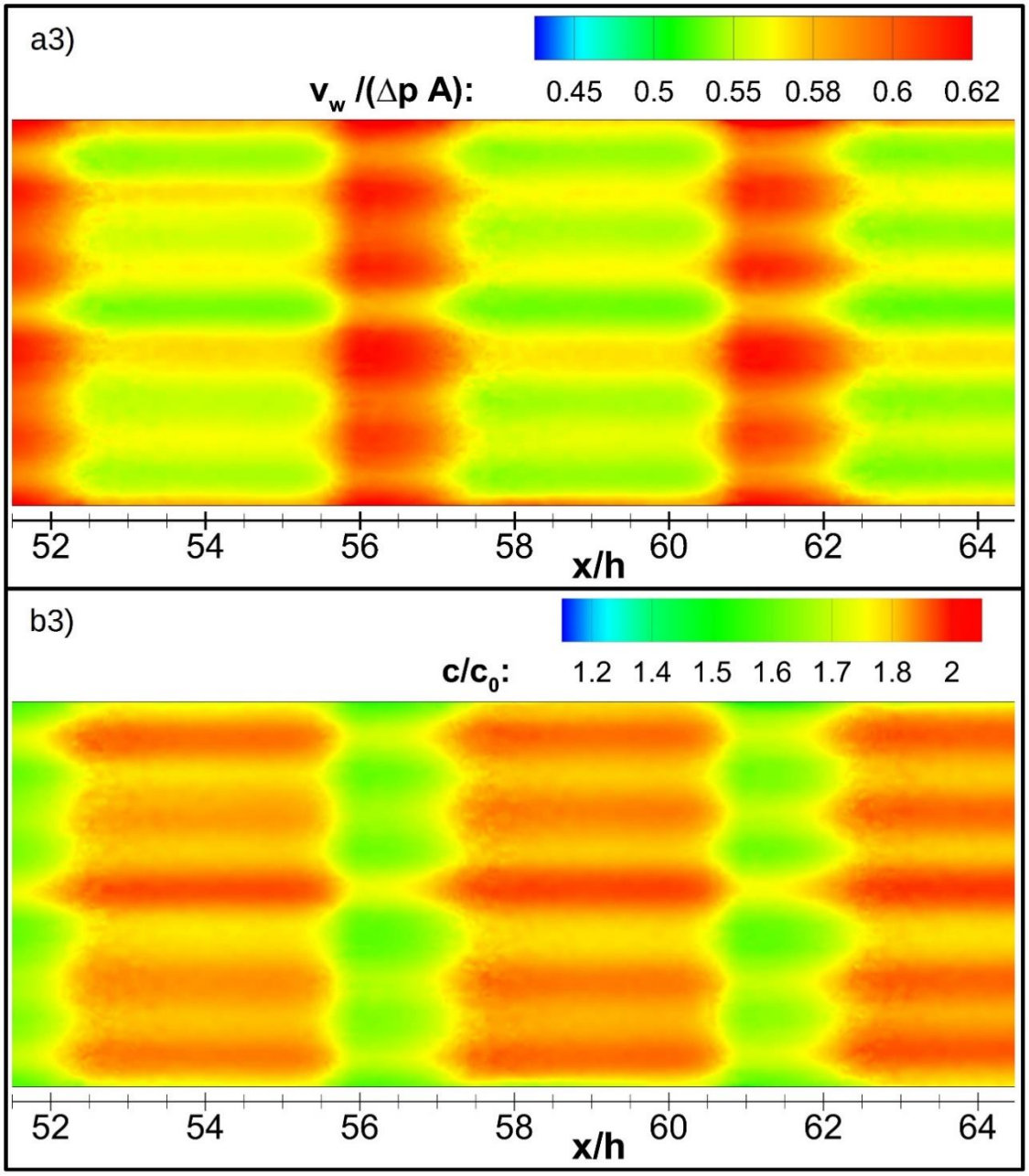

Figure 27: (Continued)

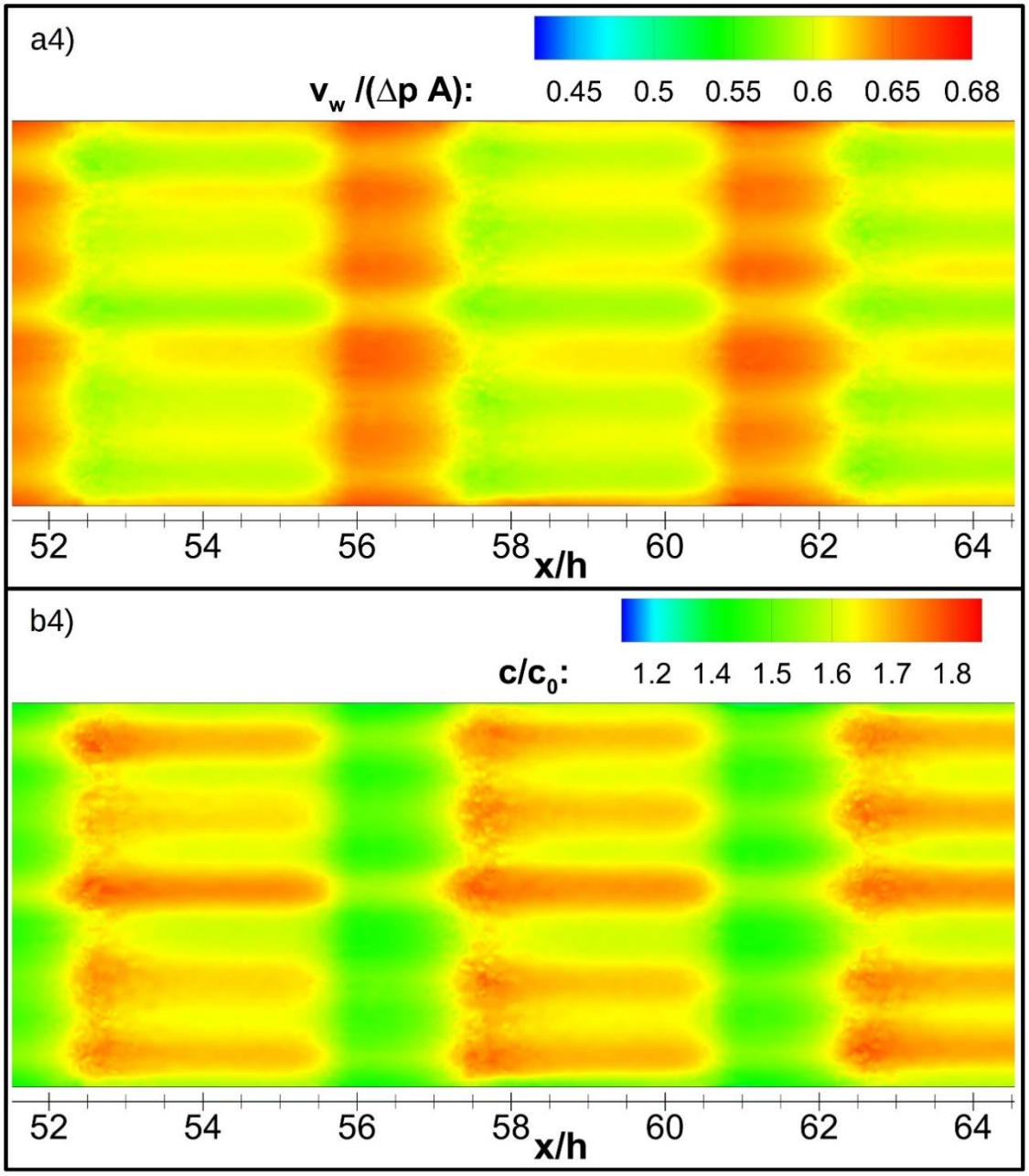

Figure 27: (Continued)

The local value of the Sherwood number is calculated along the surface of membranes from $Sh = (2h)h_m/D$. The bulk concentration, c_b, in equation (18) is calculated from average of salt concentration at the inlet and the outlet. Contours of the local Sh along the surface of the top membrane are depicted in Figure 28. Distribution of Sh is very similar to the distribution of the water flux over the membrane surface. Sh is distributed uniformly in the span-wise direction at $Re = 100$ while strips of high and low regions of Sh are shown at $Re \geq 400$. Similar to the counter part of two dimensional flows presence of the spacers in three dimensional geometry leads to significant increase in Sh. Local value of Sh is much greater near spacer and decreases rapidly away from spacers. The Sherwood number also increases as the flow rate is increased; that is also consistent with the prediction of two dimensional simulations documented in [45]. Streaks of high Sh regions coincide with the regions of low intensity concentration polarization regions, as depicted in Figure 28 and Figure 27.

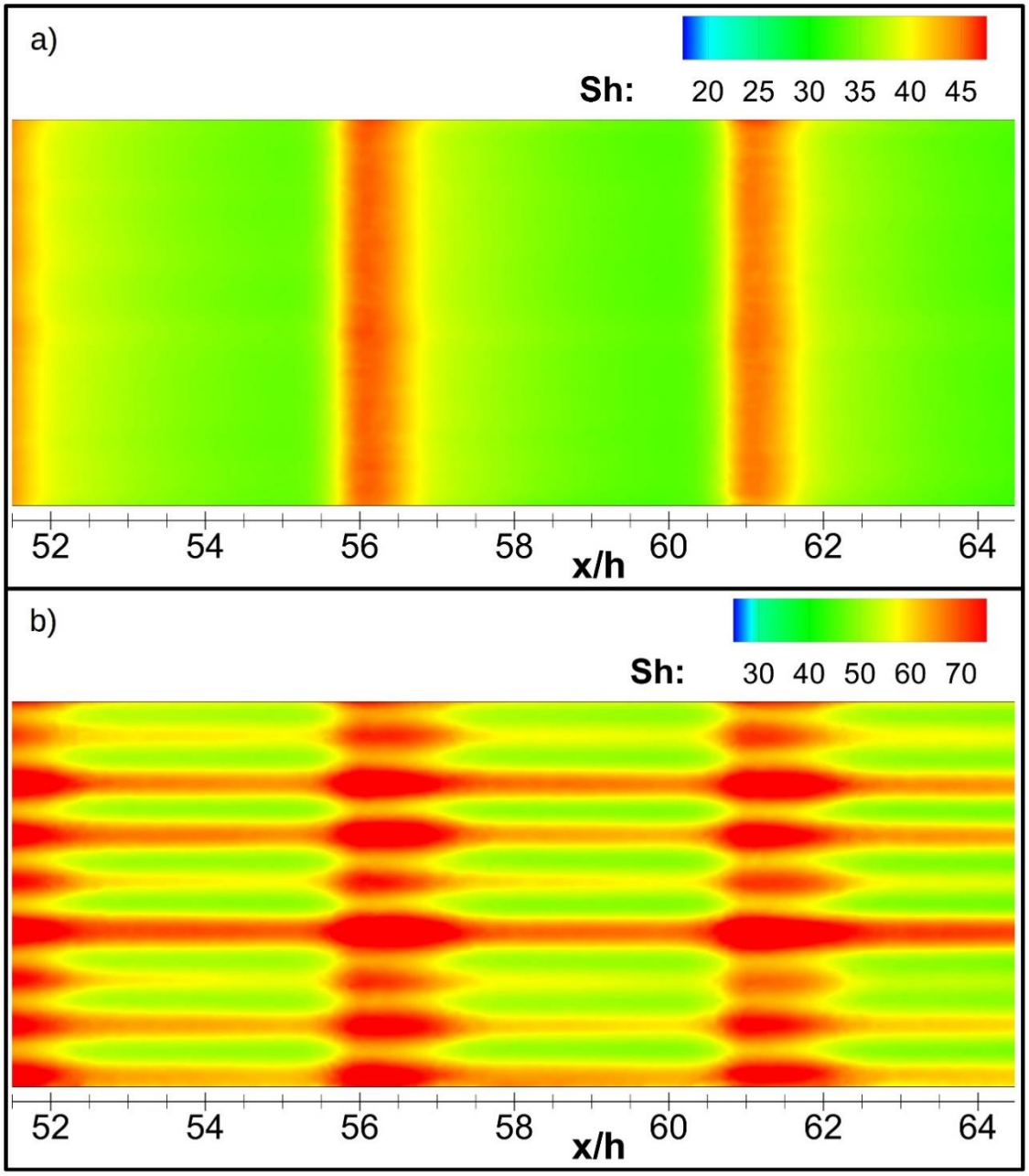

Figure 28: Contours of the local Sherwood number (Sh) along the surface of the top membrane for values of Re a) 100, b) 400, c) 600 and d) 800.

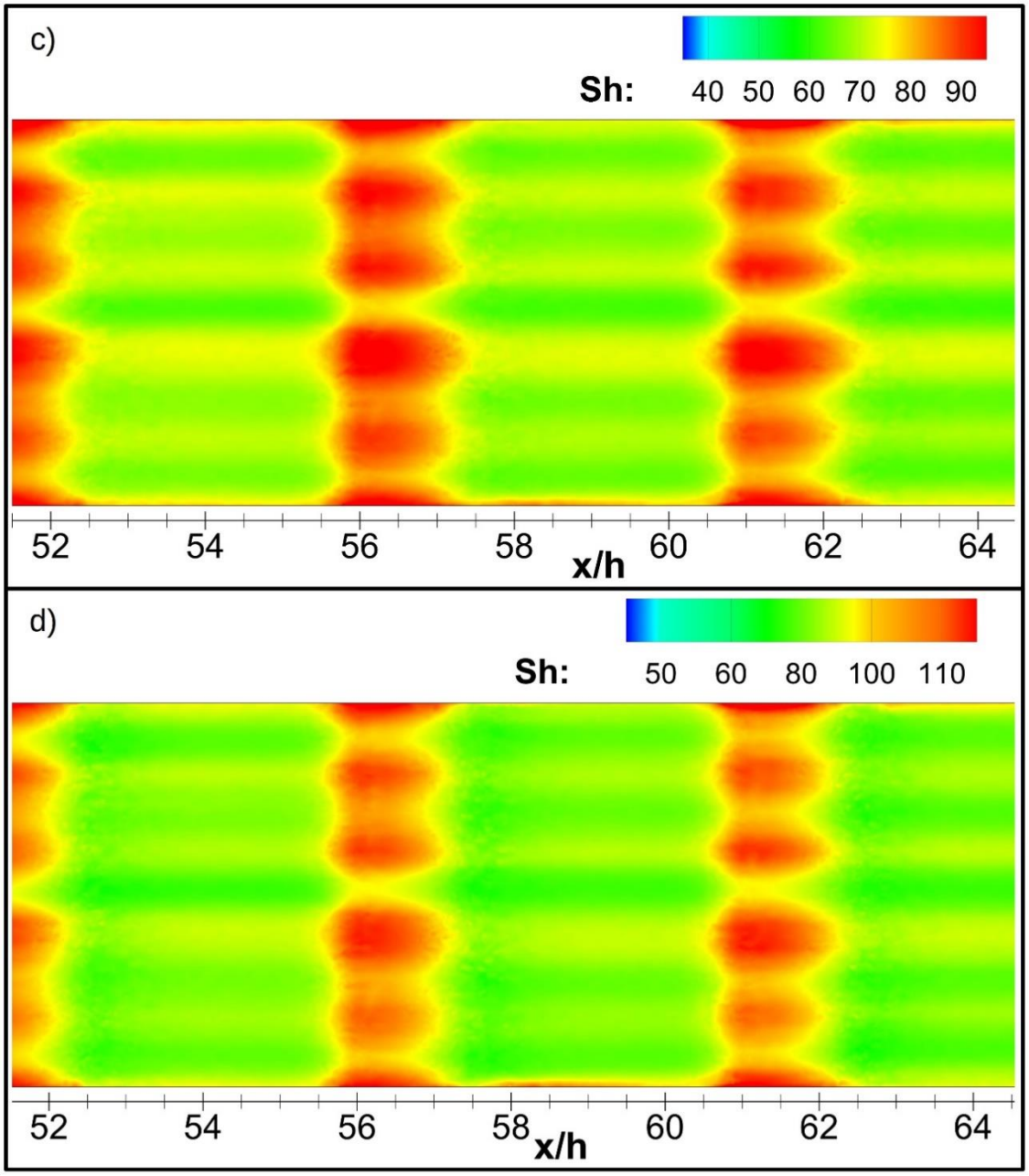

Figure 28: (Continued)

Contours of the normalized wall shear stress along the surface of the top membrane are shown in Figure 29. The local shear stress is normalized by the maximum value of the wall shear stress for each flow rate. The maximum value of the wall shear stress is calculated to be 0.9, 4.5, 8.5 and 12.6 Pa for $Re = 100$, 400, 600 and 800, respectively. Similar to the flow properties presented above the wall shear stress is uniform in the span-wise direction at $Re = 100$, but it becomes streaky as the flow becomes three dimensional at higher flow rates ($Re = 400$, 600 and 800). Streaks induces by the secondary flow is not as pronounced as in the case of the water flux, concentration or Sh number distribution. At all flow rates, the maximum wall shear stress occur right above the spacers where the fluid is accelerated passing through the spacers. The intensity of the wall shear stress increases as Re is increased. Koutsou et al. [53] experimentally determined regions where fouling occurs and showed that the fouling sites coincide with the low wall shear stress regions. Based on present results, potential fouling sites are situated in the regions between spacers and three dimensional flow structures in the feed channel induced by secondary flows help to alleviate potential fouling occurring along the surface of the membrane.

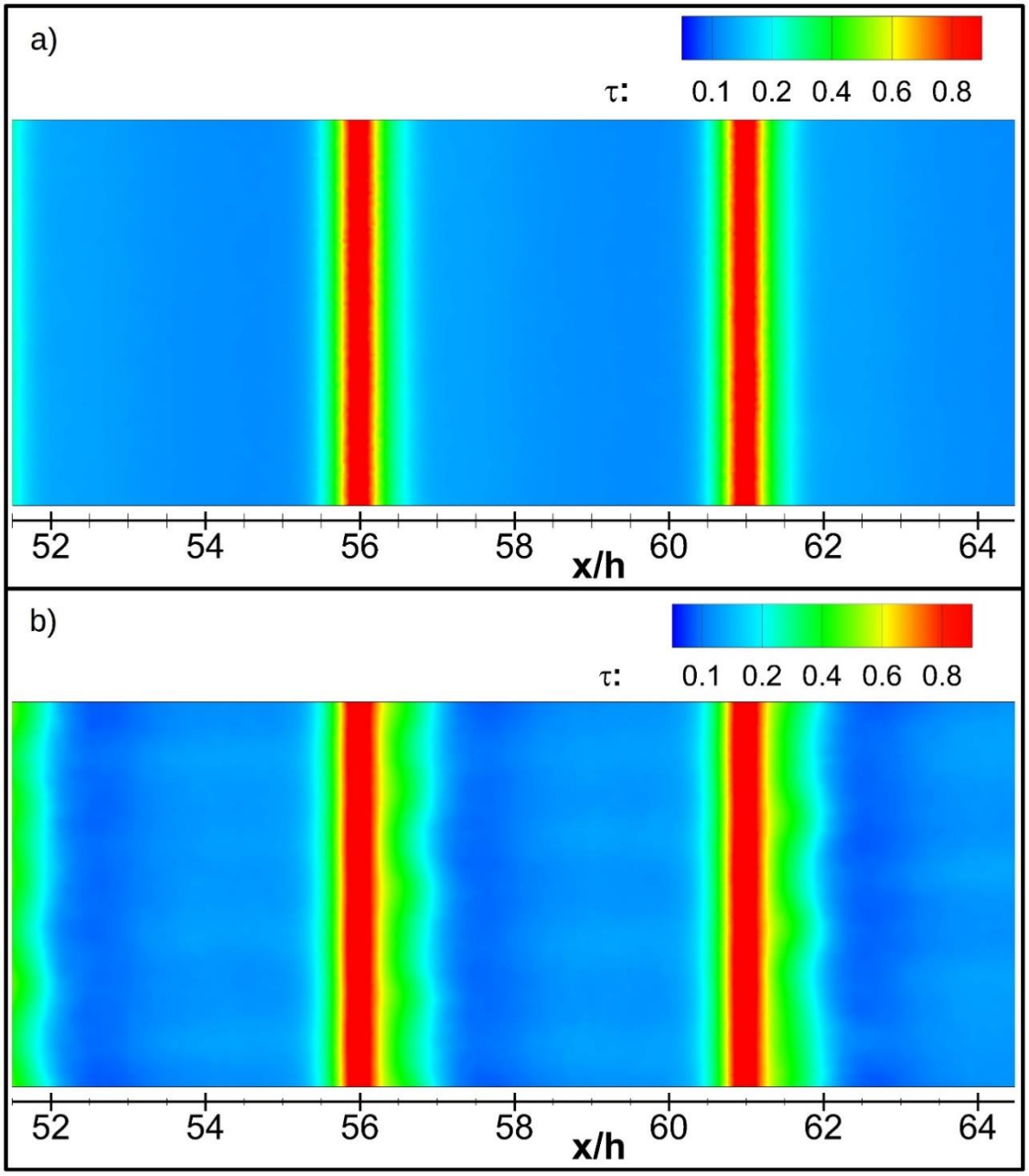

Figure 29: Contours of the wall shear stress normalized by the maximum value for values of Re a) 100, b) 400, c) 600 and d) 800.

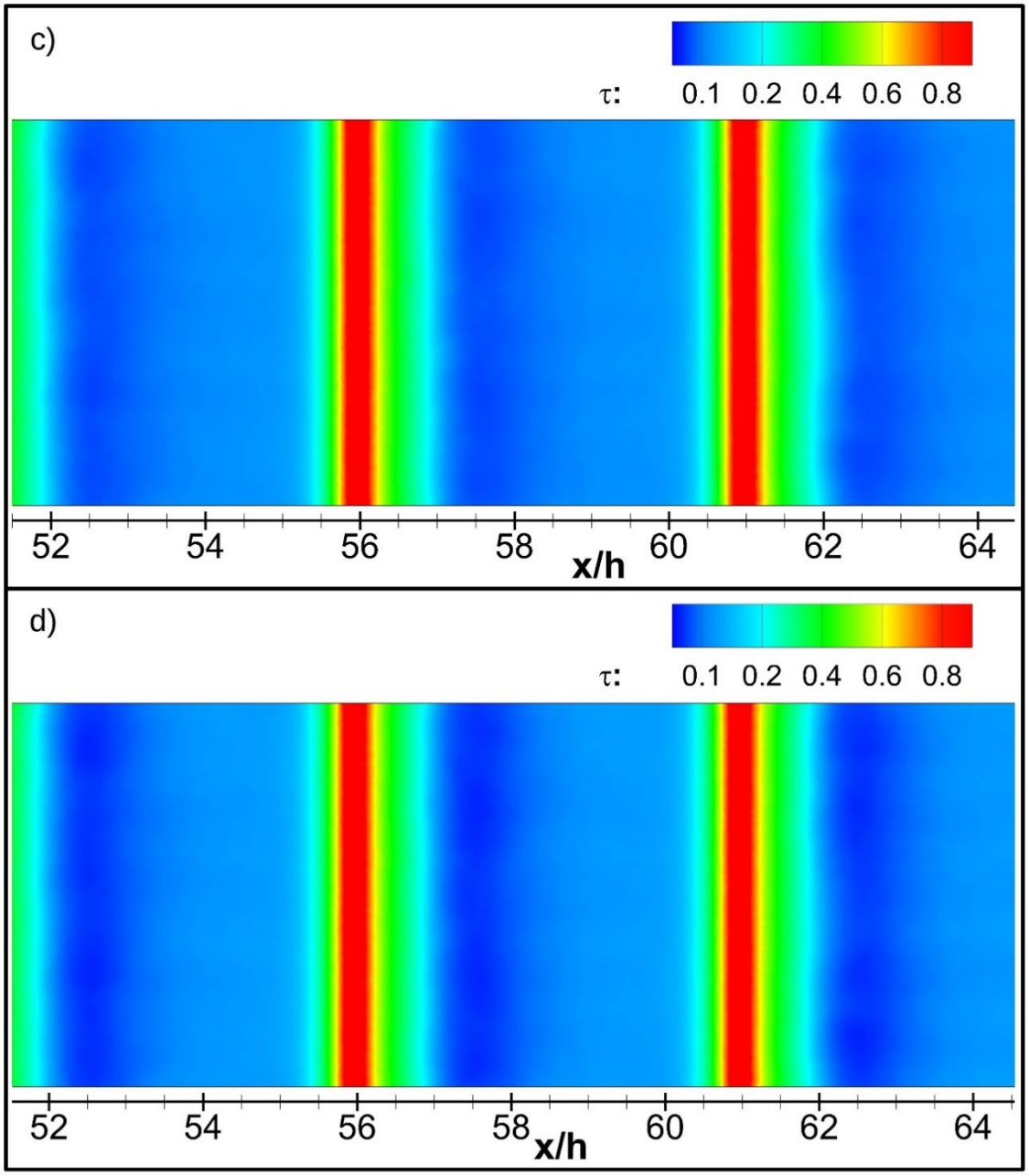

Figure 29: (Continued)

The span-wise averages of normalized water flux, concentration and the Sherwood number at each x location are determined for three dimensional flows in the feed channel containing spacers. These span-wised average profiles in the stream-wise direction are plotted in Figure 30 and 31 in the spacer bank region for different values of Re. The profiles of the normalized water flux, concentration and local value of Sh predicted by two dimensional steady simulations are also plotted in Figure 30 and 31 to assess the influence of the three dimensional effects on the span-wise averaged membrane performance properties for $Re = 100$, 400, 600 and 800. In both figures, the solid lines denote profiles predicted by the three dimensional simulations while the dashed lines denote profiles predicted by two dimensional simulations. Overall distribution of the two dimensional and span-wised average three dimensional profiles is similar for all membrane surface properties. Only the values of the peaks and valleys of these quantities differ at each flow rate, as shown in Figure 30 and 31.

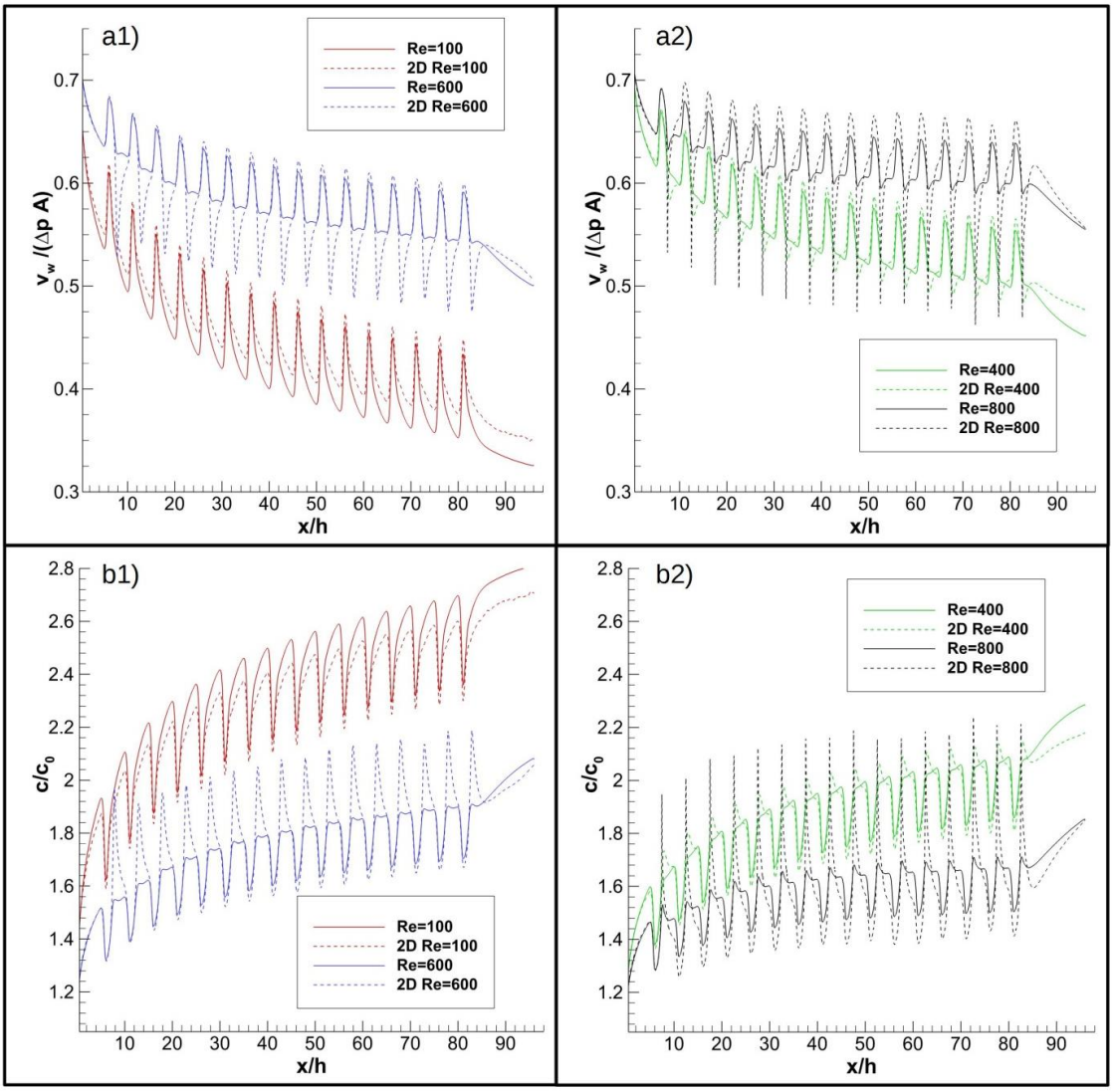

Figure 30: Span-wised averaged water flux profiles (a1 and a2) and the concentration profiles (b1, b2) in the stream-wise direction for different values of Re. Solid lines denote span-wised averaged three dimensional profiles and dashed lines denote two dimensional profiles.

The averaged three dimensional Sh profiles exhibit nearly the same distribution in the stream-wise direction as for the Sh obtained by the two dimensional simulations. Only noticeable difference in Sh profiles is observed near wake regions of the spacers. Sherwood number drops significantly right behind the spacers in the two dimensional geometry and rebound very quickly approaching the following spacers. The values of

Sh is greater at the peak and is lower at the valley of the two dimensional profiles compared those of the span-wise averaged three dimensional profiles, as shown in Figure 31. It has to be noted Sh varies greatly in the span-wise direction at $Re \geq 400$, as shown in Figure 28. Membrane flow properties are influenced by the spatial characteristics of the flow in the feed channel.

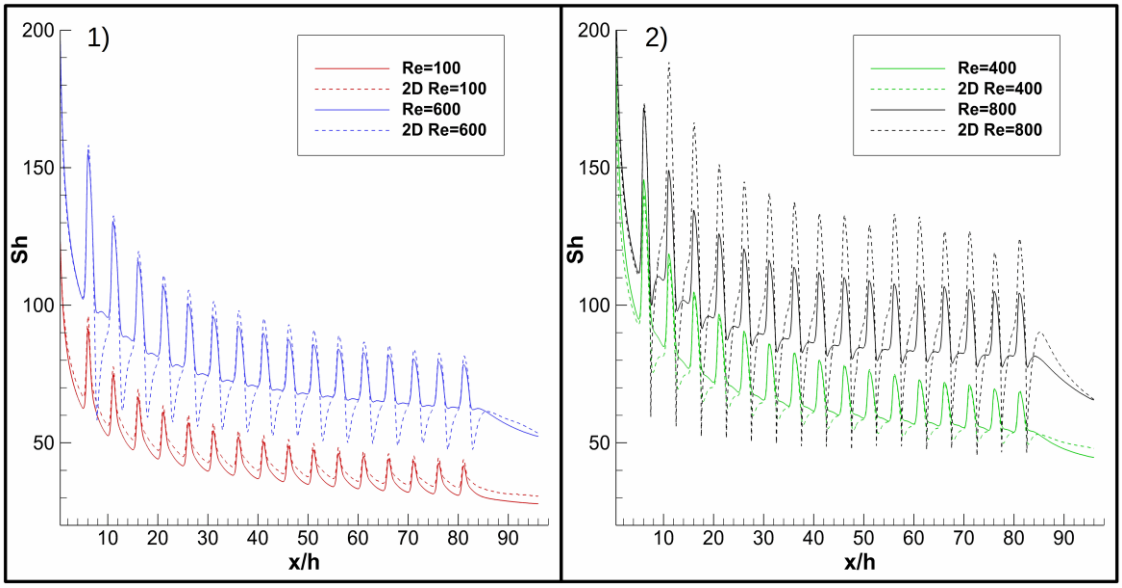

Figure 31: Span-wised averaged Sh profiles) in the stream-wise direction for different values of Re. Solid lines denote span-wised averaged three dimensional profiles and dashed lines denote two dimensional profiles.

The average values of Sh and the normalized water flux in both span-wise and stream-wise direction in the spacer bank region are determined for $Re = 100$, 400, 600 and 800. Spacer bank averaged values of Sh and the water flux are plotted in Figure 32 for three and two dimensional geometry along with the averaged value of Sh and the normalized water flux determined in the three dimensional channel without spacers. Filled blue squares and hollow red circles denote results predicted by the three-dimensional and two-dimensional simulations, respectively. Triangles represent the

results of three-dimensional flow in a channel without spacers. To minimize the influence of the inlet and the outlet conditions averaging is performed in the spacer bank region between $x/h = 38$ and $x/h = 77$. The results reveal that two dimensional approximation predicts the total averages of the water flux and the Sh reasonably well. Slight over-prediction at low Re and high Re by the two dimensional simulations are seen (see Figure 32). It is proven that presence of spacers enhances the membrane performance greatly. Three dimensional effects induced by flow transition do not alter averaged membrane properties significantly. This conclusion is specific to the three dimensional spacer geometry considered in the present study. This geometry is simplified version of the ladder type spacer mesh configuration used in separation modules. The influence of the three dimensional flow structures could be profoundly different for other spacer mesh configurations (woven and non-woven spacers). It is also important to note that transient effects in these flows can also have significant influence on the concentration polarization, fouling and the membrane performance. Investigating the influence of transient effects in three dimensional geometries is worthy of future work, but is not in the scope of the present study.

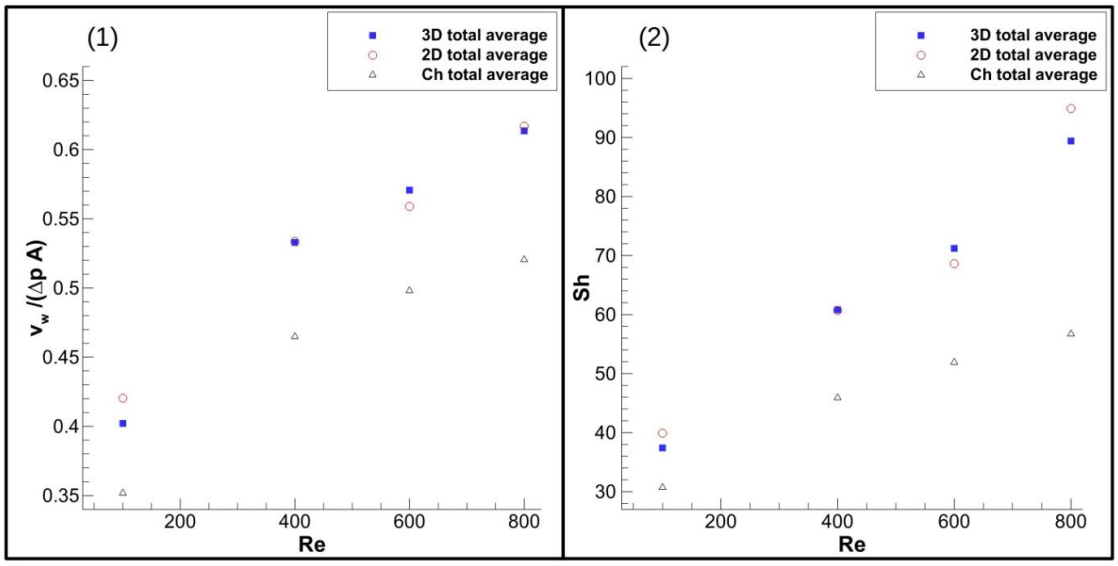

Figure 32: Span-wise and stream-wise averages of normalized water flux (1) and Sh (2) are plotted as a function of Re. Channel averages of membrane properties are shown for three dimensional channel with and without of spacers and two dimensional channel with spacers. The averages of membrane properties are calculated in the spacer bank region between x/h of 38 and 77.

4.3. CONCLUSION

Steady three dimensional simulations have been conducted to study the mass transport through the reverse osmosis membrane in the feed channel of a brackish water desalination module. The membrane surface is treated as a functional surface where the water flux is determined from local salt concentration and local pressure along the membrane. The laminar flow model is employed at $Re = 100$ while the SST k-ω turbulence flow model is employed to simulate mass and momentum transport in the feed channel at $Re \geq 400$. The flow and concentration field is nearly uniform at $Re = 100$, but it becomes strongly three dimensional for $Re \geq 400$. It is shown here that flow transition from two dimensional to three dimensional flows in a channel containing spacers occur for values of Re between 100 and 400. This is consistent with results documented previously for flows past arrays of cylinders with blockage ratio of 1/2.

Even though two dimensional flow simulations predicts the averaged membrane properties reasonably well, the local water flux and Sh along the surface of the membrane varies strongly in the span-wise direction. Furthermore the concentration polarization is profoundly influenced by the three dimensional secondary flows induced by the flow transitions. Velocity and vorticity field indicate spatially periodic flow structures present in the feed channel. Streaks along the surface of the membrane for local properties such as Sh, concentration, water flux and wall shear stress are results from the vortical structures obtained in these three dimensional flows. High water flux regions and low concentration regions coincide with the low wall shear regions. The high intensity concentration polarization sites correlates directly with the high potential fouling sites. Spacers enhance the membrane performance, and it mitigates the concentration polarization. Increasing flow rate also enhance the membrane performance. This study proves that three dimensional effects have profound influence on the membrane performance, especially the polarization and fouling characteristics of the reverse osmosis membrane in desalination systems. Further study is needed to characterize flows in the feed channel with various mesh configurations of spacers used in the desalination processes.

CHAPTER 5: THREE DIMENSIONAL ANALYSES – NET-TYPE SPACERS

5.1. GEOMETRY AND MESH STUDY

The top view of the computational domain is illustrated in Figure 33. The top and the bottom surfaces represent the reverse osmosis membranes. The gap between the membranes is $h = 1.5$ mm. Eleven repeated cells are placed along the stream-wise direction in the mid-plane of the feed channel to form a mesh of spacers. The spacer strands diameter (d) is fixed at $1/2\,h$, and the distance between two successive intersections of strands in the stream-wise direction is also fixed at $6.7\,h$, as depicted in Figure 33. The angle between the strands and the stream-wise direction, θ, is varied — $30°, 45°$ and $60°$ — to create different geometries of spacers. The cells are symmetrically placed at the mid-plane with their centers along the stream-wise direction, as illustrated in Figure 33. The length of the inlet and the outlet region is $5\,h$ and $17.67\,h$, respectively, in order to minimize the effects of the imposed boundary conditions on the velocity and the concentration fields in the desalination module containing spacers. Reynolds number (Re) is defined as $Re = (2h\,U_{ave})/\nu$. Simulations are conducted for values of Re 100, 400 and 800 for each geometry. Here U_{ave} is the average velocity at the inlet, and ν is the kinematic viscosity ($\nu = \mu/\rho$) of the binary solution of salt and water.

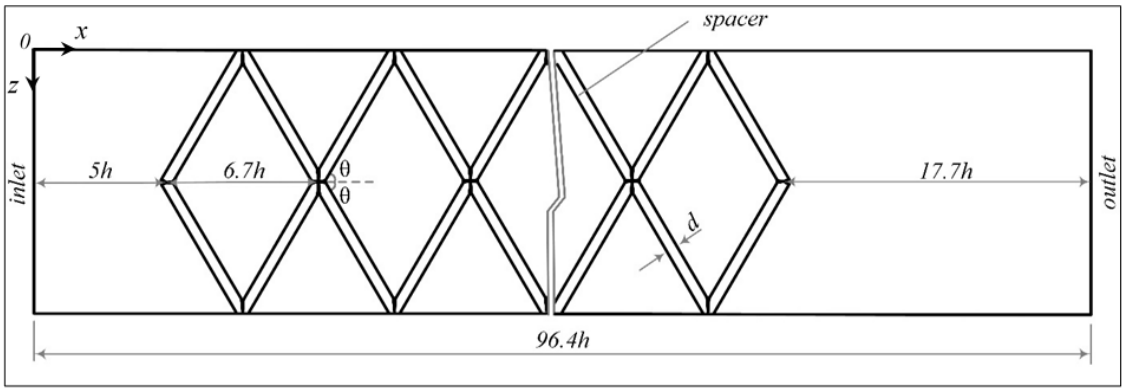

Figure 33: Schematic of the computational domain. Top view of the feed channel.

The mesh elements near walls is shown in Figure 34. The mesh study is performed for the channel containing the net of spacers in the 60° arrangement. The spatial convergence test employs three mesh sizes: 32 million elements (M1), 48 million elements (M2) and 60 million elements (M3). For three meshes, the profiles of normalized stream-wise velocity component (u/U_{ave}) as a function of the cross-flow direction at $x/h = 8.3$ and $z/h = 3.9$ are shown in Figure 35a. Figure 35b and 35c show profiles of the normalized water flux ($v_w/(A\Delta P)$) and the normalized concentration (c/c_0) along the surface of the top membrane in the span-wise direction, z. Concentration and water flux profiles are obtained at $x/h = 8.3$. Velocity, concentration and water flux profiles acquired using M2 and M3 meshes differ only slightly (see Figure 35a-35c). This ensures that the spatial convergence is attained with 48 million elements mesh. Results of simulations presented in the current study are obtained by employing M2 mesh. Although, a better spatial resolution can be achieved by refining mesh further, limited computational resources would make the task to be challenging.

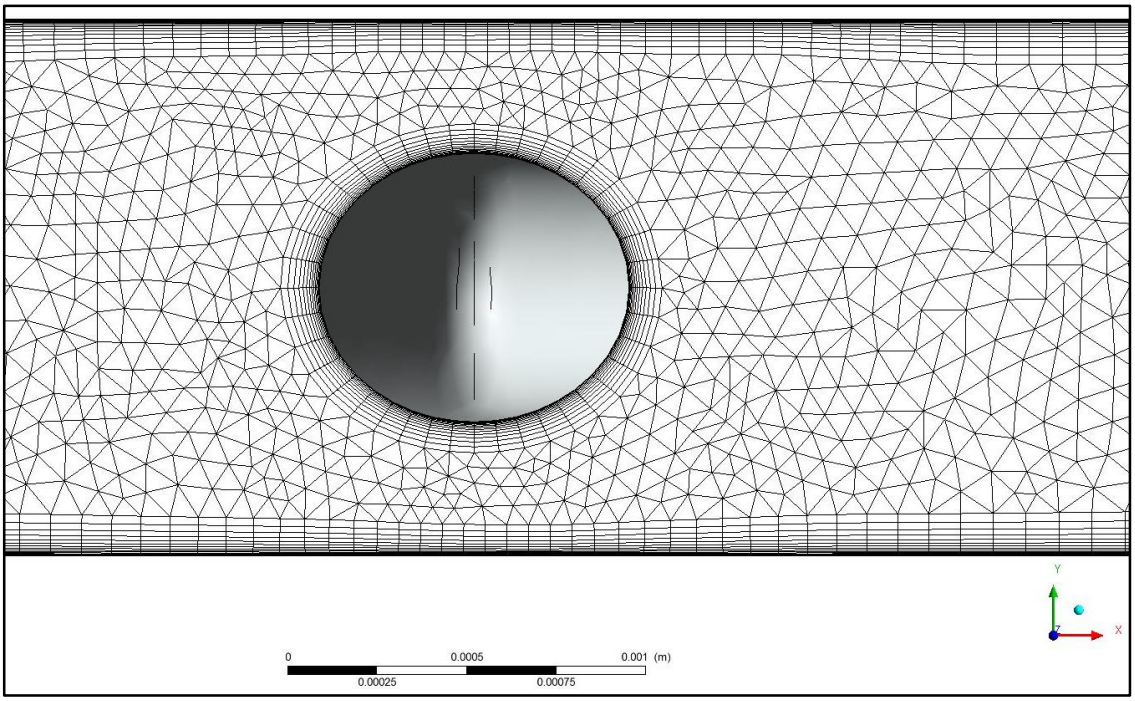

Figure 34: Mesh elements size near spacer and membrane.

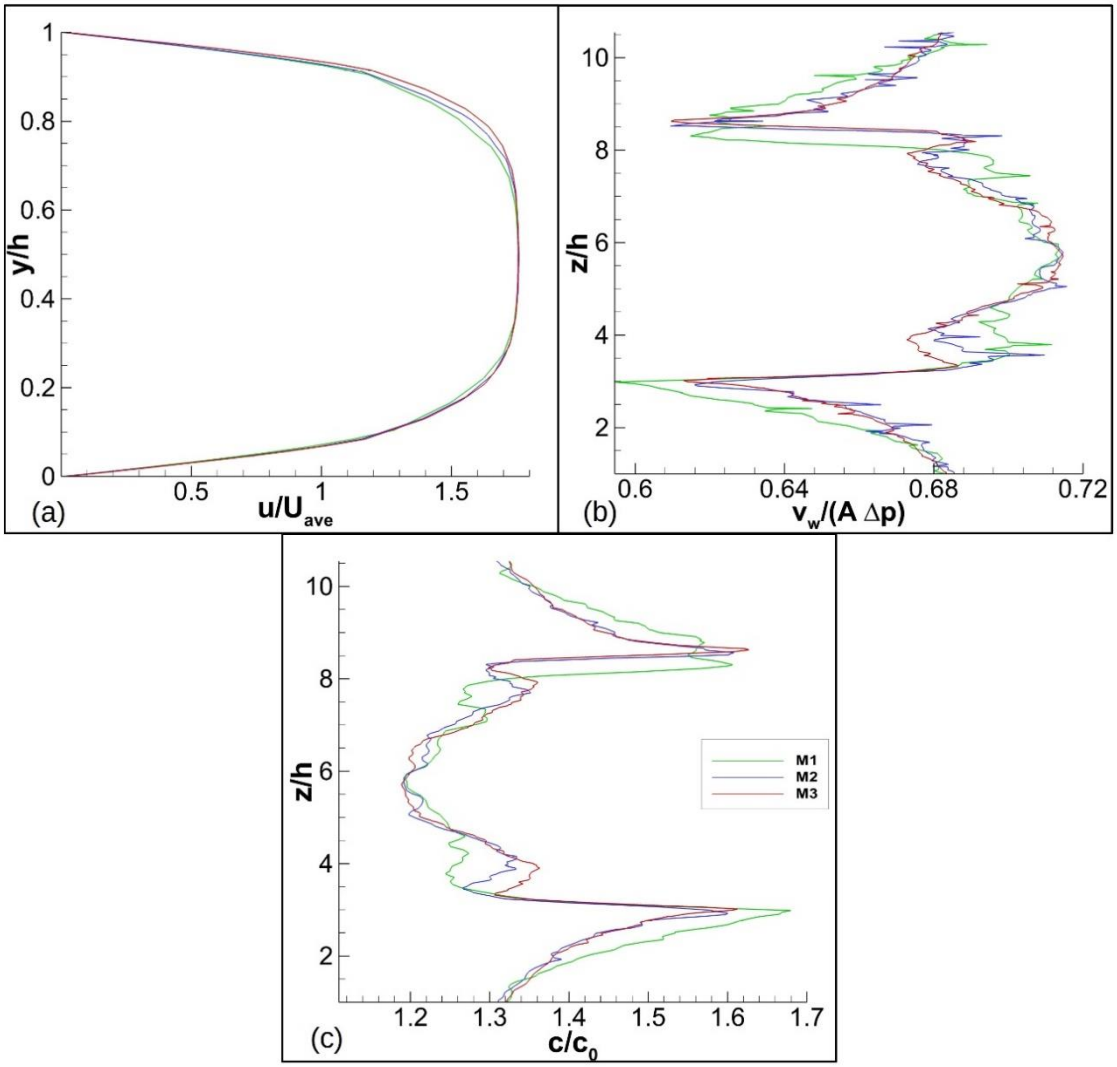

Figure 35: (a) Profiles of stream-wise component of the velocity obtained at $x/h = 8.3$ and $z/h = 3.9$, (b) profiles of the normalized water flux through the top membrane obtained at $x/h = 8.3$, and (c) profiles of the normalized concentration obtained at $x/h = 8.3$ along the surface of the top membrane.

5.2. RESULTS

5.2.1. 30° GEOMETRY:

The iso-surfaces of the stream-wise component of the velocity are shown in Figure 36a. Along the iso-surfaces $u/U_{ave} = 1.5$, the region inside the iso-surfaces u/U_{ave} is greater than 1.5, and the region outside the surfaces u/U_{ave} is lower than 1.5.

Iso-surfaces of the normalized y-component of the vorticity are illustrated in Figure 36b. Images in Figure 36, labeled as 1, 2 and 3, denote iso-surfaces acquired at Re of 100, 400 and 800, respectively. High speed flow is obtained in the middle region of the cell, as illustrated in Figure 36a1 for $Re = 100$. Fluid speed is much higher near the forward stagnation region of the intersection between strands while the backward stagnation region experiences low speed wake flows. Fluid speed becomes much greater in the region between spacers and membranes as Re is increased. High speed flow region in the middle of the cell shrinks, and it extends from the backward stagnation area to the forward stagnation area, as shown in Figure 36a2 for $Re = 400$. The high speed region inside the cell shrinks further while the high speed region between the strands and the membranes grows as Re is increased to 800, as depicted in Figure 36a3. Low level of vorticity is obtained inside the cell at $Re = 100$, as indicated in Figure 36b1. Uniform distribution of the vorticity is confined to the boundary layers of the strand. This implies that low level of mixing is present inside the cell at low flow rates. The vortices spread to the region inside the cell by extending from the rear stagnation region to the middle region of the cells, as shown in Figure 36b2 for $Re = 400$. The region where high level of vortical activities grows, and the magnitude of the vorticity increases as Re is raised to 800. This is an indication that mixing is strongly enhanced inside the cells as the flow rate is increased. It is anticipated that the presence of the spacers in the feed channel influences the membrane performance and the concentration polarization.

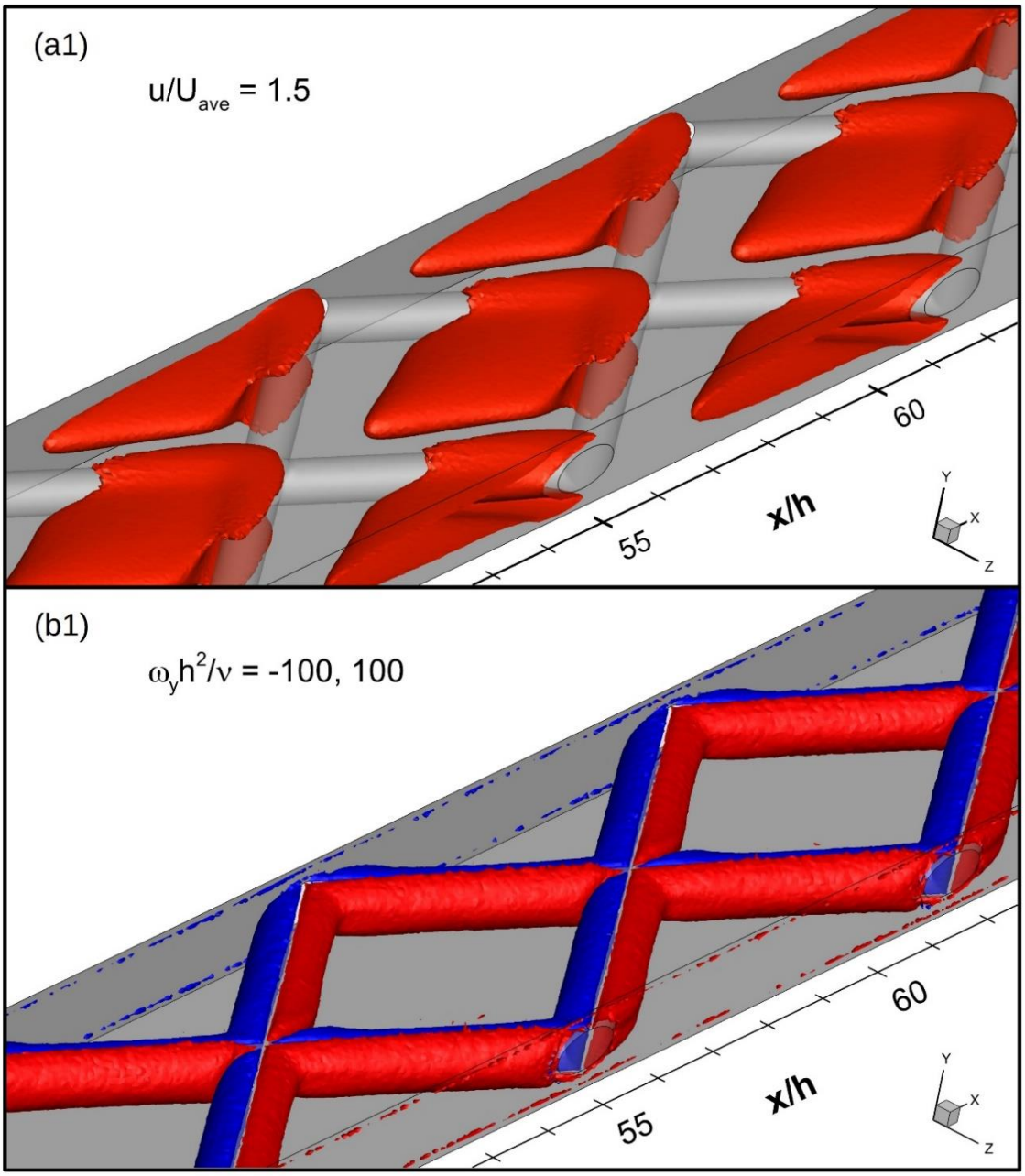

Figure 36: Iso-surfaces of (a) normalized the stream-wise component of the velocity and (b) normalized y-component of the vorticity. 1, 2 and 3 denote iso-surfaces at Re = 100, 400 and 800, respectively. The images are acquired in a feed channel containing mesh of spacers with an angle of 30 ^{0}.

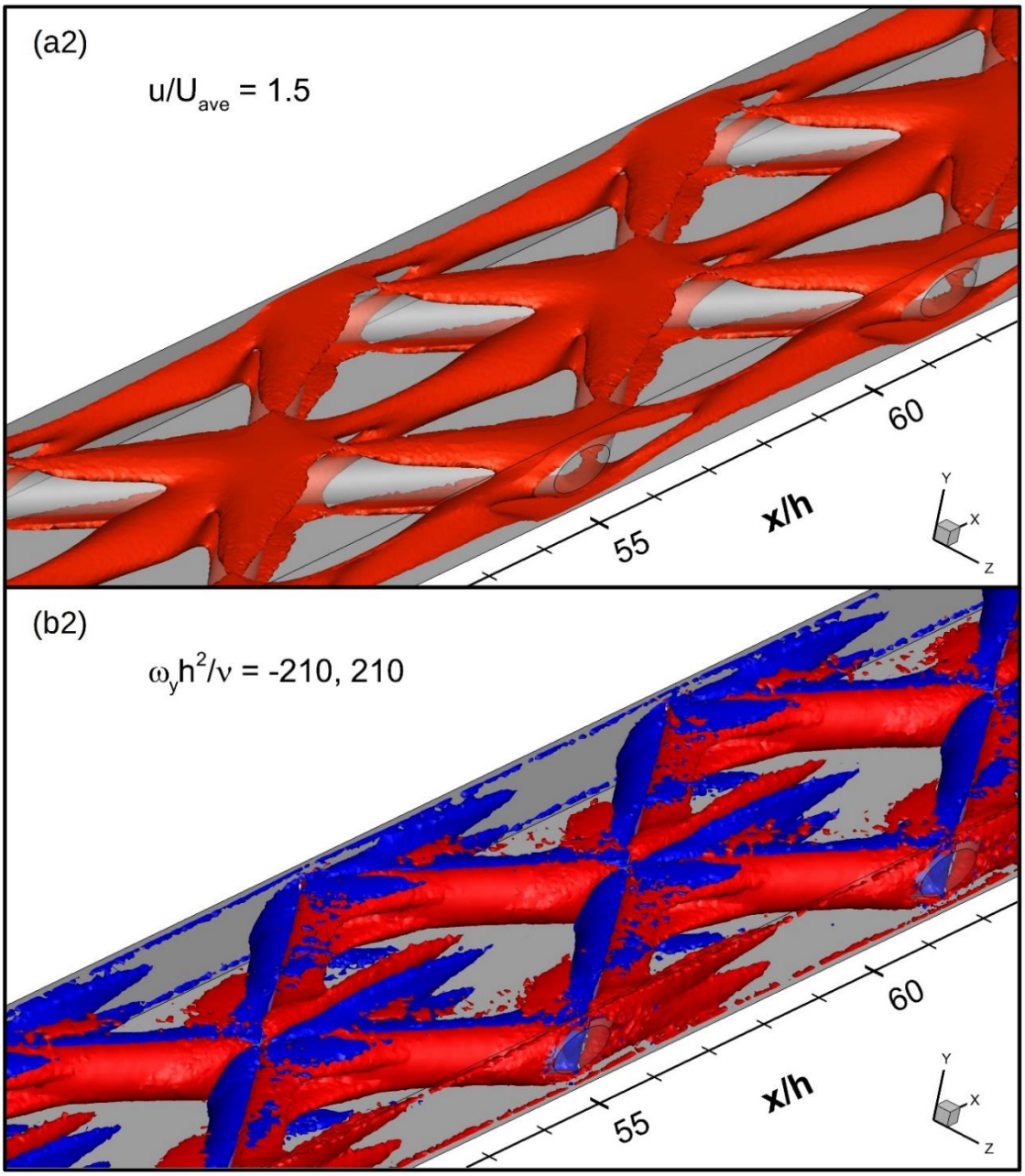

Figure 36: (Continued)

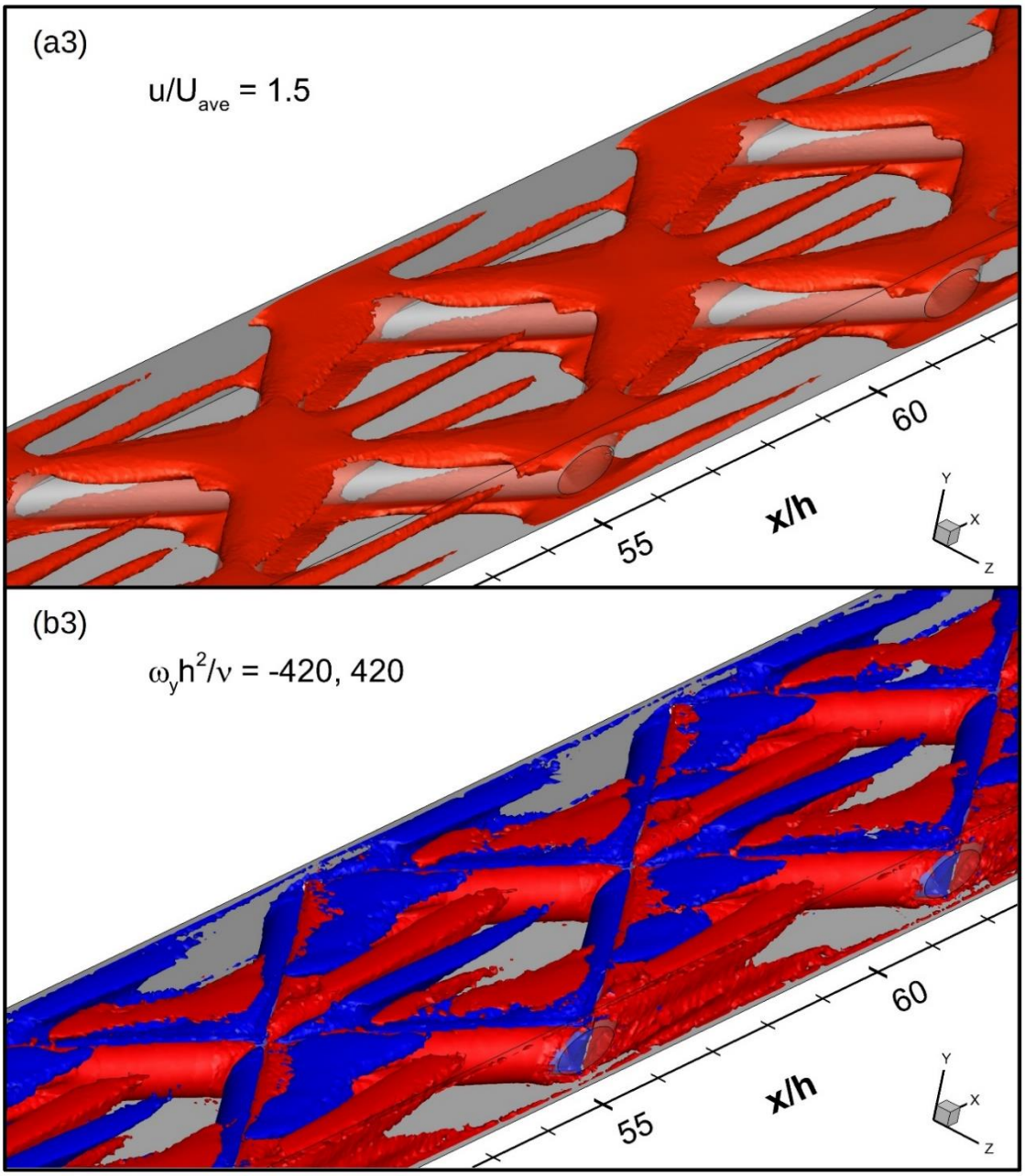

Figure 36: (Continued)

Contours of the normalized local concentration (c/c_0) and the normalized local water flux ($v_w/(\Delta p\ A)$) along the surface of the top membrane are shown in Figure 37 for Re of 100, 400 and 800. (a) and (b) images denote concentration contours and water flux contours, respectively. Images labelled by 1, 2 and 3 denote contours at Re of 100, 400 and 800. Concentration polarization occurs in a repeated pattern along the stream-wise direction. For each flow rate, it occurs in the regions away from the intersection of strands. The concentration polarization region follows similar patterns at all flow rates with a slim alterations at $Re = 800$. The level of concentration polarization is the highest at $Re = 100$, and it decreases significantly as Re is increased to 800, as shown in Figure 37a. The presence of spacers in the feed channel reduces the magnitude of concentration polarization significantly at all flow rates. Mitigation of concentration polarization is much greater at higher flow rates. This is directly attributed to the mixing in the feed channel induced by spacers. The vorticity field clearly indicates that mixing in the feed channel is much greater at higher flow rates. More than 40% reduction in the maximum concentration along the surface of the membrane is obtained as Re is increased from 100 to 800. The water flux distributions along the surface of membrane follow very similar characteristics as the concentration distributions. The lowest rate of water passage through the membrane is obtained in regions where concentration polarization occurs, as shown in Figure 37b. The water flux increases significantly as the flow rate is increased. The membrane module performs much more efficiently at higher flow rate. It is important to note that the pressure drop can significantly be higher at higher flow rates. In order to access the

membrane performance properly the coefficient of performance including the influence of pressure drop should be calculated and compared for different configurations at different operating conditions.

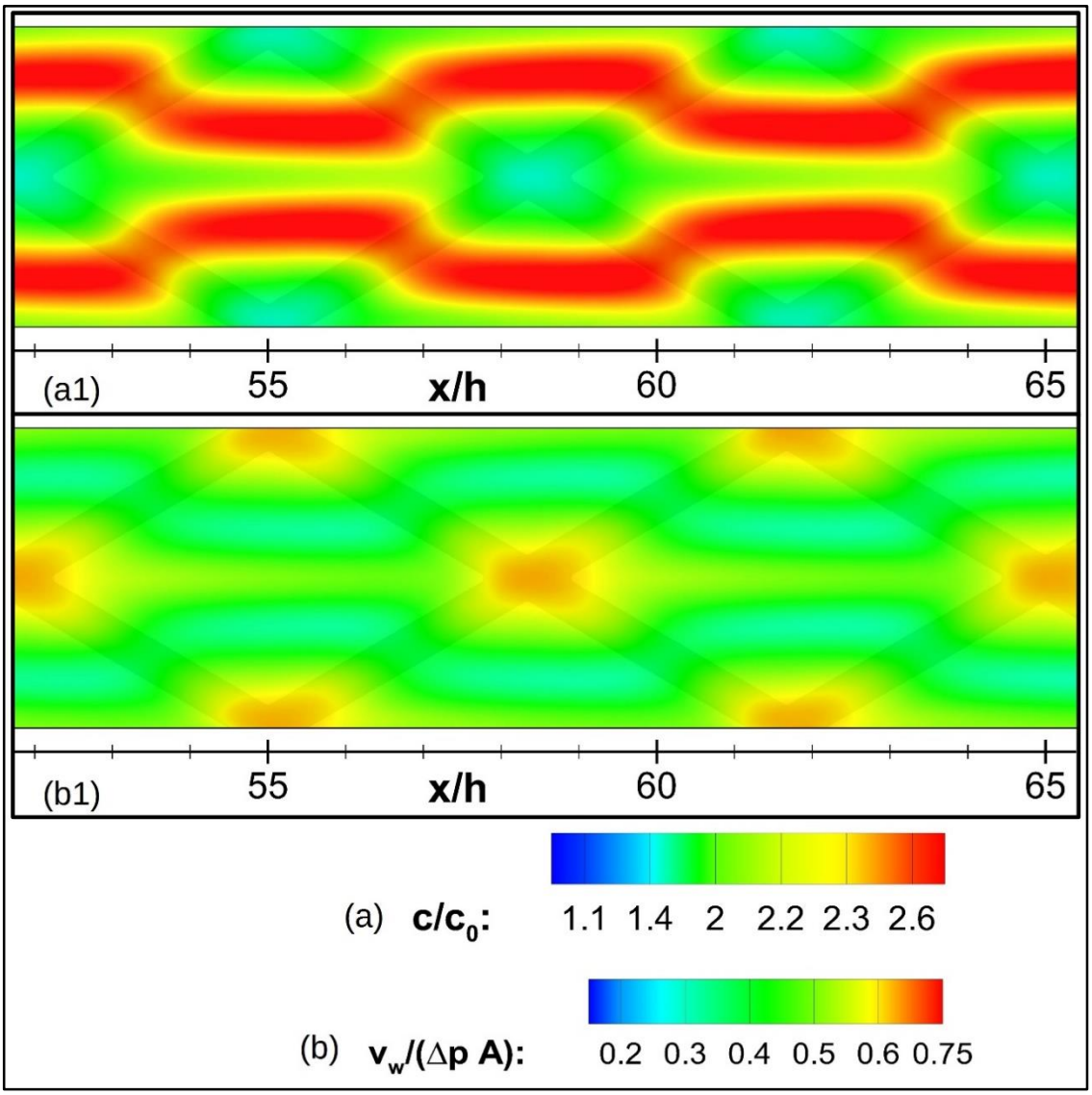

Figure 37: (a) Contours of normalized concentration along the surface of the top membrane and (b) contours of the normalized water flux through the top membrane. 1, 2 and 3 denote contours at Re = 100, 400 and 800, respectively. The contours are determined in a feed channel containing mesh of spacers with an angle of 30 ^{0}.

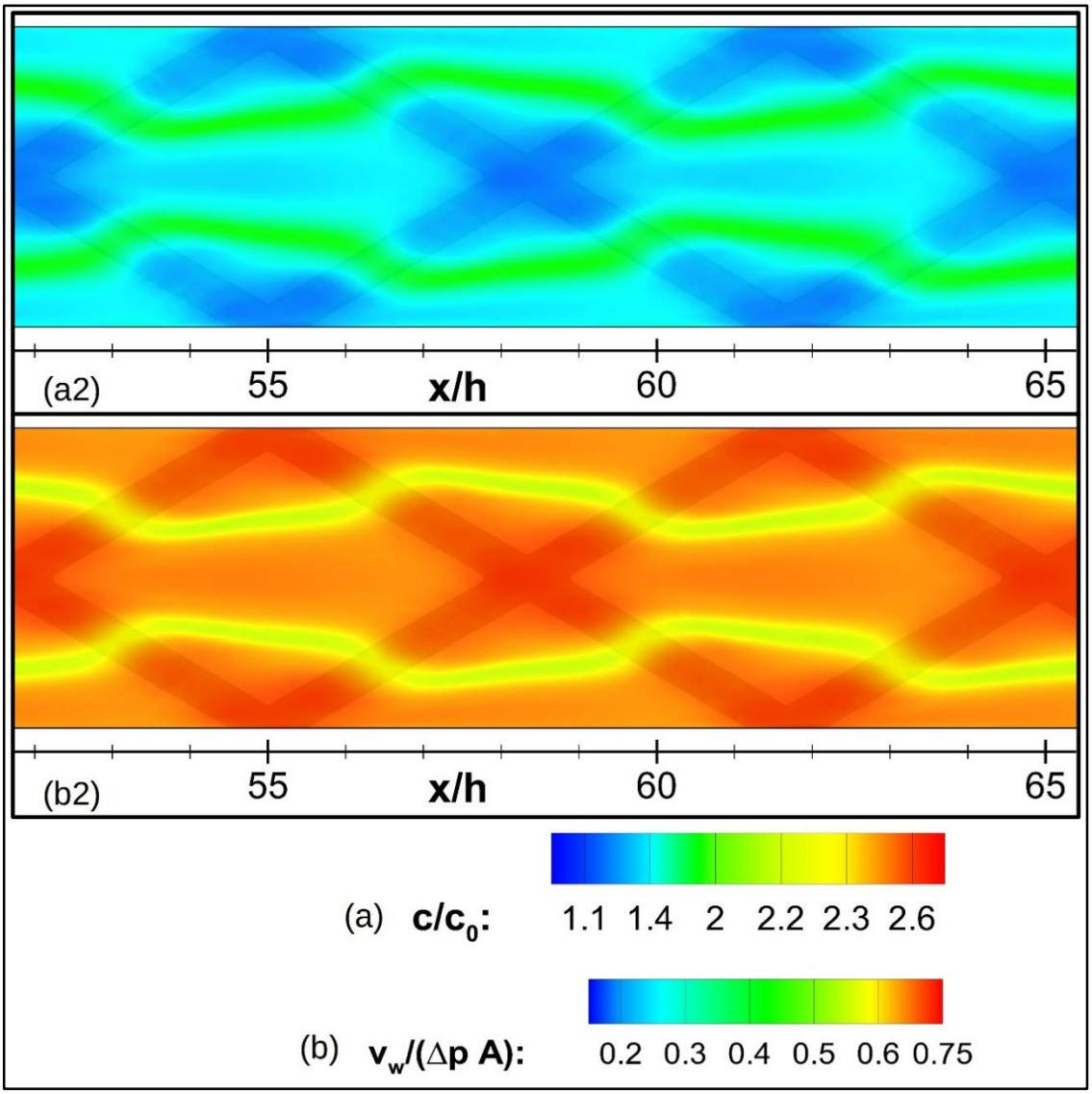

Figure 37: (Continued)

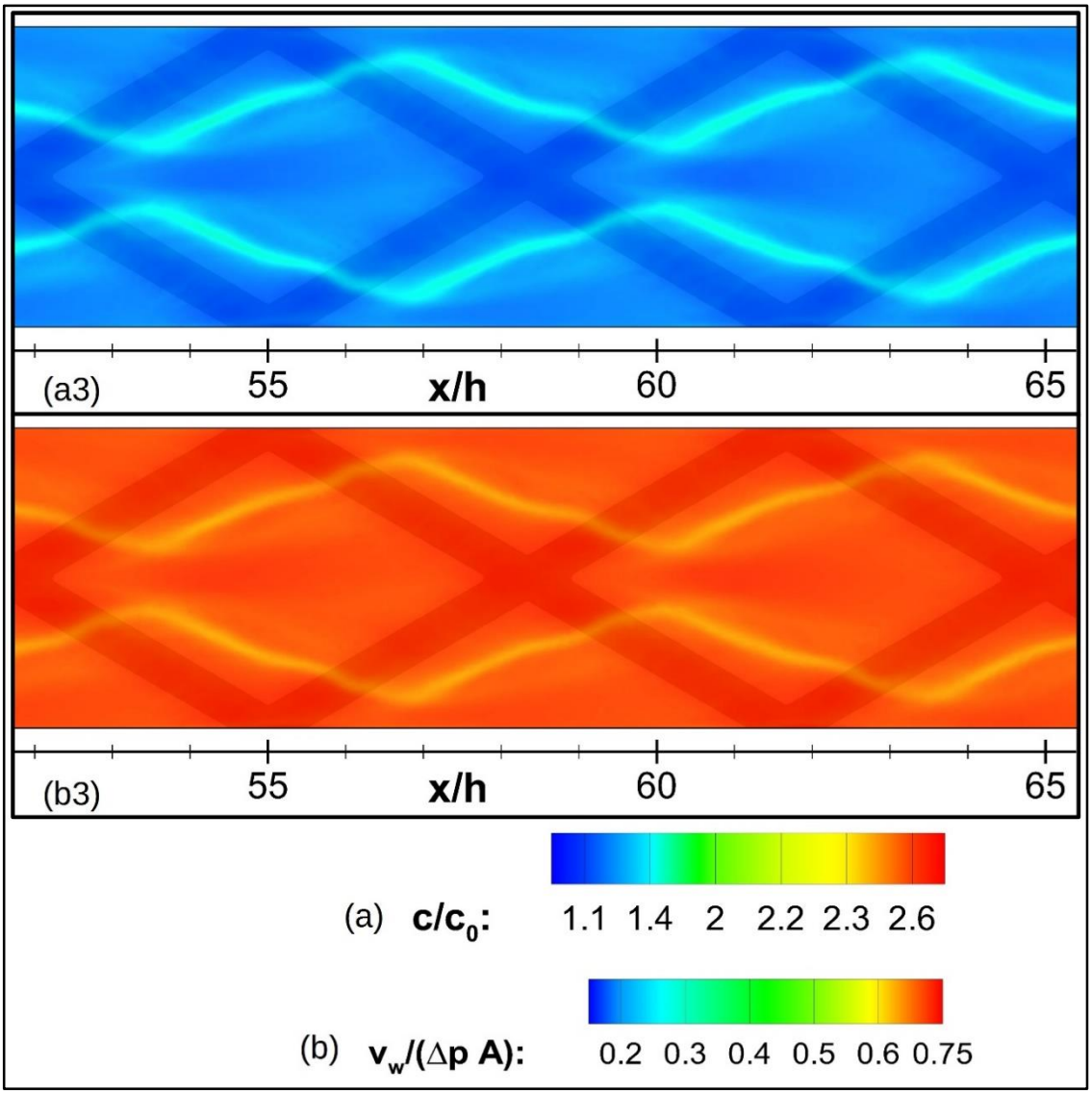

Figure 37: (Continued)

Contours of the local Sherwood number and the normalized local wall shear stress along the surface of the top membrane are shown in Figure 38 for Re of 100, 400 and 800. The local Sherwood number is evaluated from $Sh = (2h)h_m/D$. Images labelled by (a) denote contours of Sherwood number and while images labelled by (b) denote contours of wall shear stress at Re of 100 (labeled 1), 400 (labeled 2) and 800 (labeled

3). The wall shear stress is normalized by the maximum value of the shear stress for each value of Re. The maximum value of the wall shear stress is 0.7, 3.1 and 7.4 Pa, respectively, for Re of 100, 400 and 800. Regions where Sherwood number assumes low values coincides with regions where the concentration polarization occurs, as illustrated in Figure 37a and 38a. The maximum value of Sherwood number is attained in the region above the intersection of strands. That region also coincides with the low concentration regions of the membrane. Sherwood number increases more than four folds as Re is increased from 100 to 800, as depicted in Figure 38a. It is previously documented that fouling potentially occurs in regions of low wall shear stress [53–55]. The low shear region along the membrane coincides with regions of low Sherwood number. It is deducted from these results that regions where concentration polarization occurs are strongly correlated with regions where potential fouling could occur. The intensity of local wall stress increases drastically as Re is increased to 800, implying the probability of occurrence of fouling is much lower at higher flow rates. It is also important to note that the presence of grid of spacers increases the intensity of wall shear stress. Therefore, the occurrence of fouling buildup is less likely in the separation module containing a net of spacers. In fact, it is documented by Park et al. [56] that the spacer arrangement strongly influences the characteristics of the fouling buildup along the surface of the membrane in a desalination module.

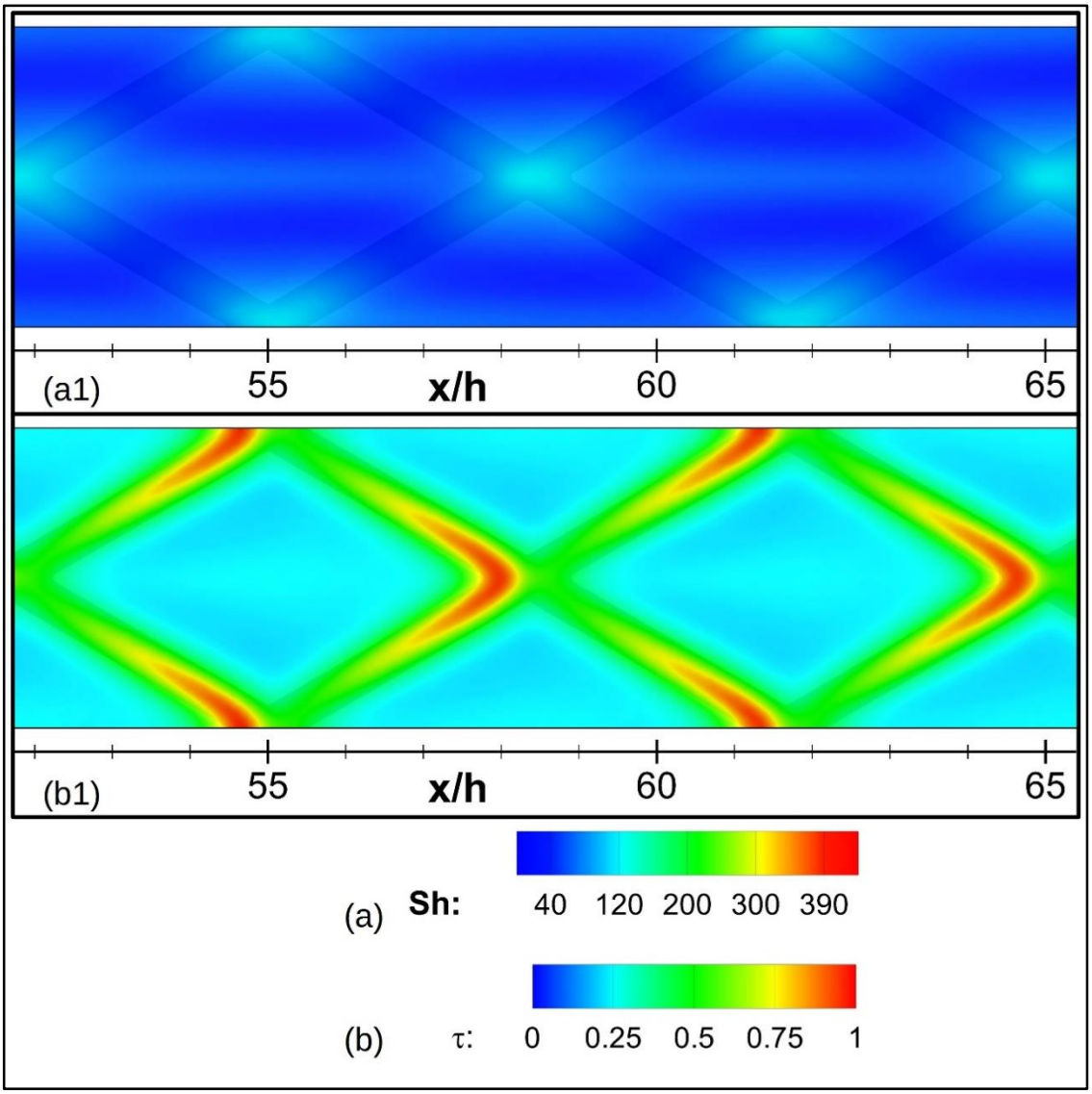

Figure 38: (a) Contours of the Sherwood number along the surface of the top membrane and (b) contours of the normalized wall shear stress along the top membrane. 1, 2 and 3 denote contours at Re = 100, 400 and 800, respectively. The contours are determined in a feed channel containing mesh of spacers with an angle of 30 ^{0}.

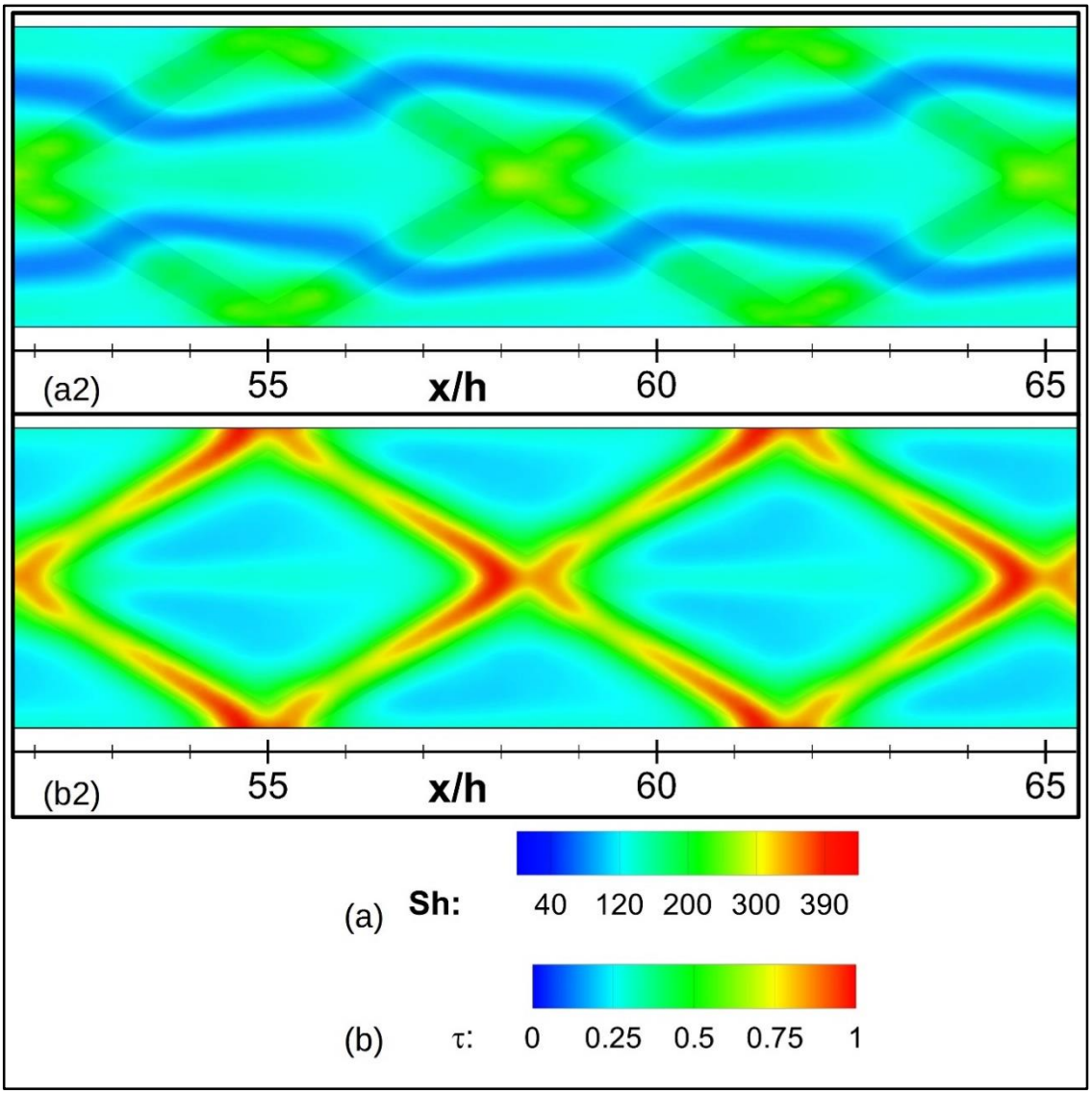

Figure 38: (Continued)

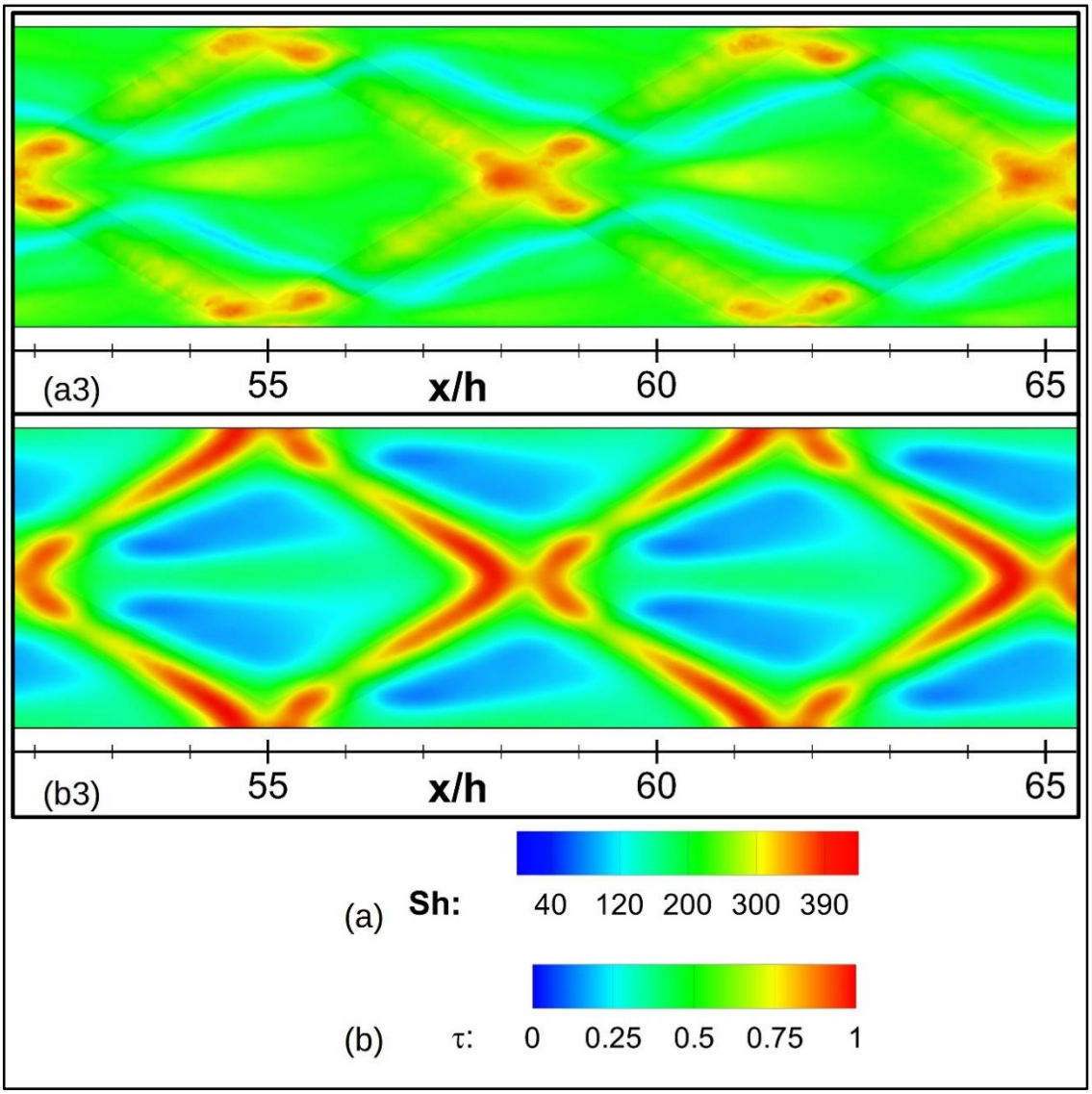

Figure 38: (Continued)

5.2.2. 45° GEOMETRY:

Figure 39 shows the iso-surfaces of the normalized stream-wise component of the velocity and the normalized y-component of vorticity in a feed channel containing a net of spacers in the $45°$ arrangement. The high speed flow is observed in the middle section of the cell and above the strands of spacers at low flow rates. As Re is increased, the high speed flow region in the middle of cell shrinks while the high speed flow region above strands grows. The intensity of the vorticity is greater near the forward and the backward stagnation regions of strands at $Re = 100$. The intensity of vorticity in the middle region of cell increases as Re is increased to 800, as shown in Figure 39b. Flow structures in the feed channel containing a net spacers in the $45°$ arrangement are similar to those in the feed channel containing a net of spacers in the $30°$ arrangement. The only noticeable difference is that the high vorticity region in the feed channel with $45°$ spacer grid is confined to the middle section of the cell. This implies that the mixing in this geometry may not be as effective as in the case for spacer grid with $30°$. In this geometry, strands of spacer face the flow more directly, which results in acceleration of fluid toward the center region. That will increase the drag forces exerted by the fluid on the strand of the spacers.

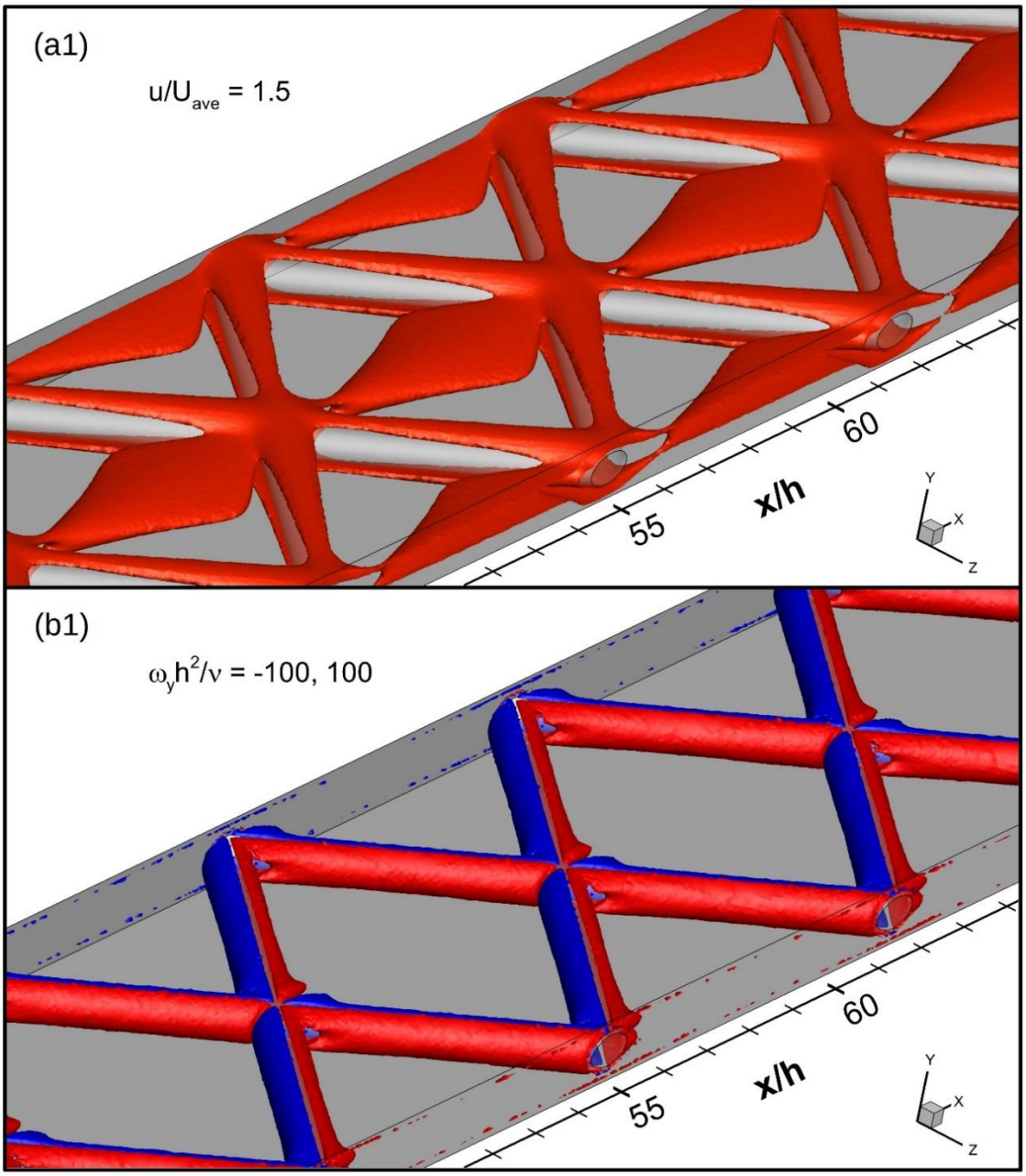

Figure 39: Iso-surfaces of (a) normalized the stream-wise component of the velocity and (b) normalized y-component of the vorticity. 1, 2 and 3 denote iso-surfaces at Re = 100, 400 and 800, respectively. The images are acquired in a feed channel containing mesh of spacers with an angle of 45 ^{0}.

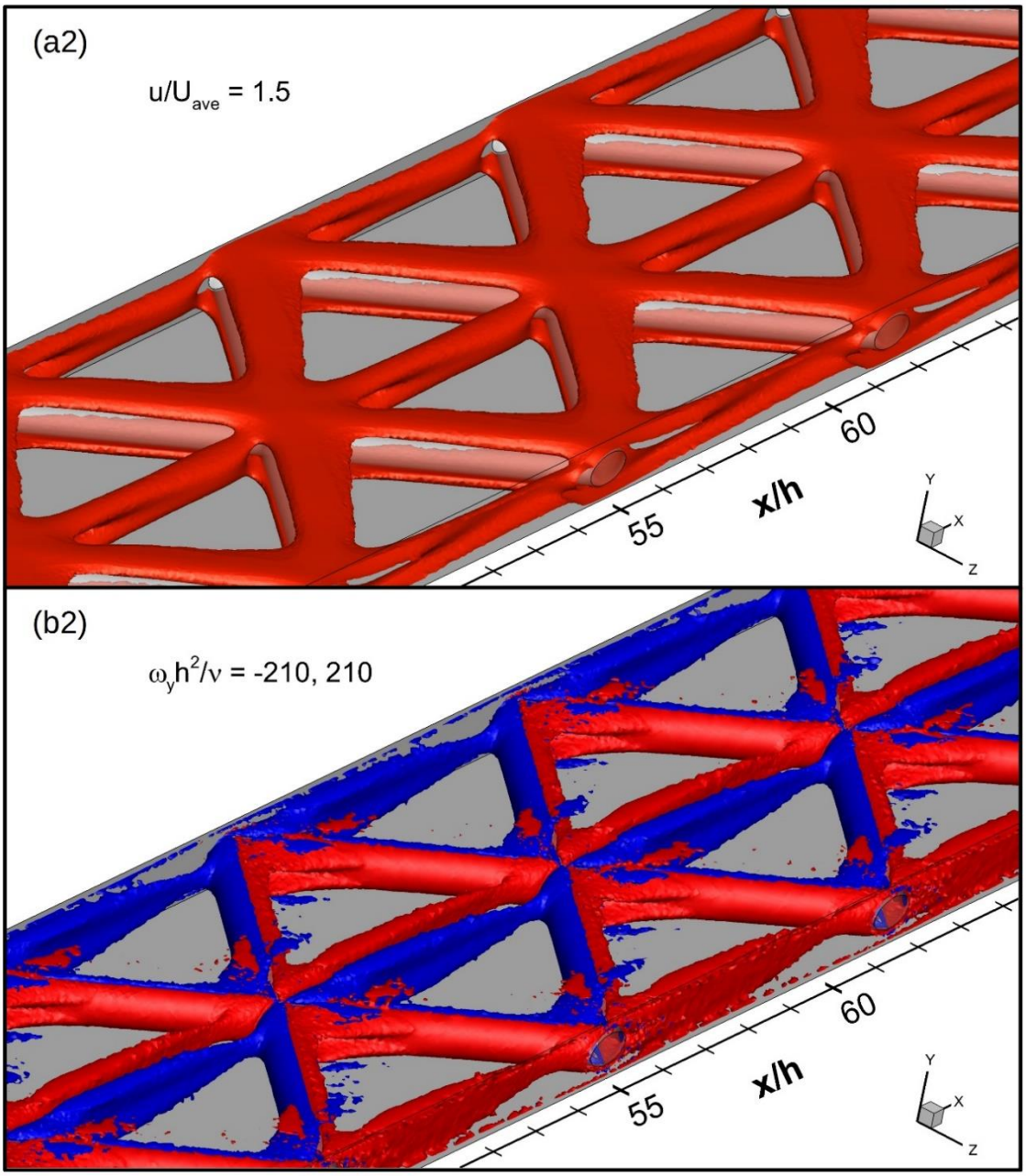

Figure 39: (Continued)

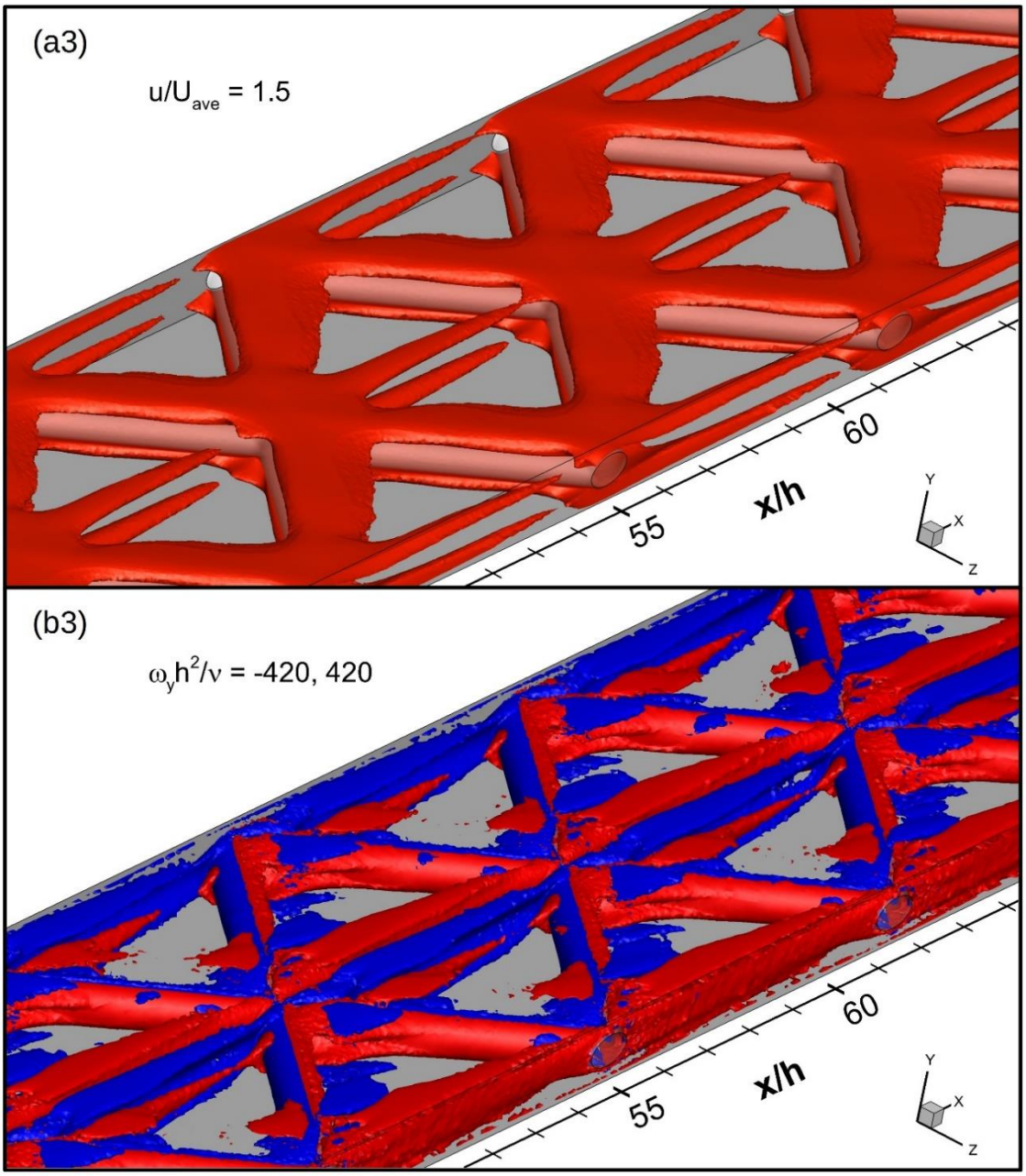

Figure 39: (Continued)

Figure 40 illustrates contours of the normalized salt concentration and the water flux along the surface of the top membrane. The distribution of salt concentration in the geometry with $\theta = 45°$ exhibits strikingly different patterns compared to that with $\theta = 30°$ at $Re = 100$, as shown in Figure 40a1 and 37a1. Concentration polarization occurs everywhere in the cell except along the centerline and at regions above the strands. This is proving that the mixing is not as effective in this geometry at $Re = 100$. As Re is increased to 400 and 800, distribution of concentration along the surface of the membrane becomes similar to that with $30°$ grid. There is a clear indication that enhanced mixing at high flow rates helps reducing the level of concentration polarization, as depicted in Figure 40a2 and 40a3. Water flux is lower in the region where concentration polarization occurs. In a similar manner, the water flux distribution is strongly influenced by the spacer arrangement. Bands of low water flux region extend in the stream-wise direction, as depicted in 40b. The rate at which water passes through the membrane increases drastically as Re is increased from 100 to 800.

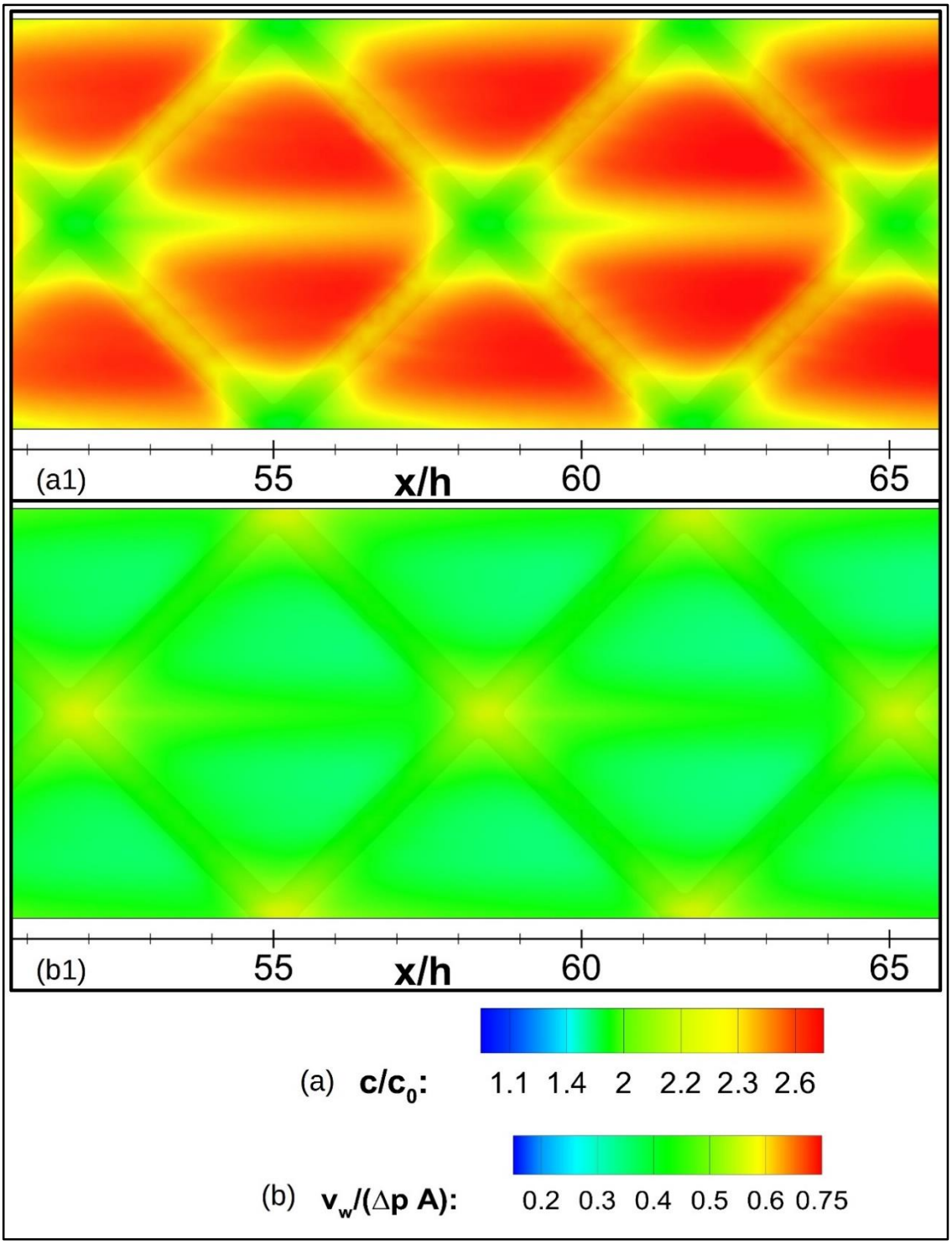

Figure 40: (a) Contours of normalized concentration along the surface of the top membrane and (b) contours of the normalized water flux through the top membrane. 1,2 and 3 denote contours at Re = 100, 400 and 800, respectively. The contours are determined in a feed channel containing mesh of spacers with an angle of 45 ^{0}.

s

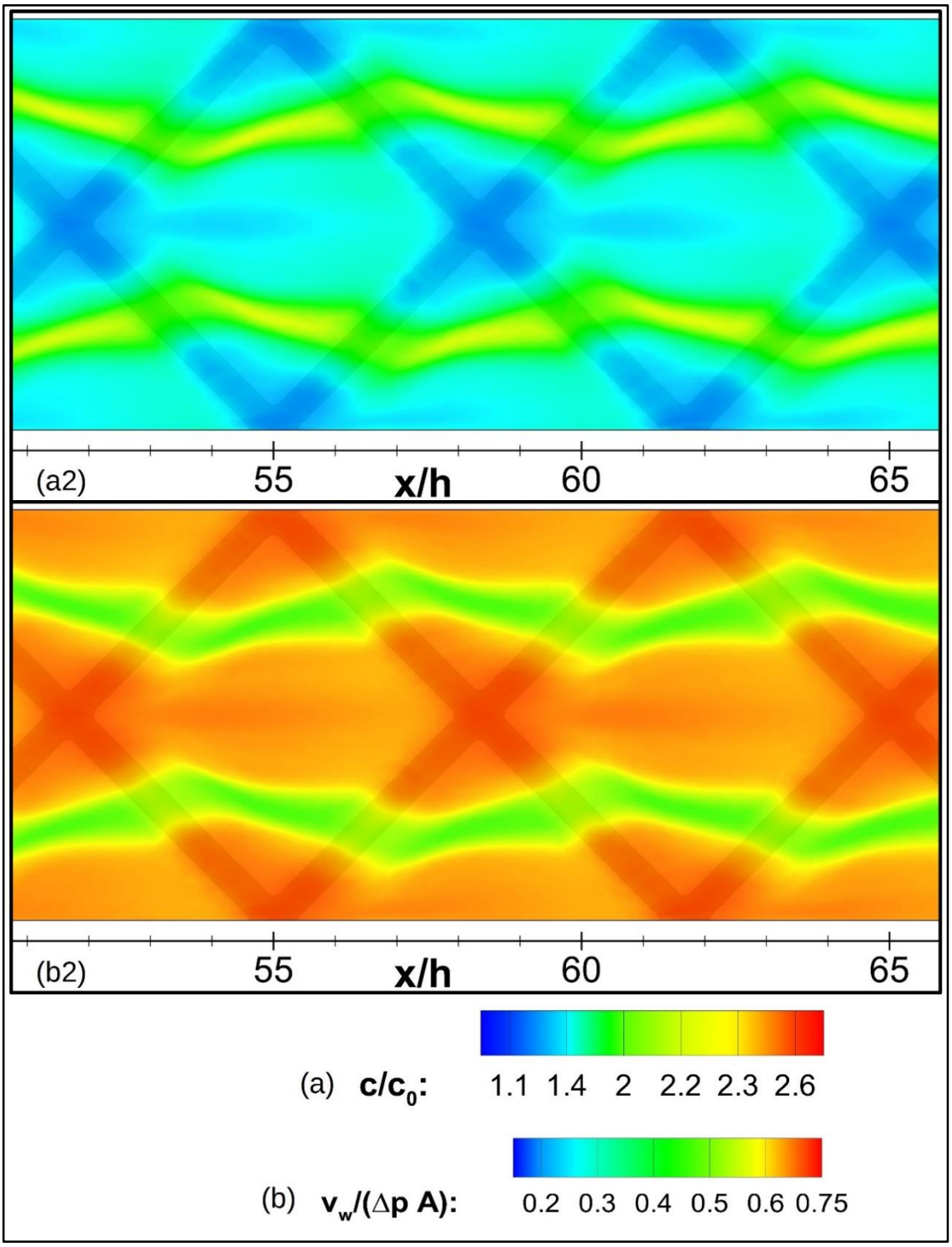

Figure 40: (Continued)

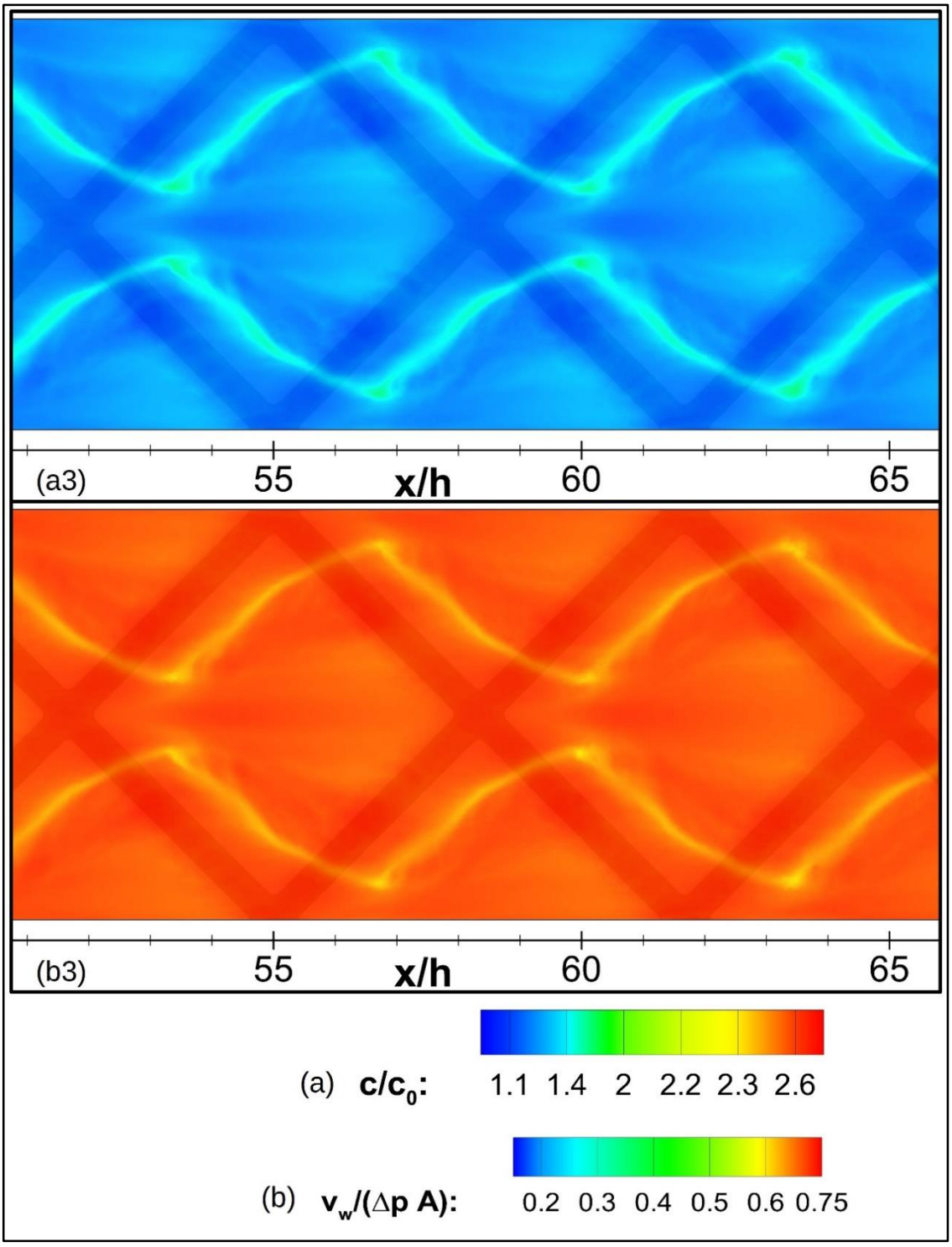

Figure 40: (Continued)

Contours of the local Sherwood number and the normalized local wall shear stress are illustrated in Figure 41. The maximum value of the wall shear stress along the surface of the top membrane is 0.9, 4.3 and 10.6 Pa, respectively, for $Re = 100, 400$ and 800. The intensity of wall shear stress is greater in this geometry compared to that in the geometry with $30°$. Sherwood number overall increases more than five folds as Re is increased from 100 to 800, as shown in Figure 41a. High Sherwood number regions correlate directly with regions of low concentration polarization. Regions of low wall shear stress also directly correlates with regions of high concentration polarization. The probability of occurrence of fouling is greatly reduced as flow rate is increased, as illustrated in Figure 40Figure 41.

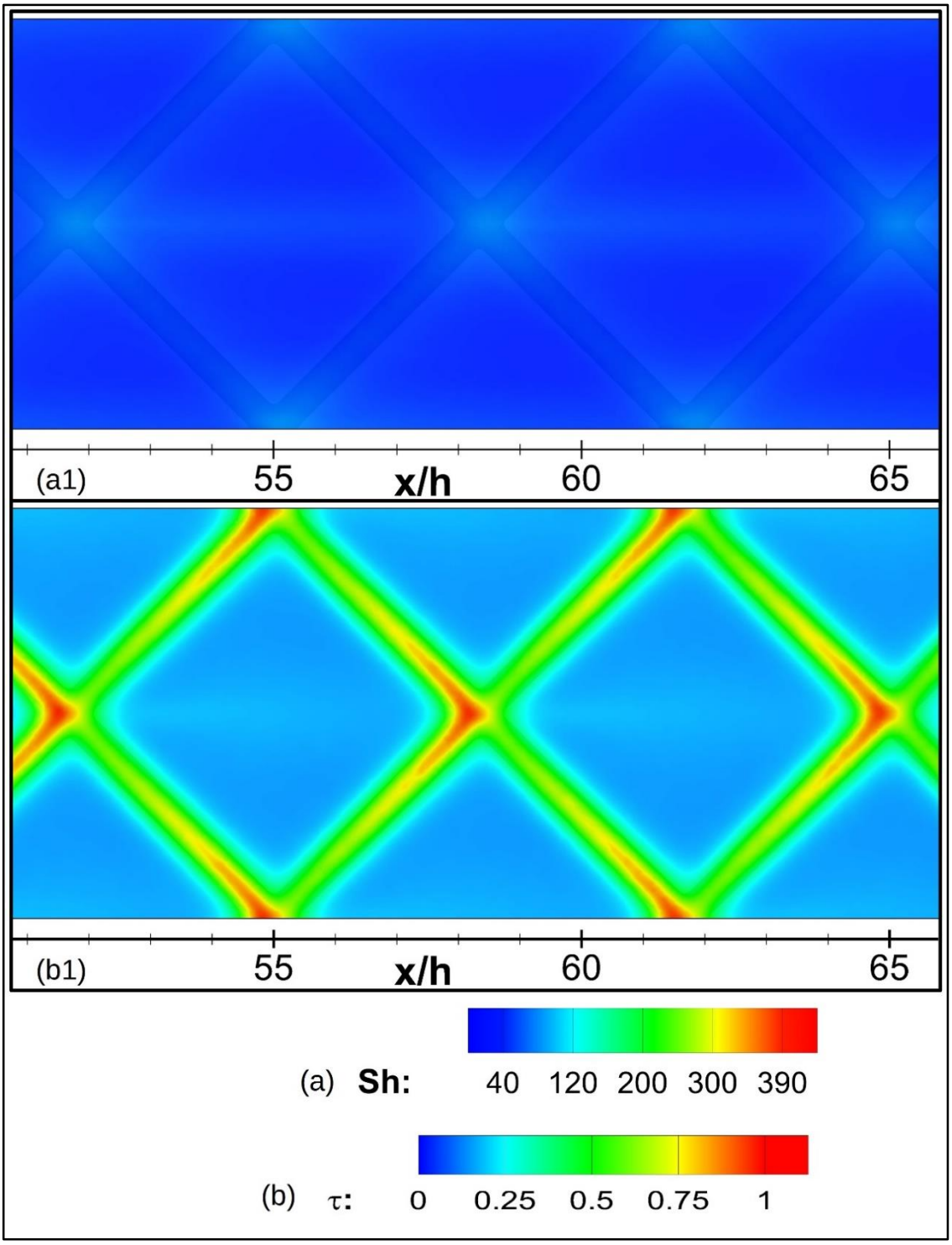

Figure 41: (a) Contours of the Sherwood number along the surface of the top membrane and (b) contours of the normalized wall shear stress along the top membrane. 1, 2 and 3 denote contours at Re = 100, 400 and 800, respectively. The contours are determined in a feed channel containing mesh of spacers with an angle of 45 ^{0}.

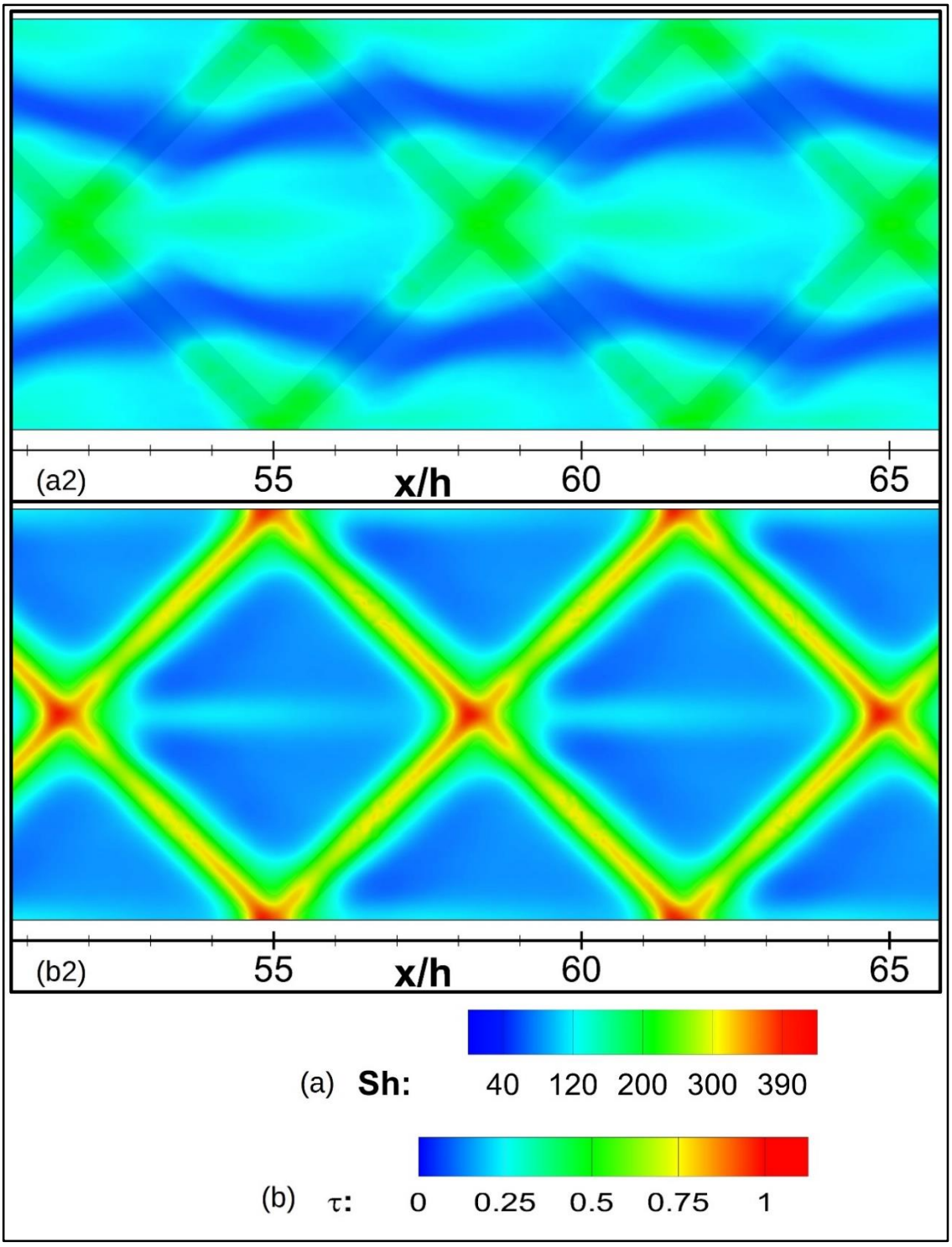

Figure 41: (Continued)

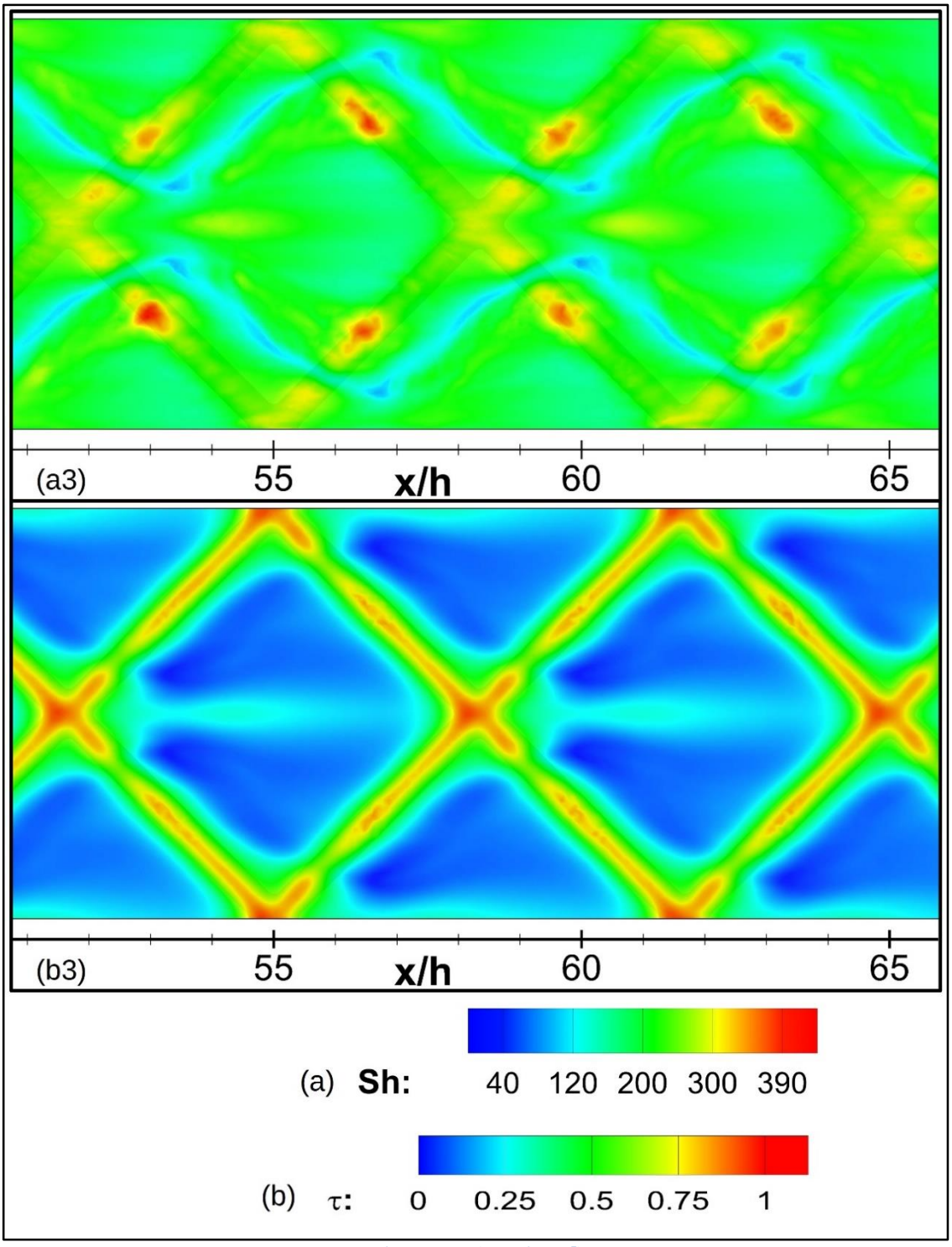

Figure 41: (Continued)

5.2.3. $60°$ GEOMETRY:

Iso-surfaces of the stream-wise component of the velocity and the y-component of the vorticity are plotted in Figure 42 in a feed channel containing a net of spacers in the $60°$ arrangement. Iso-surfaces of both velocity and vorticity at $Re = 100$ are similar to those for geometries with $30°$ and $45°$. At higher flow rates a flow transition occurs. Iso-surfaces of the velocity and the vorticity become streaky in the span-wise direction as a manifestation of flow transitions. The flow transition observed in this geometry is very similar to that observed in the feed channel containing arrays of spacers situated perpendicular to primary flows, as documented in Ref [54] and presented in Chapter 4. The geometry that was considered in Ref [54] is similar to the geometry contains a net of spacer in the $90°$ arrangement, and it is referred as the ladder-type spacer arrangement. The streaks are not perfectly periodic as in the geometry of ladder-type spacer. The intensity of vorticity and velocity is greater near the middle of cells. Flow field is three-dimensional even at low flow rates unlike the flow structure obtained in the feed channel with ladder type spacers, as depicted in Figure 42.

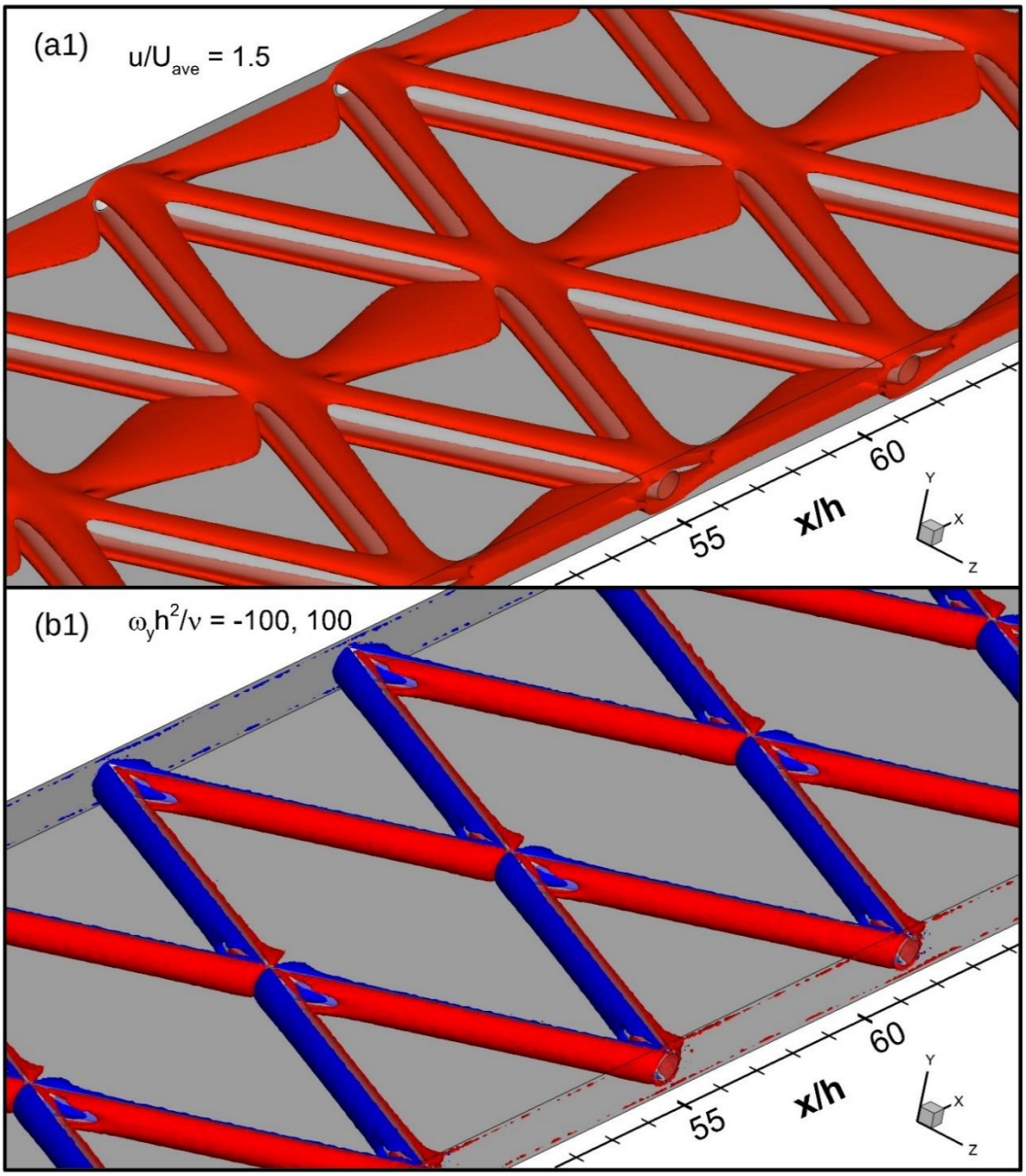

Figure 42: Iso-surfaces of (a) normalized the stream-wise component of the velocity and (b) normalized y-component of the vorticity. 1, 2 and 3 denote iso-surfaces at Re = 100, 400 and 800, respectively. The images are acquired in a feed channel containing mesh of spacers with an angle of 60 ^{0}.

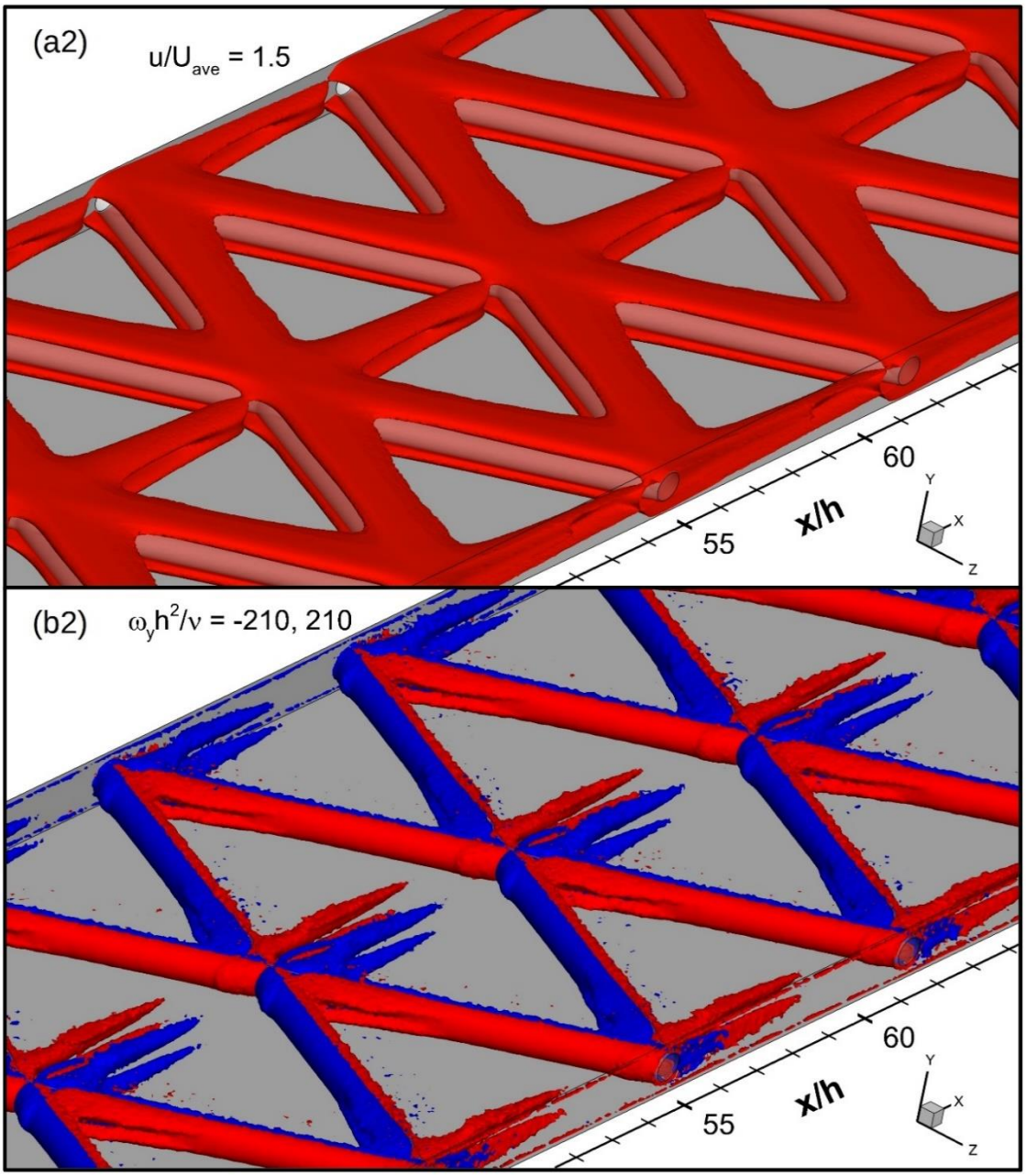

Figure 42: (Continued)

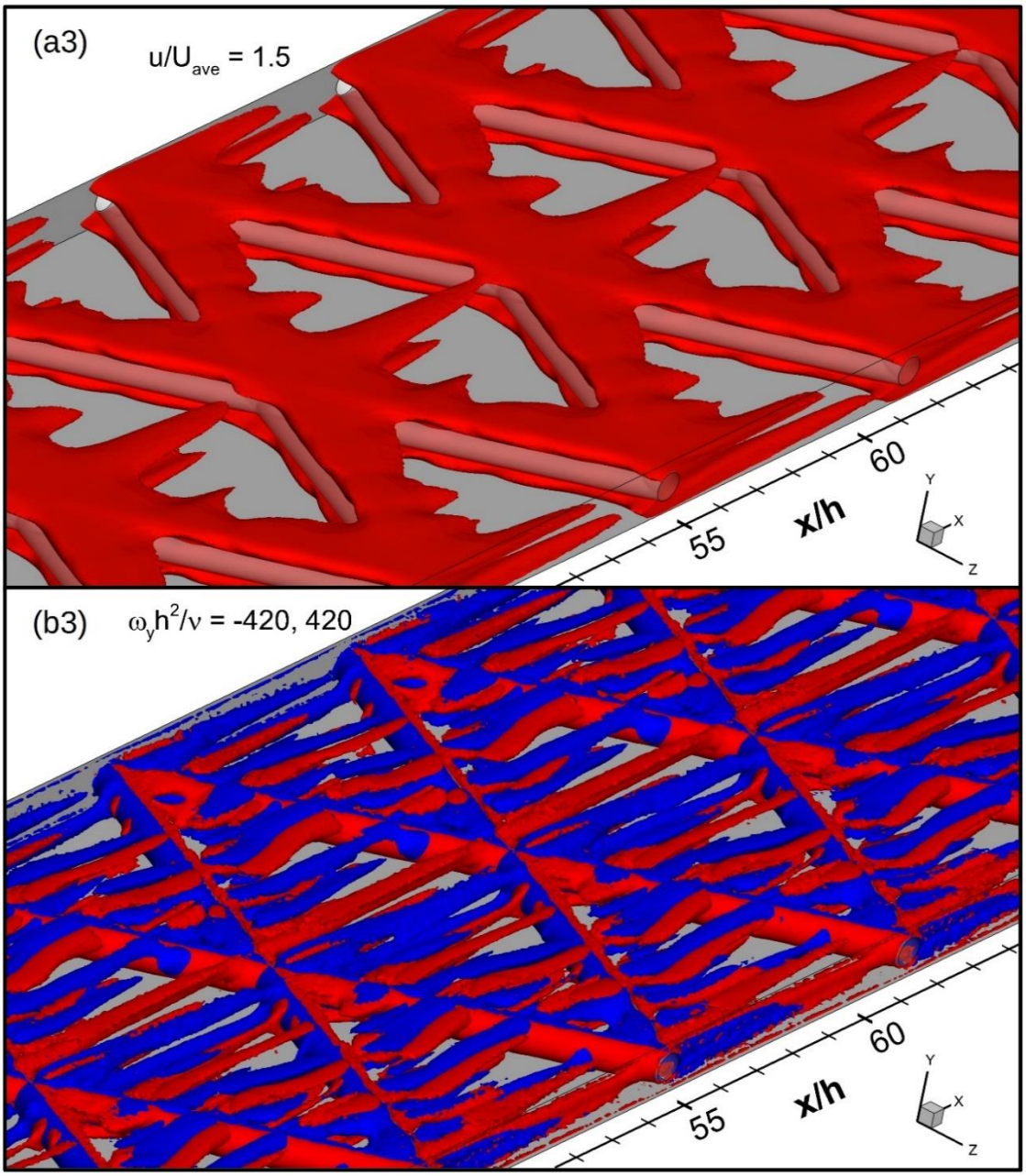

Figure 42: (Continued)

Sherwood number is nearly uniform along the surface of the membrane at $Re = 100$. It is slightly elevated in the regions above the strands of spacers. Sherwood number becomes streaky at Re of 400 and 800, as seen in Figure 44a2 and 44a3. Sherwood number increases significantly as Re is increased. The intensity of wall shear stress is immensely larger in the regions above the strands of spacers compared to the center region of cells. The streaky patterns in the wall stress distribution is clearly present at $Re = 800$, as depicted in Figure 44b3. These results demonstrate that fouling could also occur with a streaky pattern in this geometry inside the cells. It is abundantly clear that a grid of spacers in the feed channel creates strong three-dimensional flows. That in turn induce robust momentum mixing. As a result the membrane performance such as the water flux, concentration polarization and the potential fouling buildup is immensely altered. It is also important to note that binary fluid flows studied here could be transient. The effects of such transient flows on the membrane performance could also be significant. Transient nature of the flows and its influence on the membrane performance for few selected geometries and flow rates can be investigated as a future study.

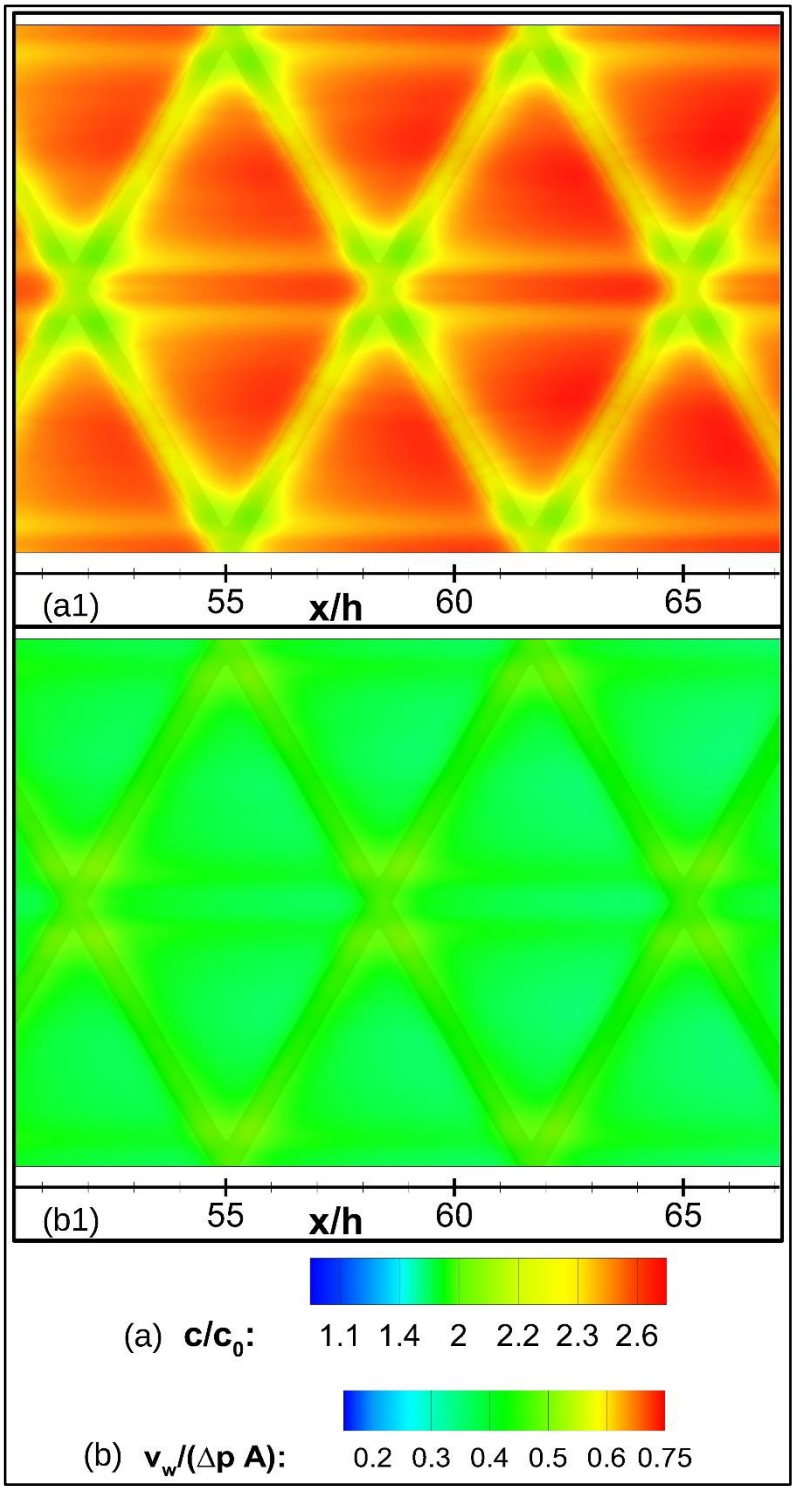

Figure 43: (a) Contours of normalized concentration along the surface of the top membrane and (b) contours of the normalized water flux through the top membrane. 1, 2 and 3 denote contours at Re = 100, 400 and 800, respectively. The contours are determined in a feed channel containing mesh of spacers with an angle of 60 ^{0}.

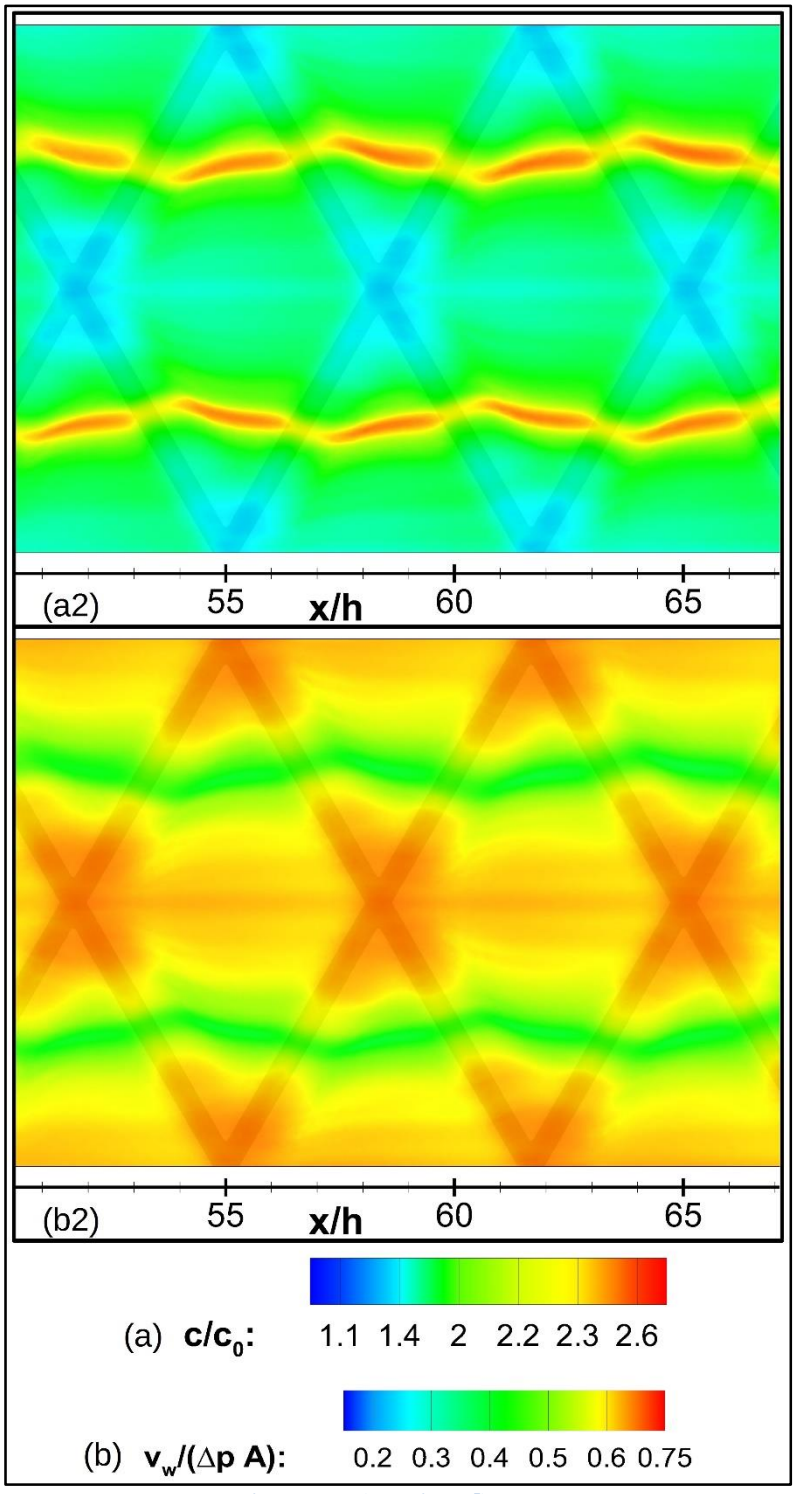

Figure 43: (Continued)

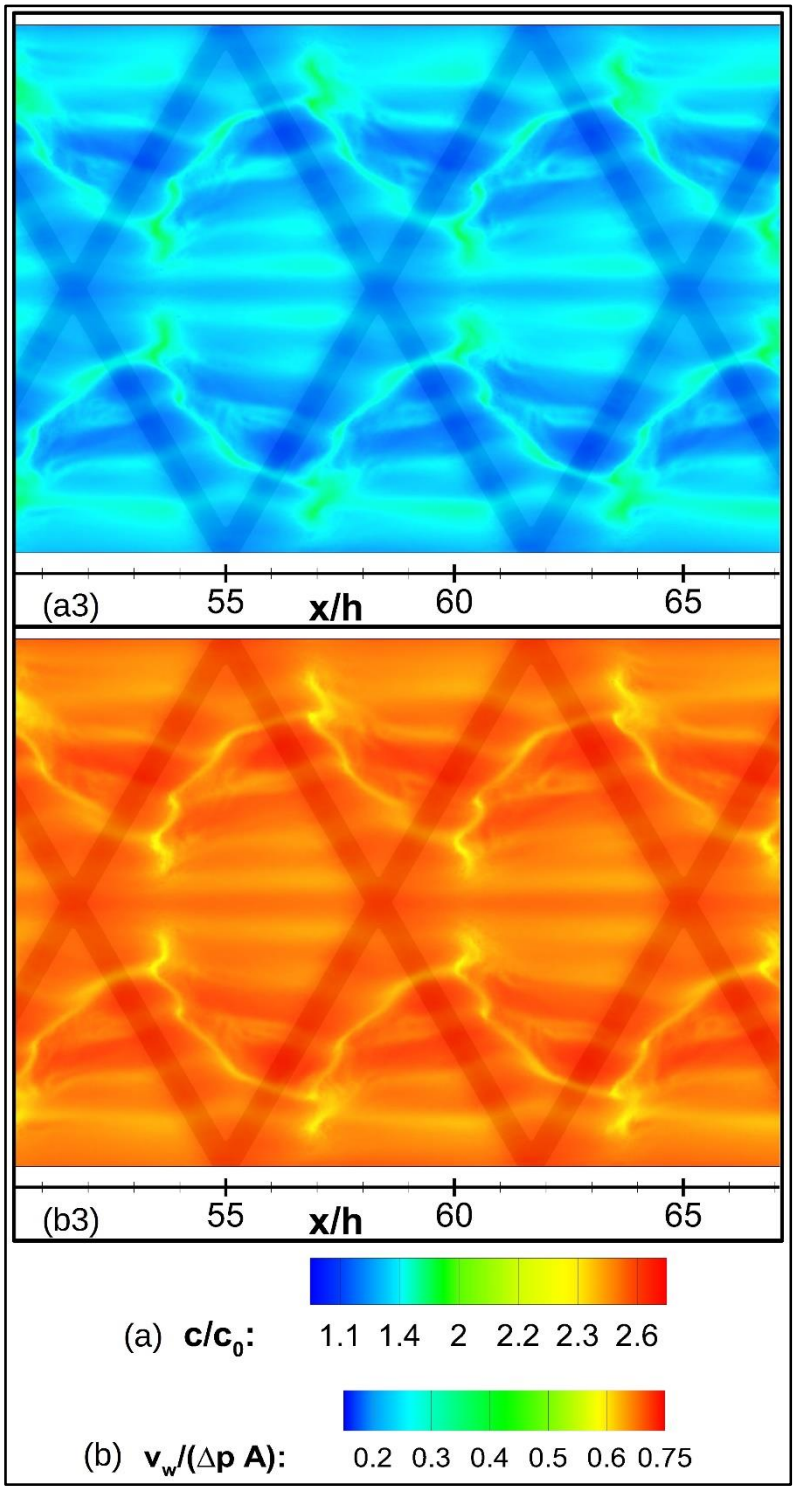

Figure 43: (Continued)

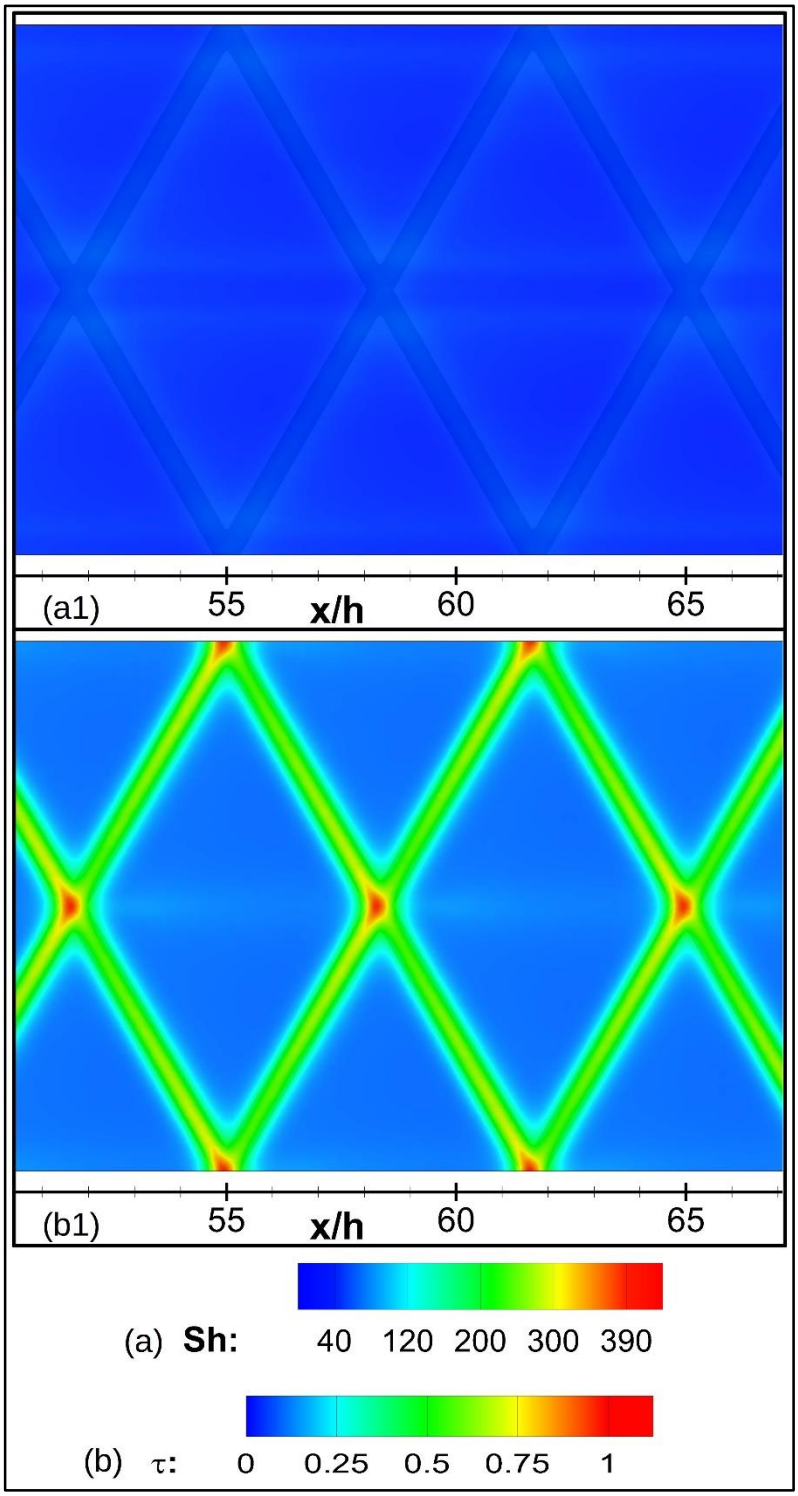

Figure 44: (a) Contours of the Sherwood number along the surface of the top membrane and (b) contours of the normalized wall shear stress along the top membrane. 1, 2 and 3 denote contours at Re = 100, 400 and 800, respectively. The contours are determined in a feed channel containing mesh of spacers with an angle of 60 ^{0}.

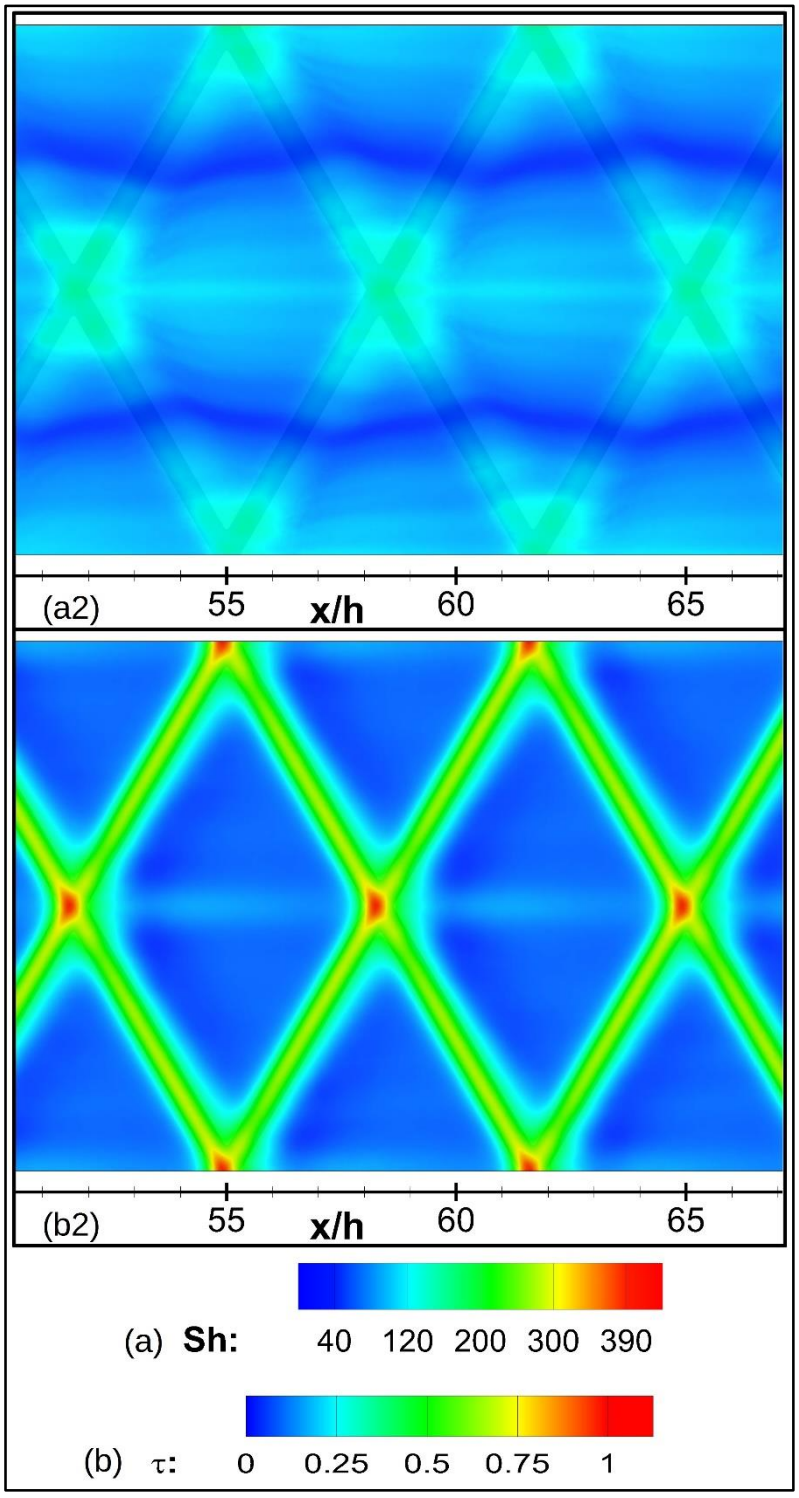

Figure 44: (Continued)

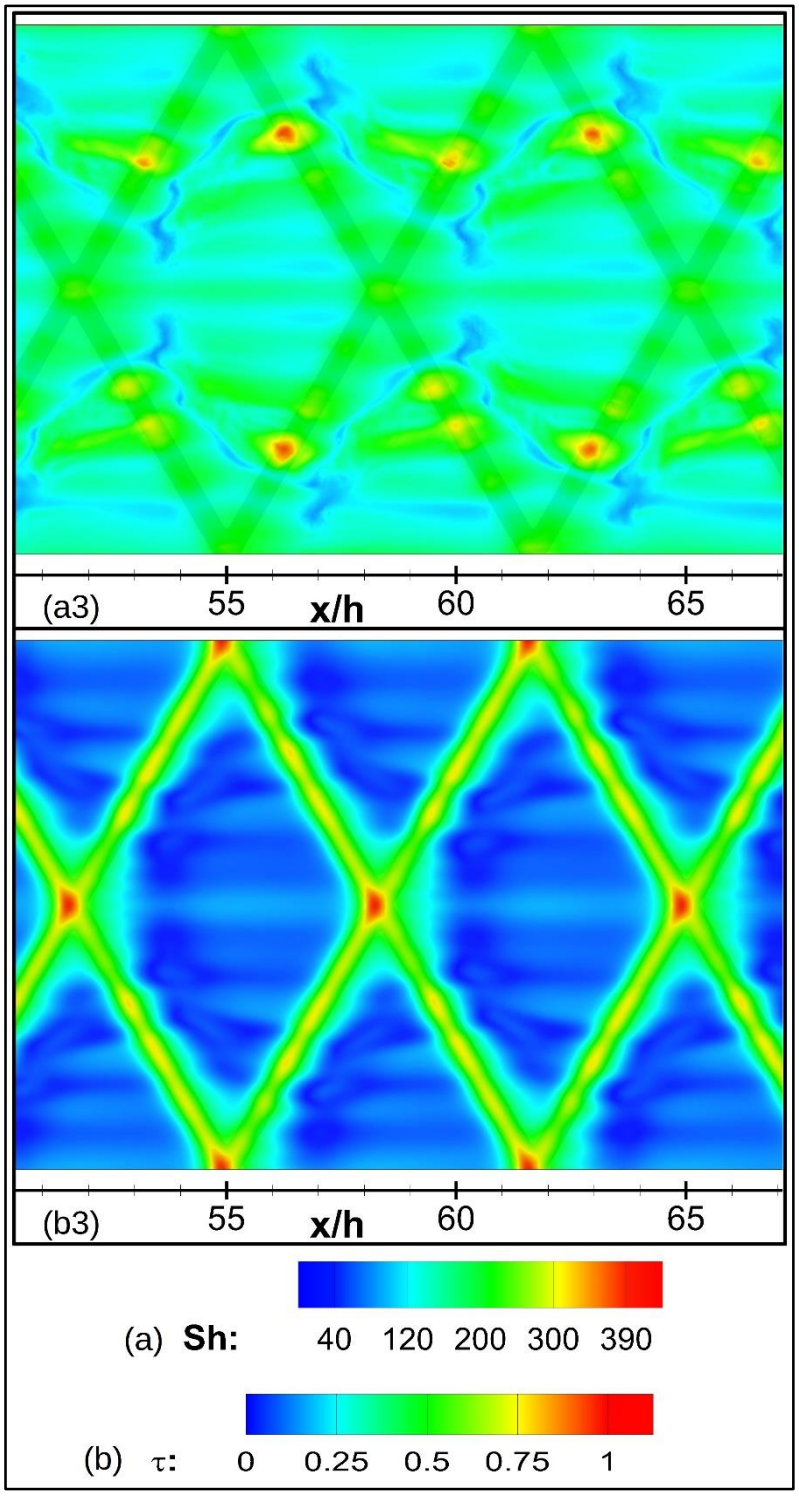

Figure 43: (Continued)

5.2.4. COEFFICIENT OF PERFORMANCE:

The coefficient of performance, CP, is introduced to compare performance of membrane modules. The friction factor, f, is averaged over $38 \leq x/h \leq 76.7$. The coefficient of performance, also referred as the merit number, measures membrane mass flux performance for the same pumping power. The coefficient of performance is calculated as $CP = (Sh/Sh_0)(f_0/f)^{1/3}$. Membrane module containing three different spacer grids are evaluated at Re of 100, 400 and 800. Table 2 lists the average friction coefficient, the average Sherwood number and the coefficient of performance for each grid at different flow rates. For all geometries, the friction factor decreases rapidly as the flow rate increases. It is also shown that Sherwood number increases with increasing flow rates in all channels. As θ increases, the average friction factor increases and the average Sherwood number decreases at all flow rates. The mass flux is greatly improved for modules containing a net of spacers at all flow rate considered in this study. This enhancement comes with a penalty of increasing pressure drop or increasing pumping power. In order to claim that membrane module with a net of spacers is an effective design the merit number should be greater than unity. All membrane modules considered in the study have the merit number less than unity at $Re = 100$. For $Re = 400$ the merit number is greater than unity in geometries with 30° and 45°, but it is less than unity for the geometry with 60°. The net of spacers with 30° is the most effective design among all modules studied here at all flow rates. The coefficient of performance for all geometries increases as the flow rate is increased, as listed in Table 2. The merit number or the coefficient of performance discussed here only considers the mass flux in

determining the membrane performance. Concentration polarization and characteristics of fouling buildup have to be incorporated in determining the performance characteristics of the membrane modules. It is shown above that all these geometries help mitigating the concentration polarization and the fouling buildup at all flow rates compared to modules without spacers.

	Channel without spacer		$\theta = 30°$			$\theta = 45°$			$\theta = 60°$		
Re	f_s	$\overline{Sh}_s$	f	$\overline{Sh}$	CP	f	$\overline{Sh}$	CP	f	$\overline{Sh}$	CP
100	0.187	31	0.986	50	**0.94**	1.007	41	**0.76**	1.067	39	**0.72**
400	0.051	46	0.352	131	**1.51**	0.386	106	**1.18**	0.439	82	**0.87**
800	0.027	57	0.235	215	**1.85**	0.274	201	**1.64**	0.321	155	**1.20**

Table 2: Performance parameters.

5.3. CONCLUSION

Simulations have been conducted to characterize three-dimensional multicomponent fluid flows in a feed channel of a reverse osmosis membrane module. The feed channel consists of a net of spacers in different arrangements. Computational fluid dynamics simulations are performed for Re of 100, 400 and 800 in geometries with strand angle of 30°, 45° and 60°. The laminar model is employed to characterize flow structures at $Re = 100$, while the SST k-ω turbulence model is employed to determine flow structures at $Re = 400$ and 800. The membrane is treated as a functional surface where the water flux and the concentration gradient are determined from the local pressure and the concentration. The present study illustrates that three-dimensional flows induced by the spacers in the feed channel have profound influence on the membrane performance. The high concentration polarization regions coincide

with low flux regions, and these regions also correlate directly with low shear regions where potential fouling buildup occurs. The presence of net of spacers in the feed channel aids mitigating the concentration polarization and aids minimizing potential fouling buildup. The membranes with all geometries perform much better at higher flow rates. The grid of spacers in the 30° arrangement offers the most efficient membrane modules at all flow rates considered. The coefficient of performance based on efficient mass transfer indicates that the angle of spacer with 30° is very effective at Re of 400 and 800. This study clearly demonstrates that the spacer arrangement should be an integral part of the optimization process of membrane modules in desalination systems.

CHAPTER 6: SUMMARY

Computational study performed here examines the flow and mass transport in the feed channel of a spiral wound membrane in the water desalination. The membrane produces fresh water via reverse osmosis process. The membrane flux model employed here is the solution-diffusion model that is well-documented. The membrane is treated as a functional surface where water mass flux, salt concentration gradient and pressure are coupled together. The investigation included two- and three-dimensional flow and mass transport simulations. Extensive mesh size studies are carried out to assure that results are mesh size independent. The membrane modeling is validated by comparing results predicted by the present model against results reported in the literature. The validation proves that the membrane flux model employed in this study is reliable and that it can accurately predict the membrane performance and the mass transport through the membrane.

The simulations for two-dimensional flow prove that the presence of spacers in the feed channel improves the fresh water production and aids in mitigating the concentration polarization along the membrane surface. The effects of the spacers on the membrane performance are shown to be more pronounced. The staggered arrangement of spacers with $e/h = 1/8$ leads to the best alleviation of the concentration polarization at $Re = 800$ when it is compared with open channel. Similarly, the water flux improves the best at $Re = 800$ in the staggered geometry with $e/h = 1/8$. It is noticed that there is a better enhancement of the water flux and concentration polarization mitigation when the spacers are placed closer to each other.

In all, geometries, the spacers show no significant influence on the concentration polarization or on the water flux at $Re = 4000$ when it is compared with open channel. The flow in open channel is in the turbulent regime at $Re = 4000$, and momentum mixing exists without presence of spacers. The transient large eddy simulation (LES) has been conducted to validate predictions obtained by steady flow simulations using SST k-ω turbulence model. The LES transient results are in a good agreement with the steady turbulent simulations. The shape of the spacers has no discernible influence on the membrane performance at any flow rates. The averaged value of Sherwood number and the water flux along the membrane surface increases as the feed flow rate increases. It is also noticed that the averaged Sherwood number and water flux are higher when the distance between spacers is shorter. However, the pressure drop increases drastically by placing the spacers closer to each other. The increase in pressure drop translates an increase in pumping power of the feed fluid. That in turn results in an increase in the production cost. In order to assess the RO membrane performance properly, the rate of water permeate or Sherwood number and the pressure drop should be considered. These parameters should be an integral part of the design and optimization of desalination modules.

Flows in a feed channel containing spacers are inherently three dimensional and transient in nature. It has been documented in the literature that flows past cylinders (even a single cylinder) becomes three dimensional at flow rates above criticality. It is also documented in the literature that flows in the feed channel containing spacers becomes unsteady at flow rates above criticality. The present study emphasizes that the influence of three dimensional flow structures on the membrane performance,

concentration polarization and fouling and scaling characteristics in the desalination modules. Preliminary analyses are conducted here to study the influence of transient nature of the flow on the membrane performance in a desalination module.

Steady three-dimensional flow simulations have been performed in a channel containing circular cross-sectioned spacers. Average properties characterizing membrane flux performances and pressure drop or friction factors in the feed channel can be predicted accurately by two dimensional modeling and analyses. However, for the range of flow rates considered in the present study the flow in the feed channel becomes three-dimensional. Three-dimensional flow structures induced by the flow transitions strongly influence the characteristics of the concentration polarization along the surface of the membrane. Flow structures become streaky and strongly three dimensional at higher flow rates. These streaky vortical structures may not influence the average mass flux properties of spiral wound membranes, but they have profound effects on the concentration polarization characteristics and fouling, especially at higher flow rates. Uniformly spaced streaks of high water flux zones occur in the span-wise direction along the membrane surface. Uniformly spaced streaks of low concentration polarization region coincide with streaks of high water flux regions. Concentration polarization is mitigated by three dimensional flows induced by flow transitions. More than 30% reduction of the concentration polarization is achieved as Re increased from 100 to 800. Although, it may not be quantified precisely the same level of reduction in the probability of fouling reduction can be achieved by three dimensional flows induced by flow transitions. Mitigating concentration polarization will improve the membrane

performance significantly. The lifetime of the desalination module will be improved by the reduction of scaling and fouling build up.

Simulations have been carried out for the flow and mass transport in a feed channel containing net of spacers. The net of spacers is used in the industrial reverse osmosis desalination processes. Three dimensional velocity and concentration fields are characterized for values of angle of 30°, 45°, and 60°. Simulations are performed for values of Reynolds number in the range of 400 to 800. The net of spacers leads to three-dimensional flow structures and promotes good momentum mixing in the feed channel. The intensity of the three dimensional flow structures increases rapidly as the flow rate increases. It is demonstrated here that three dimensional flow structured generated by the presence of mesh of spacers in the feed channel strongly influence the membrane performance. The effect of angle on the three dimensional characteristics of the flow is very strong. The presence of net of spacers in the feed channel helps mitigating the concentration polarization at membrane surface and helps the membrane to perform better. The highest level of concentration polarization alleviation and the best enhancement of water flux through the membrane is obtained with a net of spacer with 30° in the feed channel. This conclusion is drawn from calculated coefficient of performance of modules containing the mesh of spacers. The coefficient of performance of different modules is determined for the same pumping power used to operate these modules. Moreover, the presence of net of spacers helps to reduce the fouling potentials along the membrane surface. The fouling potentials can be minimized by creating evenly distributed high level of wall shear along the membrane surface.

This study can be extended by considering flow and mass transfer modeling in both feed and production channel. The velocity and the concentration fields in these channels are coupled through the flux through the membrane separating these channels. The non-linear interactions between the concentration and the pressure field are expected to influence the membrane performance and the water flux through the membrane. Such behavior can be especially significant in multistage seawater desalination by reverse osmosis. This approach can also be employed to predict the performance of corrugated membrane performance.

REFERENCES

[1] L.K. Wang, ed., Membrane and desalination technologies, Humana Press, New York, NY, 2011.

[2] R.W. Baker, Membrane technology and applications, John Wiley & Sons, Chichester, West Sussex; Hoboken, 2012. http://www.123library.org/book_details/?id=54302 (accessed August 23, 2015).

[3] S. Loeb, S. Sourirajan, Sea Water Demineralization by Means of an Osmotic Membrane, in: Saline Water Conversion—II, AMERICAN CHEMICAL SOCIETY, WASHINGTON, D. C., 1963: pp. 117–132. http://pubs.acs.org/doi/abs/10.1021/ba-1963-0038.ch009 (accessed February 7, 2016).

[4] J.E. Cadotte, R.J. Petersen, R.E. Larson, E.E. Erickson, A new thin-film composite seawater reverse osmosis membrane, Desalination. 32 (1980) 25–31. doi:10.1016/S0011-9164(00)86003-8.

[5] J.E. Cadotte, R.J. Petersen, Thin-Film Composite Reverse-Osmosis Membranes: Origin, Development, and Recent Advances, in: A.F. Turbak (Ed.), Synth. Membr., AMERICAN CHEMICAL SOCIETY, WASHINGTON, D. C., 1981: pp. 305–326. http://pubs.acs.org/doi/abs/10.1021/bk-1981-0153.ch021.

[6] S.S. Shenvi, A.M. Isloor, A.F. Ismail, A review on RO membrane technology: Developments and challenges, Desalination. 368 (2015) 10–26. doi:10.1016/j.desal.2014.12.042.

[7] L. Malaeb, G.M. Ayoub, Reverse osmosis technology for water treatment: State of the art review, Desalination. 267 (2011) 1–8. doi:10.1016/j.desal.2010.09.001.

[8] K.P. Lee, T.C. Arnot, D. Mattia, A review of reverse osmosis membrane materials for desalination—Development to date and future potential, J. Membr. Sci. 370 (2011) 1–22. doi:10.1016/j.memsci.2010.12.036.

[9] S. Wardeh, H.P. Morvan, CFD simulations of flow and concentration polarization in spacer-filled channels for application to water desalination, Chem. Eng. Res. Des. 86 (2008) 1107–1116. doi:10.1016/j.cherd.2008.04.010.

[10] H.T. El-Dessouky, H.M. Ettouney, Fundamentals of salt water desalination, 1st ed, Elsevier, Amsterdam ; New York, 2002.

[11] R. Salcedo-Díaz, P. García-Algado, M. García-Rodríguez, J. Fernández-Sempere, F. Ruiz-Beviá, Visualization and modeling of the polarization layer in crossflow reverse osmosis in a slit-type channel, J. Membr. Sci. 456 (2014) 21–30. doi:10.1016/j.memsci.2014.01.019.

[12] Filtration systems | Auxiaqua, (n.d.). http://www.auxiaqua.es/en/sistemas-filtracion/ (accessed January 7, 2016).

[13] J. Schwinge, D.E. Wiley, D.F. Fletcher, A CFD study of unsteady flow in narrow spacer-filled channels for spiral-wound membrane modules, Desalination. 146 (2002) 195–201. doi:10.1016/S0011-9164(02)00470-8.

[14] C.P. Koutsou, S.G. Yiantsios, A.J. Karabelas, A numerical and experimental study of mass transfer in spacer-filled channels: Effects of spacer geometrical

characteristics and Schmidt number, J. Membr. Sci. 326 (2009) 234–251. doi:10.1016/j.memsci.2008.10.007.
[15] M. Kostoglou, A.J. Karabelas, Comprehensive simulation of flat-sheet membrane element performance in steady state desalination, Desalination. 316 (2013) 91–102. doi:10.1016/j.desal.2013.01.033.
[16] J. Schwinge, D.E. Wiley, D.F. Fletcher, Simulation of the Flow around Spacer Filaments between Channel Walls. 2. Mass-Transfer Enhancement, Ind. Eng. Chem. Res. 41 (2002) 4879–4888. doi:10.1021/ie011015o.
[17] J. Schwinge, D.E. Wiley, D.F. Fletcher, Simulation of the Flow around Spacer Filaments between Narrow Channel Walls. 1. Hydrodynamics, Ind. Eng. Chem. Res. 41 (2002) 2977–2987. doi:10.1021/ie010588y.
[18] M. Shakaib, S.M.F. Hasani, M. Mahmood, CFD modeling for flow and mass transfer in spacer-obstructed membrane feed channels, J. Membr. Sci. 326 (2009) 270–284. doi:10.1016/j.memsci.2008.09.052.
[19] V. Geraldes, V. Semiao, M. Norberta de Pinho, Concentration polarisation and flow structure within nanofiltration spiral-wound modules with ladder-type spacers, Comput. Struct. 82 (2004) 1561–1568. doi:10.1016/j.compstruc.2004.03.052.
[20] S.K. Karode, A. Kumar, Flow visualization through spacer filled channels by computational fluid dynamics I.: Pressure drop and shear rate calculations for flat sheet geometry, J. Membr. Sci. 193 (2001) 69–84. doi:10.1016/S0376-7388(01)00494-X.
[21] G.A. Fimbres-Weihs, D.E. Wiley, Numerical study of mass transfer in three-dimensional spacer-filled narrow channels with steady flow, J. Membr. Sci. 306 (2007) 228–243. doi:10.1016/j.memsci.2007.08.043.
[22] C.P. Koutsou, S.G. Yiantsios, A.J. Karabelas, Direct numerical simulation of flow in spacer-filled channels: Effect of spacer geometrical characteristics, J. Membr. Sci. 291 (2007) 53–69. doi:10.1016/j.memsci.2006.12.032.
[23] G. Srivathsan, E.M. Sparrow, J.M. Gorman, Reverse osmosis issues relating to pressure drop, mass transfer, turbulence, and unsteadiness, Desalination. 341 (2014) 83–86. doi:10.1016/j.desal.2014.02.021.
[24] G. Srivathsan, Modeling of fluid flow in spiral wound reverse osmosis membranes, (2013).
[25] A. Saeed, R. Vuthaluru, H.B. Vuthaluru, Investigations into the effects of mass transport and flow dynamics of spacer filled membrane modules using CFD, Chem. Eng. Res. Des. 93 (2015) 79–99.
[26] J. Chakraborty, N. Verma, R.P. Chhabra, Wall effects in flow past a circular cylinder in a plane channel: a numerical study, Chem. Eng. Process. Process Intensif. 43 (2004) 1529–1537. doi:10.1016/j.cep.2004.02.004.
[27] N. Kanaris, D. Grigoriadis, S. Kassinos, Three dimensional flow around a circular cylinder confined in a plane channel, Phys. Fluids. 23 (2011) 064106. doi:10.1063/1.3599703.
[28] F. Rehimi, F. Aloui, S.B. Nasrallah, L. Doubliez, J. Legrand, Experimental investigation of a confined flow downstream of a circular cylinder centred between

two parallel walls, J. Fluids Struct. 24 (2008) 855–882. doi:10.1016/j.jfluidstructs.2007.12.011.
[29] M.D. Griffith, J. Leontini, M.C. Thompson, K. Hourigan, Vortex shedding and three-dimensional behaviour of flow past a cylinder confined in a channel, J. Fluids Struct. 27 (2011) 855–860. doi:10.1016/j.jfluidstructs.2011.02.007.
[30] W. Changcharoen, S. Eiamsa-ard, Numerical investigation of turbulent heat transfer in channels with detached rib-arrays, Heat Transf.-Asian Res. 40 (2011) 431–447. doi:10.1002/htj.20357.
[31] A. Chaube, P.K. Sahoo, S.C. Solanki, Analysis of heat transfer augmentation and flow characteristics due to rib roughness over absorber plate of a solar air heater, Renew. Energy. 31 (2006) 317–331. doi:10.1016/j.renene.2005.01.012.
[32] N. Alkhamis, D.E. Oztekin, A.E. Anqi, A. Alsaiari, A. Oztekin, Numerical study of gas separation using a membrane, Int. J. Heat Mass Transf. 80 (2015) 835–843.
[33] N. Alkhamis, A.E. Anqi, A. Oztekin, Computational study of gas separation using a hollow fiber membrane, Int. J. Heat Mass Transf. 89 (2015) 749–759. doi:10.1016/j.ijheatmasstransfer.2015.05.090.
[34] T. Ishigami, H. Matsuyama, Numerical Modeling of Concentration Polarization in Spacer-filled Channel with Permeation across Reverse Osmosis Membrane, Ind. Eng. Chem. Res. 54 (2015) 1665–1674. doi:10.1021/ie5039665.
[35] C.P. Koutsou, A.J. Karabelas, A novel retentate spacer geometry for improved spiral wound membrane (SWM) module performance, J. Membr. Sci. 488 (2015) 129–142. doi:10.1016/j.memsci.2015.03.064.
[36] S. Ma, L. Song, Numerical study on permeate flux enhancement by spacers in a crossflow reverse osmosis channel, J. Membr. Sci. 284 (2006) 102–109. doi:10.1016/j.memsci.2006.07.022.
[37] F.R. Menter, Two-equation eddy-viscosity turbulence models for engineering applications, AIAA J. 32 (1994) 1598–1605.
[38] O. Zikanov, Essential computational fluid dynamics, Wiley, Hoboken, N.J, 2010.
[39] J. Tu, G.H. Yeoh, C. Liu, Computational fluid dynamics: a practical approach, 1st ed, Butterworth-Heinemann, Amsterdam ; Boston, 2008.
[40] H.K. Versteeg, W. Malalasekera, An introduction to computational fluid dynamics: the finite volume method, 2nd ed, Pearson Education Ltd, Harlow, England ; New York, 2007.
[41] J. Wijmans, R. Baker, The solution-diffusion model: a review, J. Membr. Sci. 107 (1995) 1–21.
[42] S. Rosenbaum, O. Cotton, Steady-state distribution of water in cellulose acetate membrane, J. Polym. Sci. [A1]. 7 (1969) 101–109.
[43] D.R. Paul, O.M. Ebra-Lima, Pressure-induced diffusion of organic liquids through highly swollen polymer membranes, J. Appl. Polym. Sci. 14 (1970) 2201–2224.
[44] D.R. Paul, J.D. Paciotti, Driving force for hydraulic and pervaporative transport in homogeneous membranes, J. Polym. Sci. Polym. Phys. Ed. 13 (1975) 1201–1214. doi:10.1002/pol.1975.180130612.
[45] A.E. Anqi, N. Alkhamis, A. Oztekin, Numerical simulation of brackish water desalination by a reverse osmosis membrane, Desalination. 369 (2015) 156–164. doi:10.1016/j.desal.2015.05.007.

[46] S. Singha, K.P. Sinhamahapatra, Flow past a circular cylinder between parallel walls at low Reynolds numbers, Ocean Eng. 37 (2010) 757–769. doi:10.1016/j.oceaneng.2010.02.012.
[47] M. Sahin, R.G. Owens, A numerical investigation of wall effects up to high blockage ratios on two-dimensional flow past a confined circular cylinder, Phys. Fluids. 16 (2004) 1305. doi:10.1063/1.1668285.
[48] S. Mettu, N. Verma, R.P. Chhabra, Momentum and heat transfer from an asymmetrically confined circular cylinder in a plane channel, Heat Mass Transf. 42 (2006) 1037–1048. doi:10.1007/s00231-005-0074-6.
[49] A.E. Anqi, N. Alkhamis, M.F. Alrehili, A. Oztekin, Numerical study of brackish water desalination using reverse osmosis, in: Proc. IDA World Congr. Desalination Water Reuse, San Diego, 2015.
[50] M. Asai, Y. Konishi, Y. Oizumi, M. Nishioka, Growth and breakdown of low-speed streaks leading to wall turbulence, J. Fluid Mech. 586 (2007) 371. doi:10.1017/S002211200700688X.
[51] C.R. Smith, S.P. Metzler, The characteristics of low-speed streaks in the near-wall region of a turbulent boundary layer, J. Fluid Mech. 129 (1983) 27. doi:10.1017/S0022112083000634.
[52] S.I. Chernyshenko, M.F. Baig, The mechanism of streak formation in near-wall turbulence, J. Fluid Mech. 544 (2005) 99. doi:10.1017/S0022112005006506.
[53] C.P. Koutsou, S.G. Yiantsios, A.J. Karabelas, A.J. Karabelas, Membrane module performance optimization using CFD simulation of flow through narrow channels with spacers, in: Proc. IDA World Congr. Desalination Water Reuse, 2007: pp. 21–26.
[54] A.E. Anqi, A. Oztekin, N. Alkhamis, Steady three dimensional flow and mass transfer analyses for brackish water desalination by reverse osmosis membranes, Int. J. Heat Mass Transf. (2015).
[55] A.I. Radu, M.S.H. van Steen, J.S. Vrouwenvelder, M.C.M. van Loosdrecht, C. Picioreanu, Spacer geometry and particle deposition in spiral wound membrane feed channels, Water Res. 64 (2014) 160–176. doi:10.1016/j.watres.2014.06.040.
[56] H.-G. Park, S.-G. Cho, K.-J. Kim, Y.-N. Kwon, Effect of feed spacer thickness on the fouling behavior in reverse osmosis process — A pilot scale study, Desalination. 379 (2016) 155–163. doi:10.1016/j.desal.2015.11.011.

VITA

Ali Anqi was born on June 16, 1984 in Jazan-Saudi Arabia. Ali received his Bachelor of Science degree in mechanical engineering from King Khalid University-Saudi Arabia in 2007 and joined King Khalid University in 2007. He got his Master of Science in mechanical engineering from the University of New Haven in 2012. He will receive the degree of Doctor of Philosophy in mechanical engineering from Lehigh University in 2016, and will reside in Abha-Saudi Arabia. He is author and co-author of four journal articles and two journal articles under review and five conference papers.